The University of Nottingham

UNITED KINGDOM · CHINA · MALAYSIA

Hyperpolarised Xenon Production via Rb and Cs Optical Pumping Applied to Functional Lung MRI

Hayley Louise NEWTON,

MSci. (Hons) Dunelm

THESIS SUBMITTED TO THE

UNIVERSITY OF NOTTINGHAM

FOR THE DEGREE OF DOCTOR OF PHILOSOPHY

School of Physics and Astronomy

June 2014

Abstract

Hyperpolarisation encompasses a multitude of methods to increase the species'
spin polarisation for nuclear magnetic resonance (NMR) and magnetic res-
onance imaging (MRI) applications. Hyperpolarised ^{129}Xe is produced via
spin-exchange optical-pumping (SEOP). Firstly, electronic spins of alkali metal
vapour are polarised via absorption of circularly polarised light. Alkali metal
polarisation is subsequently transferred to noble gas nuclei via collisions.

Within this thesis, the SEOP process is examined by probing the kinetics
of the ^{129}Xe polarisation build up. A combination of diagnostic techniques are
used including low field NMR to measure ^{129}Xe polarisation (P_{Xe}) at different
spatial positions, near-IR optical absorption to give a global estimate of the
alkali metal polarisation, and *in situ* Raman spectroscopy to spatially moni-
tor the energy transport processes by detecting the internal gas temperatures
(T_{N_2}). T_{N_2} values were found to be dramatically elevated above oven thermo-
couple readings, with observations of up to $\sim$1000 K for an oven heated to
only $\sim$400 K. Internal gas temperatures are presented for the first time along
the length of the optical cell, showing spatial temperature and P_{Xe} variations
during steady state and rubidium runaway conditions.

Two contrasting methods of Raman spectroscopy are examined: a conventional
orthogonal arrangement of detection and excitation optics, where intrinsic spa-
tial filtering of the probe laser is utilised; and a newly designed inline module
with all components in the same optical plane. Optical filtering is used to
reduce the Rayleigh scattering and the probe laser line. This new inline device
is presented herein and has a $\sim$23 fold improvement in signal to noise enabling
increased accuracy and precision of 'real-time' temperature monitoring.

Rubidium, caesium and a rubidium/caesium hybrid are compared as the al-
kali metal of choice in the SEOP process. Caesium has a higher spin-exchange
cross-section with ^{129}Xe, thus a system is envisaged where current Rb D_1 lasers
in many polarisers can be utilised with a Rb/Cs hybrid to gain improvements
in polarisation rates or levels. Xenon polarisations are shown up to 50% for a
hybrid cell.

Finally, preparatory experiments crucial to the imminent lung imaging study
are presented, including measurements of P_{Xe} at low and high magnetic fields.
In addition, polariser technology is examined including the current Notting-
ham device and an open-source consortium polariser.

Publications

1. **Hayley Newton**, Laura L. Walkup, Nicholas Whiting, Linda West, James Carriere, Frank Havermeyer, Lawrence Ho, Peter Morris, Boyd M. Goodson, & Michael J. Barlow; *Comparative study of in situ N_2 rotational Raman spectroscopy methods for probing energy thermalisation processes during spin-exchange optical pumping*, Applied Physics B - Lasers and Optics, 2014, **115 (2)**, 167 - 172

2. Panayiotis Nikolaou, Aaron M. Coffey, Laura L. Walkup, Brogan M. Gust, Nicholas Whiting, **Hayley Newton**, Iga Muradyan, Mikayel Dabaghyan, Kaili Ranta, Gregory D. Moroz, Matthew S. Rosen, Samuel Patz, Michael J. Barlow, Eduard Y. Chekmenev & Boyd M. Goodson; *XeNA: An automated open-source ^{129}Xe hyperpolarizer for clinical use*, Magnetic Resonance Imaging, 2014, **32 (5)**, 541 - 550

3. Nicholas Whiting, **Hayley Newton**, Peter Morris, and Michael J. Barlow & Boyd M. Goodson; *Observation of energy thermalization and $\sim$1000 K gas temperatures during spin-exchange optical pumping at high xenon densities*, manuscript in preparation, 2014

4. *'Spin-Exchange Optical Pumping at High Xenon Densities and Laser Fluxes: Principles and Practice'*, B.M. Goodson, N. Whiting, **H. Newton**, J.G. Skinner, K. Ranta, P. Nikolaou, M.J. Barlow, and E.Y. Chekmenev, invited chapter for *'Hyperpolarized Xenon-129 Magnetic Resonance (Concepts, Production, Techniques and Applications)'*, editors: T. Meersmann and E. Brunner, Royal Society of Chemistry, UK, submitted, 2014

5. Panayiotis Nikolaou, Aaron Coffey, Laura L. Walkup, Brogan Gust, Nicholas Whiting, **Hayley Newton**, Scott Barcus, Iga Muradyan, Mikayel Dabaghyan, Gregory D Moroz, Matthew S Rosen, Sam Patz, Michael J. Barlow, Eduard Chekmenev & Boyd M. Goodson; *Near-unity nuclear polarization with an 'open-source' ^{129}Xe hyperpolarizer for NMR and MRI*, Proceedings of National Academy of Sciences, 2013, **110 (35)**, 14150 - 14155

Acknowledgements

There have been many people who have helped me over the course of my PhD and I would like to take the opportunity to thank some of them here. I would like to start by thanking my supervisors, Peter Morris, Mike Barlow, and Ian Hall, for allowing me to work in such a broad spectrum of research from fundamental physics to translational medicine. Notably, I would like to thank Mike for allowing me to follow this career path by getting me excited with a summer undergraduate project in hyperpolarised ^{129}Xe MRI at Earth's field.

I have met many enthusiastic international scientists (across the big pond) who have offered much support and guidance including Nick Whiting and Boyd Goodson, thank you both for all your help. Despite all Nick's best attempts, as a graduate student I did not feel the need to start drinking coffee or take up smoking! In addition, thank you Laura Walkup for taking me under your wing when I visited your lab and for many fun adventures in the UK and the USA. Thank you Ed Chekmenev, Peter Nikolaou, Aaron Coffey, and Kaili Ranta for many polariser discussions and allowing us to visit your laboratories.

Back in Nottingham, I would like to thank the teams I have worked with, including students and staff at the MR centre. Thank you Jason Skinner for many a scientific debate, for being a great friend and introducing me to some fantastic music. Further, I would like to acknowledge Jason for jointly carrying out a great deal of the work set out in this thesis. Thank you Jonathan Birchall for loving SEOP so much that after an eventful Masters project, he decided to return to carry out his PhD work with us! Thank you Maria Liljeroth for sharing her knowledge of MRI and many an eventful night in the HILF unit, trying to keep awake in the early hours of the morning (maybe the coffee might have helped here!). I would also like to thank the other members of the hyperpolarised ^{129}Xe group at Nottingham: Robert Walker for polarising many bags of ^{129}Xe, Brett Haywood for aiding my training on becoming a competent person for MRI scanning of healthy volunteers and John Owers-Bradley for many helpful discussions. I acknowledge EPSRC for PhD funding.

Finally, I would like to thank my family, in particular my parents (Linda and Chris Newton), for all their love and support, and for encouraging me to spend many hours exploring the countryside on our horses. In addition, thank you to my loving fiancé, Phil Chung, who has been encouraging and supporting me along the way even though there was a $\sim$6000 mile distance between us!

Contents

List of Figures

List of Tables

List of Abbreviations

Abbreviation	Meaning
AM	Alkali Metal
CCD	Charge Coupled Device
COPD	Chronic Obstructive Pulmonary Disease
Cs	Caesium
CT	Computerised Tomography
DNP	Dynamic Nuclear Polarisation
FFE	Fast Field Echo
FID	Free Induction Decay
FiDCSI	Free induction Decay Chemical Shift Imaging
FIESTA	Fast Imaging Employing Steady State Acquisition
FISP	Fast Imaging with Steady state Precession
FWHM	Full Width Half Maximum
FOV	Field of View
GE	General Electric
GRE	Gradient Echo
He	Helium
HP	Hyperpolarised
HRCT	High Resolution Computerised Tomography
ID	Inner Diameter
K	Potassium
LDA	Laser Diode Array
MRI	Magnetic Resonance Imaging
N_2	Nitrogen
NG	Noble Gas
NMR	Nuclear Magnetic Resonance
OD	Outer Diameter
OP	Optical Pumping
ppm	parts per million

Abbreviation	Meaning
ppb	parts per billion
p_{Xe}	xenon partial pressure
P_{Xe}	129-Xenon polarisation
Rb	Rubidium
rf	radio frequency
SE	Spin Exchange
SEOP	Spin Exchange Optical Pumping
SNR	Signal to Noise Ratio
T_1	Longitudinal relaxation time
T_2	Transverse relaxation time
TE	Echo time
TR	Repetition time
T_{N_2}	Nitrogen rotational temperature
T_{LDA}	Laser Diode Array temperature
T_{cell}	Cell thermocouple temperature
Xe	Xenon
XeNA	Xenon polarizatioN Automated

Chapter 1

Introduction

1.1 Overview

The motivation for investigating hyperpolarised ^{129}Xe is to improve the current methods available to diagnose and monitor lung diseases. Chronic obstructive pulmonary disease (COPD) is a non-reversible air flow condition with direct annual healthcare costs to the NHS of greater than £800 million in 2011 [1]. Lung cancer is the second most prevalent cancer with a median survival time after diagnosis of only 203 days in England, [2]. Idiopathic pulmonary fibrosis is one of several interstitial lung diseases with about 4200 new cases every year in the UK [3]. With earlier and more accurate diagnosis of these types of respiratory disease, there can hopefully be improved disease management and quality of life for these patients.

A disadvantage of the most commonly used current method, high resolution computed tomography (HRCT), for investigating ventilation and perfusion in the lungs is the need for a dose of ionising radiation. Although HRCT scans provide good anatomical images, most clinical measurements of lung function (such as spirometry) assess the entire lung as a global entity. However, it is well known that both health and disease function are not homogeneous and

may vary over the lung space. The reader is referred to a review article comparing the techniques of HRCT and magnetic resonance imaging (MRI) for functional lung imaging [4]. The key advantages of MRI over HRCT is that it has the ability to probe various nuclei (e.g. ^{1}H, ^{3}He, ^{13}C and ^{129}Xe) and it is a fast technique without ionising radiation. It also provides a method by which longitudinal studies can be completed to study effects of drugs for treatments or to follow disease progression, this is more accessible with hyperpolarised gas MRI as the radiation doses experienced from HRCT scans limit repeat visits in a study.

The technique of spin exchange optical pumping (SEOP) produces a high noble gas polarisation through the transfer of angular momentum from photons in a circularly polarised laser beam to alkali metal electronic spins and this is spin-exchanged onto ^{129}Xe nuclei via collisions [5, 6]. ^{129}Xe polarisations which are many orders of magnitude greater than thermal xenon polarisations have given rise to many applications of hyperpolarised gases including lung imaging. The first hyperpolarised ^{129}Xe lung image was reported in 1994 by Albert *et al.* [7] and shows the complementary use of conventional MRI and hyperpolarised gas MRI in an excised mouse lung.

This thesis aims to investigate hyperpolarised xenon (^{129}Xe) production via rubidium (Rb) and caesium (Cs) optical pumping with an application towards functional lung MRI. The first stage in this study was to characterise the optical pumping process by looking at the individual aspects using different experimental techniques. This was carried out using various techniques including examining energy transport with Raman spectroscopy, low-field NMR spectroscopy and optical absorption. Within this work, the polarisation of ^{129}Xe was probed under different experimental conditions such as a choice of alkali metal, laser power, and laser centroid wavelength. Translating this

fundamental knowledge involved working closely with a collaboration of many research groups in the USA which came together to create an open-source clinical polariser with near unity polarisation [8, 9]. Leading towards future clinical ^{129}Xe work at Nottingham, calibrations and optimisations have been carried out on the current continuous flow polariser, with various experimental parameters being investigated including gas flow rate, volume, and accumulation time.

1.2 Thesis Outline

Chapter 2 leads the reader through the principles of hyperpolarisation and the different techniques used to polarise a sample. The author describes techniques including the brute force method, dynamic nuclear polarisation, parahydrogen, metastability exchange optical pumping, and spin exchange optical pumping. As this thesis focuses on spin exchange optical pumping this is explained in more depth than the other techniques. A comparison is drawn on the two main types of ^{129}Xe polarisers: batch mode and continuous flow. An open-source batch mode clinical polariser designed as a part of an international consortium is discussed, [8, 9]. The latter part of this chapter introduces applications of hyperpolarised samples and covers *in vivo* lung imaging and *in vitro* cryptophanes which promise to have a clinical application in the future.

Chapter 3 sets the framework for the experimental methods used in the majority of the work in this thesis. The techniques include low field ^{129}Xe NMR spectroscopy to measure the ^{129}Xe polarisation, *in situ* Raman spectroscopy to probe internal gas temperatures and energy transport within the spin exchange optical pumping arrangement, and optical absorption to look at the pump laser light absorbed in the sample by the rubidium electrons to gain an approximation of the alkali metal polarisation. The theory behind these approaches is given and the procedures for calibration and data analysis are

outlined.

Chapter 4 applies the basic principles of Raman spectroscopy laid out in Chapter 3, focusing on the geometry of the excitation and detection optics in the Raman set-up. This chapter has led to two publications: one by Whiting *et al.* [10] which gives the details of the orthogonal method and the second by Newton *et al.* [11] that describes a new in-line module with all the Raman spectroscopy optics in a single plane (180° method). An approximately 23 fold improvement in signal to noise is observed with the self-aligning inline module allowing 'real-time' monitoring of internal gas temperatures. This latter method was the subject of a talk by Newton [12] at the 4th International Conference on Xenon NMR in Materials (XeMAT 2012), Dublin, Ireland.

Chapter 5 examines current procedures for thermal management within a spin exchange optical pumping system, including overall temperature reduction, localised temperature variations and global temperature ramping. A comparison of xenon polarisations and internal gas temperatures is made when steady state conditions occur and rubidium runaway takes place. The temperature variation in the oven and internal gases during the spin exchange optical pumping experiment is spatially monitored and the impacts on the ^{129}Xe polarisation and pump laser light absorption are discussed.

Chapter 6 firstly looks at the effect of spin exchange optical pumping with different alkali metals namely rubidium and caesium and then studies the response of mixing the two metals to form a Rb-Cs hybrid. Rb and Cs are compared under spin exchange optical pumping on their respective D_1 transitions, using frequency-narrowed laser diode arrays. The proposed Rb-Cs-^{129}Xe hybrid system is expected to follow the pathway of optically pumping the Rb vapour then spin exchange with the Cs and subsequently onto the ^{129}Xe. The

xenon polarisation build up rates and maximum values obtained from the different alkali metals is examined. The first section of this chapter was presented by Whiting *et al.* [13] at the 52nd Experimental Nuclear Magnetic Resonance Conference 2011. The latter part of this work culminated in the award of the ENC Ritchey Prize 2014 and an opportunity to present our work at the 55th Experimental Nuclear Magnetic Resonance Conference 2014 by Newton *et al.* [14].

Chapter 7 translates the fundamental physics laid out in the previous chapters towards a clinical application. Measurements of thermal and hyperpolarised ^{129}Xe, enable ^{129}Xe polarisations to be measured at 2 mT and 1.5 T. Polarisations are examined at various flow rates, accumulation times and volumes of xenon gas on a continuous flow polariser to find optimal conditions with a balance between gas residence time within the cell to enable spin exchange optical pumping and accumulation time of frozen xenon. Proton lung MRI is developed with a comparison of sequences to obtain good co-registration images for future ^{129}Xe imaging of the human lung.

Chapter 2

Principles and techniques of hyperpolarisation

2.1 Strategies for improving nuclear spin polarisation

The sensitivity is limited in conventional nuclear magnetic resonance resonance (NMR) due to the small population differences in the nuclear Zeeman energy levels even at high magnetic fields, Figure 2.1(a). For example, the proton polarisation at room temperature and 9.4 T is only $P_{thermal} \approx 3\text{x}10^{-5}$. This arises from the equilibrium Boltzmann equation in the high temperature approximation:

$$P_{thermal} = \frac{\gamma \hbar B_0}{2 k_B T} \tag{2.1}$$

where γ is the gyromagnetic ratio of the sample, $\hbar$ is the reduced Planck's constant, B_0 is the magnetic field, k_B is Boltzmann's constant, and T is the sample temperature.
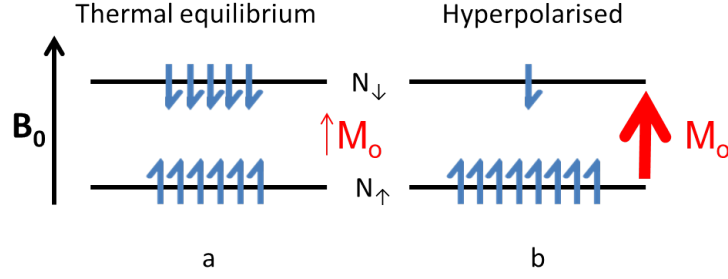
Figure 2.1: Thermal equilibrium state (a) has small population difference with a small magnetisation vector, M_0, whereas (b) hyperpolarised state has a much larger magnetisation vector resulting from a large spin polarisation. $N_\uparrow$ and $N_\downarrow$ denote the two states.

Considering a spin-1/2 system, the polarisation can be described as

$$P = \frac{N_\uparrow - N_\downarrow}{N_\uparrow + N_\downarrow} \tag{2.2}$$

where $N_\uparrow$ and the $N_\downarrow$ are the number of spins in the two sublevels, Figure 2.1. Polarisation is directly related to the observable magnetisation, M_0 by considering the total number of nuclear spins, N_s and the gyromagnetic ratio, [15]

$$M_0 = \frac{1}{2} N_s \gamma \hbar P \tag{2.3}$$

To improve this inherent limitation in NMR sensitivity, it can be seen that there are two potential ways of increasing the thermal polarisation. The first is to increase the magnetic field, B_0, and the second would be to lower the temperature, T, of the sample to around a few Kelvin. This is a disadvantage for biological substances which can not be cooled to low temperatures without altering or destroying the sample. In addition, high magnetic field strengths are very expensive. Hyperpolarisation techniques can be used to increase the polarisation of a sample, by various methods as discussed below. Hyperpolarisation is a non-equilibrium technique resulting in non-renewable polarisation; this means that once the sample has been saturated (either a single 90° pulse or multiple low flip angles) it has been 'used' and returns to its thermal equilibrium state, it then needs to be re-polarised before it can

be 'used' again. In this non-Boltzmann distribution of nuclear spins where there are more nuclear spins in the lower state than the upper state, Figure 2.1(b), NMR enhancements of 3-5 orders of magnitude are achieved. A brief overview of various techniques to obtain hyperpolarised states are described in the following sections.

2.1.1 Brute force polarisation

The brute force method of polarisation (or cryogenic method) relies on cooling the sample to very low temperatures in a high B_0 field, to obtain high equilibrium xenon polarisations. For example, the theoretical thermal polarisation is $\approx 99.96\%$ for ^{129}Xe at 1 mK and 15 T [16]. The main obstacle to overcome is the time it takes to polarise a sample. At 4.2 K the T_1 is greater than 60 hours for natural abundance xenon (^{129}Xe and ^{131}Xe), rising to $\sim$180 hours with isotopically enriched ^{129}Xe. This polarisation time constant is reduced with the addition of a relaxant, such as O_2 or ^{3}He [17, 18], this lessens the time it takes to produce a hyperpolarised sample. The advantage of this method is that it can be applied to various nuclei as the system is not restricted to polarising xenon.

2.1.2 Dynamic nuclear polarisation (DNP)

Dynamic nuclear polarisation (DNP) can be used to hyperpolarise solid and liquid samples. DNP utilises low temperatures to cool a sample, containing, for example ^{13}C, which has been doped with molecules having unpaired electron spins (free radicals). Microwave radiation is applied to induce electron-nuclear spin transitions. This technique utilises the high gyromagnetic ratio of the electron to obtain high electron polarisations at low temperatures which can then be transferred to the nuclei of interest ($\gamma_e = 1.76$ x 10^5 MHzT^{-1}, $\gamma_{^{13}C} = 10.7054$ MHzT^{-1} from ref [19] and [20]). The reader is referred to a review by

9

Hurd *et al.* [21] for more information on this technique.

2.1.3 Para-hydrogen

The para-hydrogen technique involves a rapid conversion of ortho-hydrogen
($\uparrow\uparrow$) to para-hydrogen ($\uparrow\downarrow$) by use of a metal catalyst and low temperatures
[22, 23]. This utilises the knowledge that ortho-hydrogen is dominant at room
temperature but para-hydrogen becomes energetically favourable at decreased
temperatures. This para-hydrogen polarisation can then be transferred to
other species in order to follow chemical and biological processes. Further
information is in a review article by Duckett *et al.* [22].

2.1.4 Metastability exchange optical pumping

Metastability exchange optical pumping is only used to hyperpolarise ^{3}He,
which, as will be discussed in section 2.1.5.2, is experiencing a world-wide
shortage. This technique uses two excited states of the same species such
that a weak radio frequency (rf) discharge causes a transition to an excited
metastable state and then irradiation with 1083 nm circularly polarised light
is the optical pumping transition. More information can be found in a paper
on the fundamental aspects of this technique by Batz *et al.* [24].

2.1.5 Spin exchange optical pumping

The work described in this thesis uses spin exchange optical pumping (SEOP)
which is now described in detail. SEOP utilises a transfer of momentum be-
tween the electronic spins in alkali metal vapour and noble gas nuclei to pro-
duce hyperpolarised noble gases, the choice of which will be discussed below.

Optical pumping originated in the 1950s from experiments by Kastler [25]
who demonstrated that light can be used to remove electron spin populations
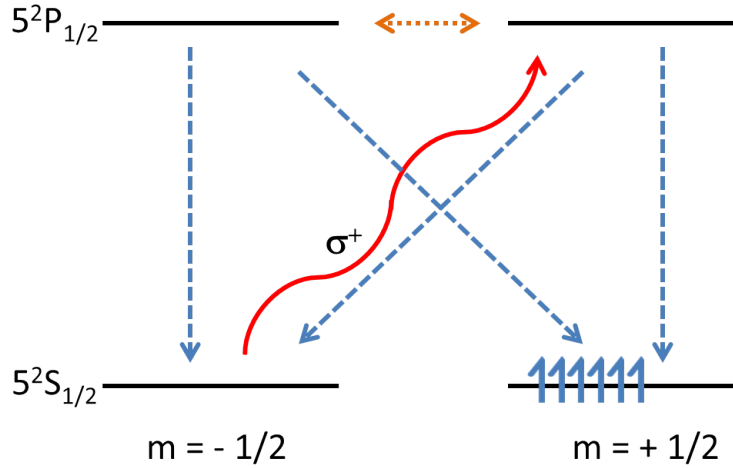
Figure 2.2: Schematic of optical pumping of Rb electron spins. Transition due to circularly polarised light is denoted by the red line, blue lines signify relaxation, orange is collisional mixing.

from their state of thermal equilibrium. He also envisaged experiments where it was possible to transfer the non-equilibrium spin polarisation from electrons to nuclei.

The SEOP process involves an alkali metal (e.g. K, Rb or Cs) and a noble gas (e.g. ^{3}He, ^{21}Ne, ^{83}Kr, ^{129}Xe or ^{131}Xe) [26–29]. Circularly polarised resonant laser light drives a transition to polarise the alkali metal (AM) electron's spins, Figure 2.2. This spin is then transferred as angular momentum to the nuclei of the noble gas (NG) to give a non-thermal distribution of nuclear spins, known as hyperpolarisation.

Alkali metals are used in this process as they possess a single unpaired electron in their valence shell, which has the spin state of 1/2. Also, it is highly convenient that they have strong absorption lines where lasers are commercially available. For example, the Rb D$_1$ ($5^2S_{1/2} \rightarrow 5^2P_{1/2}$) line is at 794.77 nm and the Cs D$_1$ line is at 894.36 nm ($6^2S_{1/2} \rightarrow 6^2P_{1/2}$), air reference, [30, 31]. These transitions, Figures 2.3 and 2.4, are described by term symbols which
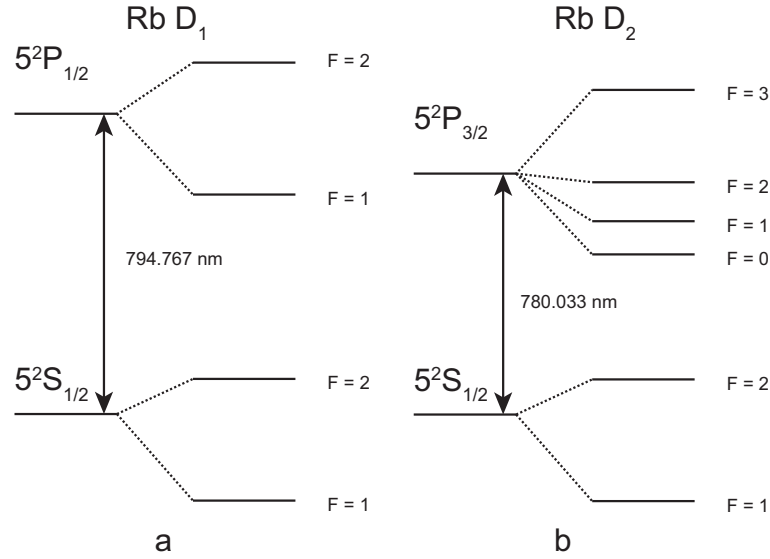
Figure 2.3: ^{87}Rb D_1 and D_2 transitions showing hyperfine structure, [30]. Both transitions originate from the same ground state with the D_2 absorption (b) resulting in a lower excited state than the D_1 transition (a). **F** denotes the total atomic angular momentum which gives rise to the hyperfine splitting. $\mathbf{F} = \mathbf{J} + \mathbf{I}$ where **J** is the total electron angular momentum and **I** is the total nuclear angular momentum, with the magnitude of F being $|J - I| \leqslant F \leqslant J + I$. For example for the ground state $5^2S_{1/2}$ of ^{87}Rb, $J = 1/2$ and $I = 3/2$, therefore $F = 1$ or 2. For ^{85}Rb (not shown), $I = 5/2$, so ground state splitting is $F = 2$ or 3. Spacing between the S and P sublevels are not to scale, wavelengths are shown with air reference.
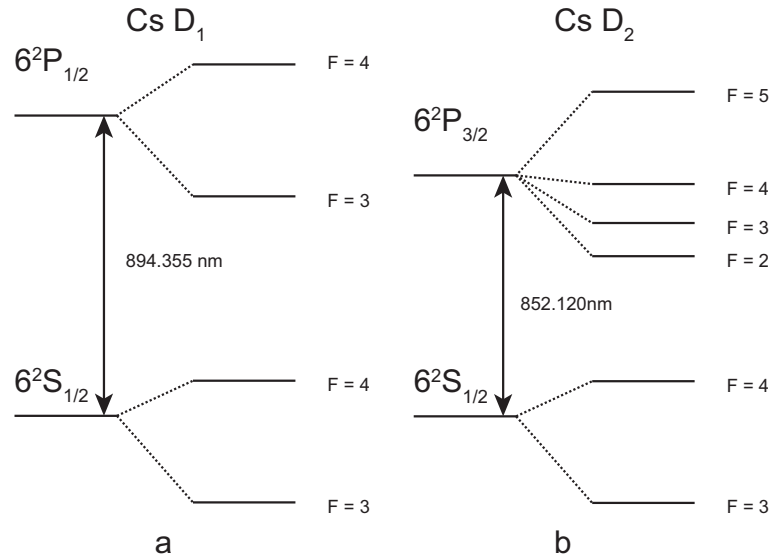
Figure 2.4: Absorption lines for Cs (a) D_1 and (b) D_2 from 894.593 nm and 852.347 nm respectively, [31]. The nuclear spin of ^{133}Cs is $I = 7/2$, consequently, for the D_1 ground state $(6^2S_{1/2})$ $F = 3$ or 4, and for the D_2 excited state $(6^2S_{3/2})$ $F = 2$, 3, 4 or 5. Spacing between the S and P sublevels are not to scale, wavelengths are shown with air reference.

are used to denote a particular electronic state within an atom, noting the angular momentum and the atomic orbital location, known as the principle quantum number, n:

$$n^{2S+1}L_J \tag{2.4}$$

where L is the electron orbital angular momentum (e.g. L $= 0$ denotes the S level and L $= 1$ denotes the P level), J is the total angular momentum and S is the total spin electronic angular momentum, with $2S + 1$ being the spin multiplicity term.

In further detail, the hyperpolarisation process begins with circularly polarised resonant photons (normally D_1 transition) whose angular momentum is transferred to the electron spin of the alkali metal in the presence of a weak magnetic field (e.g. 30 G). This excites the Rb electron spins from the $5^2S_{1/2}$, $m = -1/2$ to the $5^2P_{1/2}$, $m = +1/2$ state as the angular momentum has to be changed by $\Delta m = +1$ due to selection rules (Figure 2.2). Collisions will occur which lead to depletion of the population. Repopulation of the required $5^2S_{1/2}$, $m = +1/2$ state will cycle until a steady state is formed, thus giving rise to electron polarised alkali metal vapour, which results in the alkali metal polarisation, P_{AM}. This is a balance between the rate of optical pumping, $\gamma_{OP(z,r)}$, as a position of z the depth into the optical pumping (OP) vessel (known as a cell) and r the radial distance from the centre, and the rate of alkali metal spin destruction, Γ_{SD} [32].

$$P_{AM} = \frac{\gamma_{OP(z,r)}}{\gamma_{OP(z,r)} + \Gamma_{SD}} \tag{2.5}$$

For optical pumping to create a high P_{AM} we need $\gamma_{OP(z,r)} \gg \Gamma_{SD}$. The rate of optical pumping is defined as [33]

$$\gamma_{OP(z,r)} = \int \Phi(z,r,v).\sigma_0(v)dv \tag{2.6}$$

where $\Phi(z, r, v)$ is the amount of light flux at position (z, r) per unit of frequency, (hence the need for high powered resonant lasers) and $\sigma_0(v)$ is the frequency-dependent absorption cross-section of the alkali metal. Counteracting this, the rate of spin destruction of the alkali vapour is [33],

$$\Gamma_{SD} = \sum_i k_{SD}^i.[M_i] \tag{2.7}$$

which is the sum over all the collisions, k_{SD}^i which occur between the alkali metal and a gas, i, combined with the number density, $[M_i]$, of the particular gas. Although some collisions are undesirable due to spin destruction, others will transfer the polarisation from the polarised alkali metal electron to the unpolarised noble gas nucleus. This occurs via Fermi contact hyperfine interactions [34],

$$\alpha \vec{S}.\vec{I} = \frac{\alpha}{2}[S^+I^- + S^-I^+] + \alpha S_Z I_Z \tag{2.8}$$

where α is the coupling constant between the nuclear spin and the electron spin and is proportional to the probability of the two species being in the same place. The element $S^+I^- + S^-I^+$ is known as the flip-flop term and governs the process of polarisation transfer, which leads to a build up of a polarised noble gas P_{NG} given by [32]

$$P_{NG} = P_{AM(z,r)} \left(\frac{\gamma_{SE}}{\gamma_{SE} + \Gamma_{NG}} \right) (1 - \exp[-(\gamma_{OP(z,r)} + \Gamma_{NG})t] \tag{2.9}$$

where Γ_{NG} is the spin destruction rate of the noble gas nuclei and is equivalent to $1/T_1^{NG}$. The process of relaxation is mostly dependent on collisions with the wall of the vessel. γ_{SE} is the spin exchange rate between the alkali metal and the noble gas [33],

$$\gamma_{SE} = [AM]_{cell} \left[\frac{\gamma_{AMNG}}{[NG]_{cell}} \left(\frac{1}{1 + br} \right) + <\sigma v> \right] \tag{2.10}$$

where $[AM]_{cell}$ is the number density of the alkali metal vapour, γ_{AMNG} is
the spin exchange rate due to $3-$body Van der Waals type interactions and
$< \sigma v >$ is the velocity averaged cross-section occuring in $2-$body binary type
interactions. A discussion on Rb/^{129}Xe spin exchange rates due to these two
different types of interactions is presented in a paper by Cates *et al.* [35]. The
value [33] br is governed by the pressure of both the buffer gas, p_{N_2} and the
noble gas, p_{NG},

$$br = 0.275 \left(\frac{p_{N_2}}{p_{NG}} \right) \tag{2.11}$$

In ideal conditions, with perfect polarisation transfer, the noble gas polarisa-
tion tends towards the polarisation of the alkali metal.

$$\lim_{t\to\infty;\gamma_{SE}\gg\Gamma_{NG}} P_{NG} \to P_{AM} \tag{2.12}$$

2.1.5.1   Choice of alkali metal

Rubidium has commonly been used for optical pumping with ^{129}Xe due to the
availability of lasers at the wavelength required. However, caesium is thought
to be a better prospect for spin-exchange. Due to its larger size (Cs has an
atomic radius of 235 pm and the radius of Rb is 216 pm, [38]), its electrons are
more easily spin-polarised and the process of spin-exchange to the noble gas
is more efficient. Shao *et al.* [39] measured the spin exchange rates for K, Rb
and Cs to be 0.031, 0.048 and 0.062 s^{-1} respectively under typical conditions.
Additionally, Cs has a much lower melting point [40], 28.4 °C, compared to
Rb at 39.3 °C, so lower oven temperatures can be utilised for spin exchange.
Furthermore, the vapour pressure, P_V, of Cs is much greater than Rb (and
of K). At 25°C, $P_V(\text{Rb}) = 3.92(20)\text{x}10^{-7}$ torr [30], $P_V(\text{Cs}) = 1.488(74)\text{x}10^{-6}$
torr [31], $P_V(\text{K}) = 9.75\text{x}10^{-9}$ torr [36]. Relative vapour pressure ratios for the
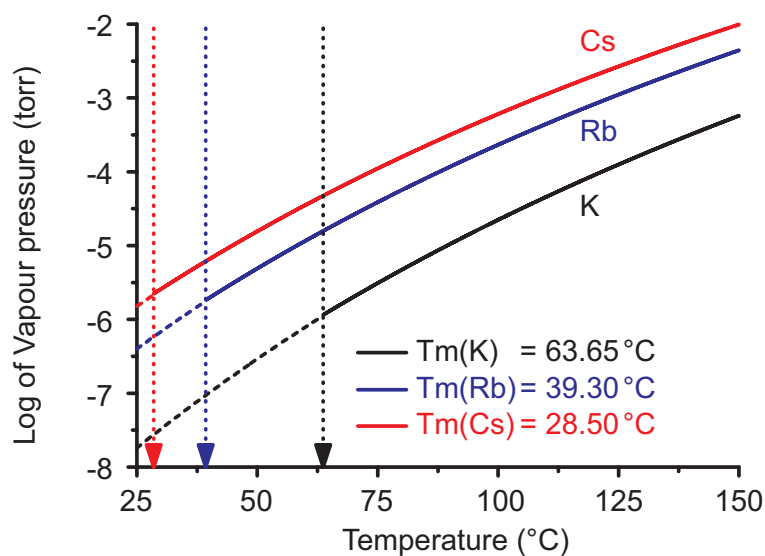
Figure 2.5: Vapour pressure curves of K, Rb and Cs. Solid lines show vapour pressure curves above melting point, dashed lines show vapour pressure curves below melting point, dotted arrow lines show melting point of respective elements. Data from refs [30, 31, 36].
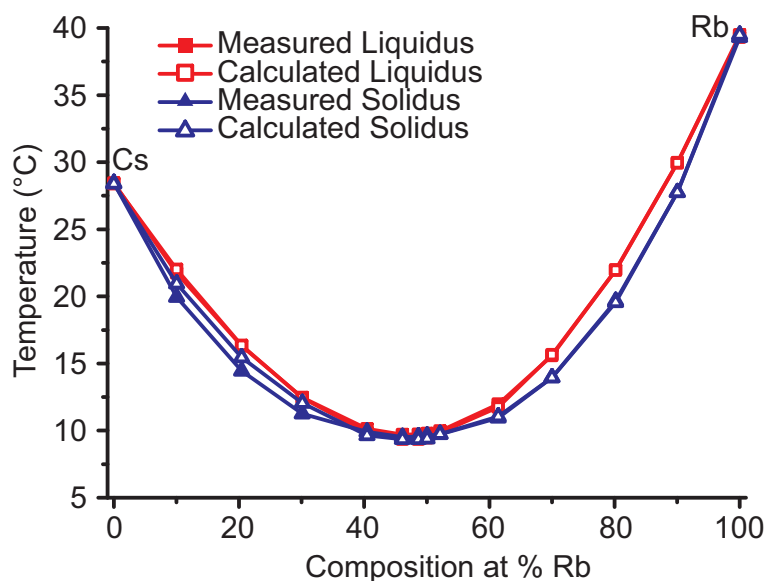
Figure 2.6: Liquidus (red) and solidus (blue) curves for hybrid Cs-Rb. Open symbols represent calculated values, closed are measured values. Liquidus and solidus are the points at which the composition is completely liquid and solid respectively, the gap between the two values are the melting interval where both states co-exist. Figure is adapted from reference [37].

alkali metals are shown in equation 2.13 and demonstrated in Figure 2.5.

$$\frac{P_V(Cs)}{P_V(Rb)} \approx 3.8 \quad \frac{P_V(Rb)}{P_V(K)} \approx 30 \quad \frac{P_V(Cs)}{P_V(K)} \approx 114 \qquad (2.13)$$

A hybrid of alkali metals in the SEOP process was first proposed by Happer *et al.* [41] in a USA patent in 2001, followed by experiments by Babcock *et al.* [42] in 2003 examining K/Rb hybrid vapour with ^{3}He. In 2007, Chen *et al.* [43] compared the previous work of Babcock *et al.* to pure K SEOP. Babcock *et al.* [42] used the knowledge that K/^{3}He collisions are more efficient at polarisation transfer than Rb/^{3}He collisions and thus a standard Rb laser was used to optically pump, with the momentum being transferred via collisions to K electrons and then onto ^{3}He. Whiting *et al.* [28] showed that with the use of frequency-narrowed high powered laser diode arrays, the spin exchange rate of Cs-^{129}Xe is 1.5 times higher that of Rb-^{129}Xe. These alkali metal hybrid principles were applied to Rb/Cs in our work, using a standard Rb laser and exploiting the fact that the binary spin-exchange rate coefficient[1], κ, for Cs-^{129}Xe is 1.6 times greater than Rb-Xe^{129}. (At 9.4 T, Jau *et al.* showed κ (Cs-^{129}Xe) = $(2.81 \pm 0.2)\,x\,10^{-16}$cm^{3}s^{-1}, [44] and κ (Rb-^{129}Xe) = $(1.75 \pm 0.12)\,x\,10^{-16}$cm^{3}s^{-1}, [45].) For a hybrid mixture of Rb and Cs, we have to consider the liquidus and solidus transition points instead of melting points. This is due to the non-pure substance in which there is a transition over which the melting occurs where both solid and liquid states are present. These transition points are shown as a function of the percentage of Rb in the alloy in Figure 2.6.

This argument is further forged by considering the spin-exchange cross sections which are 1.2 times greater for Rb-Cs than Rb-Rb [46], as shown in Table 2.1. In addition, the characteristic time for spin-exchange between non-identical

---

[1]The spin exchange rate coefficient, γ_{SE}, shown in equation 2.10 encompasses both the 2 body and 3 body interactions. The 2 body term is denoted separately by the binary spin-exchange rate coefficient, κ.

Table 2.1: Comparison of spin exchange cross section and time constants for Rb^{87}-Rb^{87} and Rb^{87}-Cs^{133}. [a] data from Gibbs and Hull [46] and [b] data from Happer [5].

Alkali Metal	Spin-exchange cross-section x 10^{-14} cm^2	spin-exchange time x 10^{-10}cm^{3}s^{-1}
Rb^{87}-Rb^{87}	1.9±0.2 [a]	7.9±0.8 [a]
Cs^{133}-Cs^{133}	2.20±0.35 [b]	
Rb^{87}-Cs^{133}	2.3±0.2 [a]	8.6±0.9 [a]

atoms (cross-exchange between Rb^{87}-Cs^{133}) is greater than the self-exchange time between Rb^{87}-Rb^{87}, Table 2.1. These arguments suggest that hybrid Rb/Cs SEOP with ^{129}Xe is worth exploring.

2.1.5.2 Choice of noble gas

^{3}He has been widely used for hyperpolarised noble gas applications due to its large gyromagnetic ratio; 32.4338 MHz/T for ^{3}He compared to 11.7769 MHz/T for ^{129}Xe, ref [20]. However, a downside of ^{3}He is the worldwide shortage of the gas which is such an issue that the US Department of Energy prepared a white paper on it in 2009 [47] and the issue was presented before congress in 2010 [48]. The only method to produce ^{3}He is via the radioactive decay of tritium (^{3}H ($t_{1/2}$=12.3 years) $\rightarrow$ ^{3}He + β), but this is in decline due to reductions in the arsenal of stored nuclear weapons. Current users of ^{3}He have two options: set up recycling procedures to reuse the ^{3}He that they have, or look for other viable options.

Naturally abundant ^{129}Xe is a good alternative to ^{3}He, as despite it's lower gyromagnetic ratio which leads to a decreased magnetisation (equation 2.3) the time required to polarise a sample is much reduced (from hours to minutes). In addition, ^{129}Xe has a very large chemical shift range which enables it to be used as an molecular probe in MRI. As a further advantage of ^{129}Xe, it is soluble in many solvents. Importantly, it dissolves in the blood stream and a dissolved phase image can be obtained as well as a gas phase image in the
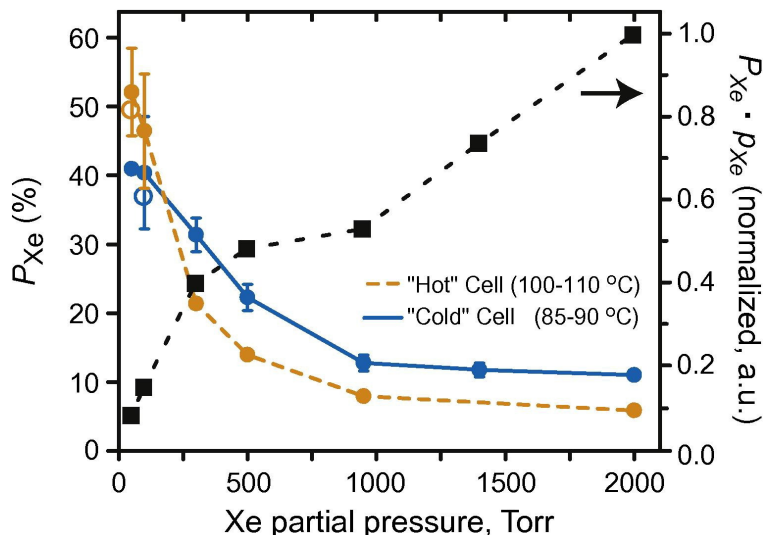
Figure 2.7: Xenon polarisation, P_{Xe}, for various Xe partial pressures, p_{Xe}, under two temperature regimes. Right axis shows $P_{Xe}.p_{Xe}$ being increased with increasing Xe partial pressure. Reprinted figure from [33] with permission from Elsevier.

lung. This allows the transfer of gas from the lungs to the blood through the alveolar walls to be monitored, giving further diagnostic information.

Traditionally within the field, most groups use a low Xe density mix, for example the commercial GE clinical polariser generally uses a 1% Xe, 10% N_2, 89% He composition, [49]. The reason for working at low Xe densities is due to the ^{129}Xe-^{129}Xe spin- destructing collisions which occur and are increasingly destructive at higher densities. However, within our research group it has been shown by Whiting *et al.* [33], Figure 2.7, that although the polarisation of ^{129}Xe, P_{Xe}, is low at high partial pressures, p_{Xe}, the product of the two components, $P_{Xe}.p_{Xe}$ which is directly related to the magnitude of ^{129}Xe NMR signal, shows a previously unexpected upward trend. This has led to our group collaborating in a consortium of researchers to build a polariser with near unity polarisation at high Xe densities, [8].

2.1.5.3   Choice of buffer gas

Nitrogen gas, and often ^{4}He, are added to the noble gas and alkali metal mixture within the OP cell as buffer gases. Both of these gases are added into the vessel to pressure broaden the alkali metal absorption line; predominantly in early work with broadband lasers high pressures of He were used for pressure broadening, [32]. Nitrogen also has a second use of quenching undesired alkali metal fluorescence. This violet emission (421 nm, 6P to 5S) was visually shown for Rb/^{129}Xe by Saha *et al.* [50]. This emission would be harmful to the overall polarisation as it is omni-directional and unpolarised. With little or no nitrogen gas, energy pooling occurs in a collision of two Rb atoms such that their energy is shared with one having a higher energy and the other returned to its ground state. 421 nm light is emitted when the highly excited Rb relaxes back to its ground state. The authors also noted other emissions at various wavelengths and degradation of the optical cell coatings, leading to a lower P_{Xe}. In the studies in this thesis, experimental work includes a variety of binary (^{129}Xe/N$_2$) mixtures, always using >500 torr N$_2$ to prevent radiative relaxation processes occuring.

Due to the ability of nitrogen gas to non-radiatively de-excite the alkali metal transitions, it can be used to examine the gas temperature within the OP cell. This has been studied by Walter *et al.* [51] who found that for an outer cell temperature of 100°C and 15 W of broadband laser light, the nitrogen ro-vibrational temperature was greatly elevated using *in-situ* Raman measurements, with ^{4}He as a buffer gas. This thesis builds on these data using high-power frequency-narrowed lasers and we will obtain temperatures without ^{4}He, i.e. only using N$_2$ and Xe.

2.2   Hyperpolariser technology for ^{129}Xe

^{129}Xe can be produced using a hyperpolariser (also known as a polariser), using two different methods. The first is a continuous flow design where a lean xenon gas mix is flowed through an optical pumping cell (with buffer gases) at a fixed flow rate. Upon exit from the polariser the polarised gas can either flow directly to an experiment or it can be frozen and accumulated for later use. The second method is known as batch mode where xenon along with the buffer gases are heated inside an oven with optical pumping by a high power laser. Upon reaching steady state polarisation, which can occur within minutes to tens of minutes, the cell is cooled and then the gas is moved out of the cell.

Along with the different gas flow mechanisms, there are two different pressure regimes resulting from two types of spin-exchange collisions. Rb-^{129}Xe collisions can occur via sudden binary collisions which are 2-body interactions, or by long-lived van der Waals molecules resulting from three-body collisions. The 2-body interactions are pressure independent and dominant at high pressures, whereas the three-body collisions are more efficient at Rb-^{129}Xe spin exchange and this dominants at low pressures.

The first continuous flow polariser was presented by Driehuys *et al.* [32] which was later used as a prototype for the company Magnetic Imaging Technologies INC (MITI) [52], which was taken over by GE Healthcare, currently the technology is available through Polarean [53]. Lean xenon mixes (e.g. 1% Xe, 10% N_2, 89% He) are used to reduce the Rb-^{129}Xe spin-destruction which is a dominant relaxation process at high pressures, [54]. However, low partial pressures of xenon necessitate compression or cryogenics to obtain high magnetisation. Xenon is generally separated from the buffer gases and accumulated as frozen xenon to be sublimated for gaseous applications. The polarisation after an

accumulation time, t_a is dependent on the original ^{129}Xe polarisation, $P_{Xe}(0)$, and the T$_1$ of the solid xenon at a particular magnetic field, [32].

$$P_{Xe}(t_a) = P_{Xe}(t_0)\frac{T_1}{t_a}(1 - e^{-t_a/T_1}) \qquad (2.14)$$

Examples of various ^{129}Xe polarisers utilising a continuous flow device have been shown by Hersman's group [55], Saam's group [56] and Wild's group [54].

Recent success in large-scale ($\sim$1 l/hr) batch mode polarisers has produced near unity polarisations at high xenon densities with an open-source design by Nikolaou *et al.* [8]. This device builds on previous work by Whiting *et al.* [33] who found surprisingly high xenon polarisations under conditions of high xenon partial pressures, as shown in Figure 2.7. A consortium of hyperpolarised xenon researchers collaborated to design and build an automated, modular instrument known as XeNA - Xenon polarizatioN Automated. High resonant photon flux of up to 200 W at the Rb D$_1$ transition with xenon rich gas mixes, produced xenon polarisations of 30-90% for 300-1600 torr xenon, with nitrogen making up the total cell pressure of 2000 torr in a 500 cc volume. One of the main advantages of batch mode collection is that it negates the need for a cryogenic collection, this lessens the design complexity and removes the losses in ^{129}Xe polarisation caused by storage as frozen xenon and phase transitions. It was shown by Kuzma *et al.* [57] that rapid sublimination is required as the T$_1$ near the Xe melting point (161.4 K) is only 6 s. However, cryocollection does aid in the removal of residual rubidium and reduces the likelihood of it entering the sample collection vessel, accordingly in the batch mode collection a Teflon filter is used in the transfer line. Full technical details of this device are available in a report by Nikolaou *et al.* [9]. A second generation ^{129}Xe polariser device built within the consortium is known as XeUS [58, 59] and includes a 3D-printed oven which increases the simplicity of the integration and alignment of various components including the *in situ* NMR using
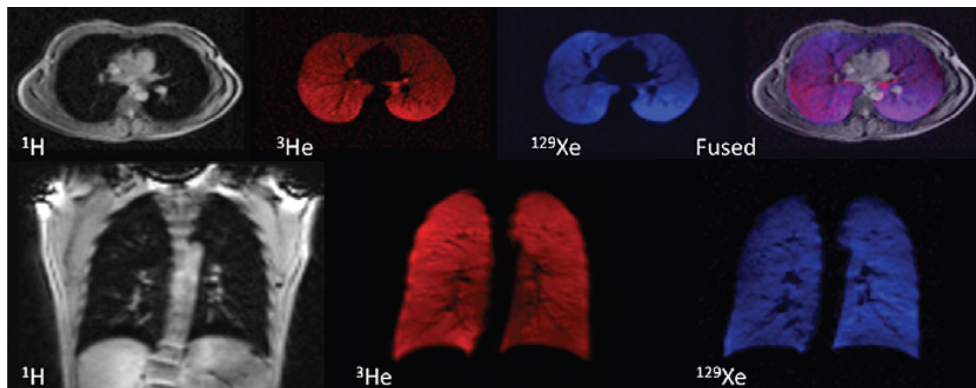
Figure 2.8: Lung images acquired from a healthy volunteer showing the complementary use of the three nuclei: ^{1}H, ^{3}He (red) and ^{129}Xe (blue). Reprinted figure from [60], with permission from RSNA.

3D-printed coil formers, laser alignment, optics holders for retro-reflection, optomechanical alignment, OP cell valve holders. In addition, the device has a thermo-electric temperature control unit, *in situ* near-IR spectroscopy and is fully automated. Incredibly high xenon polarisations of $74 \pm 7\%$ were monitored with a high xenon partial pressure of 1000 torr in a 500 cc cell. These high xenon partial pressures provide high magnetisation for a multiple of different applications across many fields incorporating preclinical, clinical, and materials magnetic resonance spectroscopy and imaging.

2.3 Applications of hyperpolarised noble gases

Hyperpolarised noble gases have been used for a variety of applications, a brief selection of which are discussed here. The most popular is *in vivo* lung imaging. As mentioned in Chapter 1, Albert *et al.* [7] presented the first reported image of ^{129}Xe in lung tissue in 1994. Since then there have been many studies of lung disease, using both ^{3}He and ^{129}Xe. In recent years, Wild *et al.* [60] has presented work enabling the acquisition of ^{1}H, ^{3}He and ^{129}Xe images simultaneously to enable co-registration from a ^{1}H image, diffusion information for the different hyperpolarised nuclei and an image of ^{129}Xe dissolved into the blood stream due to its solubility and large chemical shift range. This

provides complementary structural and functional data. Driehuys *et al.* [61] discussed the tolerability and safety of ^{129}Xe as a probe for lung diseases whilst performing MRI within a 16 second breath hold. It was found that no serious adverse events resulted and no significant changes in vital signs were observed, although the majority of subjects did experience some mild short-lived symptoms such as dizziness. Another emerging translated methodology from the chemical to medical field is the use of caged xenon, which allows the user to have a targeted biosensor due to the chemical shift of ^{129}Xe and its ability to act as a host. Work in this area has been recently reported by Klippel *et al.* [62] where the possibility for a highly sensitive tracer is discussed.

Chapter 3

Experimental methods for probing a low-field ^{129}Xe system

3.1   Introduction

This chapter describes the experimental methods used in the majority of this thesis. Details are provided here of the optical pumping cells, the alkali metal and gas filling process, and the lasers. In addition, approaches utilised for low field NMR spectroscopy, optical absorption and for measuring in cell buffer gas temperatures with Raman spectroscopy are discussed.

3.2   Optical bench setup

3.2.1   Optical pumping cells

For the majority of experiments reported here, a new design of optical pumping cell was used, Figure 3.1. It is based on a Rosen style cell [63], but with adaptations described below to allow for ease of access to the oven [10]. The inner cell used for SEOP is ∼167 mm long and ∼20 mm in diameter and is made from Pyrex glass. It is held in a Pyrex glass cylinder with Chemglass

(a)

(b)
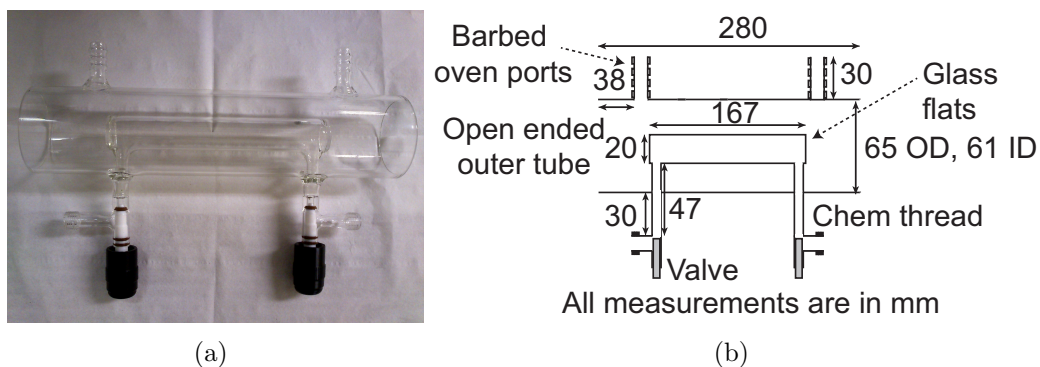
Figure 3.1: Optical pumping cell photograph (a) and schematic (b) used for the majority of experiments in this thesis. The design is a Pyrex cylinder measuring ∼167 mm long, ∼20 mm diameter with flat end windows for the pump beam to traverse through. An open-ended Pyrex outer jacket in combination with Teflon window mounts creates a hot air oven. This cell is a modification of a design by Rosen *et al.* [63].

(a)   (b)
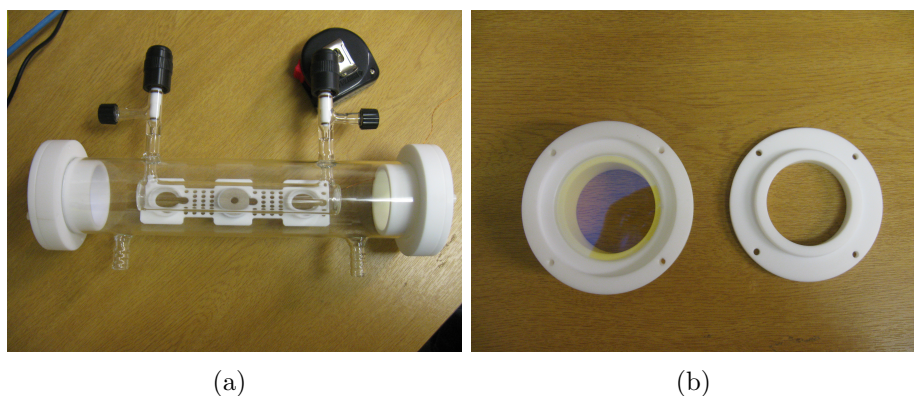
Figure 3.2: Teflon window mounts referred to in Figure 3.1 are shown here mounted onto the glass cell (a). These create an oven outside the sealed reaction vessel containing the alkali metal and noble gas. The anti-reflective coated windows are removable (b) in order to allow for ease of alkali metal distribution by a heat source.
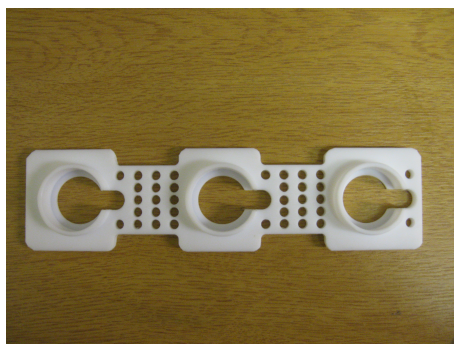
Figure 3.3: Surface coil mounts which allow measurement of ^{129}Xe polarisation at different positions, generally front, middle and back of the OP cell

Chem-thread #7 valves to allow the cell to be loaded by a pipette method. The open outer cylindrical vessel allows for the surface NMR coils to be placed immediately adjacent to the inner cell containing the SEOP components. The surface NMR coils are placed on a mount which can be slid into the oven space and has holes to allow air flow through the vessel, Figure 3.3. The oven is formed by using Teflon mounts, Figure 3.2, which can hold anti-reflection coated windows. A layer of foam is applied between the Teflon mounts and the glass to allow for thermal expansion of the two materials. The removable window mounts also enable the distribution of the alkali metal by use of a hot air blower which can heat the flat ended windows of the inner oven to prevent deposition onto the windows where the laser would penetrate.

Optical pumping cells are prepared by first placing them into a base bath solution of potassium hydroxide and methanol to clean the glassware. This process is followed by a rinse with distilled water. The cell is then placed into a solution of 1:1 distilled water and methanol in a sonic bath for one hour. Finally, the cell is rinsed with methanol to remove traces of water. Once the vessel is dry, a solution of SurfaSil is applied to the internal surface of the inner cell walls as a coating to reduce the wall relaxation in the SEOP process [64, 65]. This consists of a series of washes starting with hexane then a solution of 15% SurfaSil with hexane. This is repeated three times, finishing with a rinse of hexane and a separate methanol rinse to remove any uncoated SurfaSil. It was shown by Zeng *et al.* [64] that a silicone coated pyrex cell increases the T_1 to about 20 mins from the order of tens of seconds in a non-coated cell. The reasons for this reduction in ^{129}Xe surface relaxation were discussed by Driehuys *et al.* [65] where various mechanisms were presented including the Xe being absorbed on the coating surface with a large energy barrier that hinders its escape.

After a drying process, the cell is prepared for alkali metal filling. First the vessel is evacuated using a rotary and turbo pump to the 10^{-5} torr range and then transferred into a controlled environment cabinet with oxygen levels less than 10 parts per million (ppm) and water levels less than 2 ppm. Alkali metal is heated in its ampule or a Schlenk tube (which is used as a storage vessel from previous cell fillings) and then pipetted into the OP cell through one of the Chem-thread valves. Once the alkali metal has solidified it can be removed from the controlled environment cabinet and then the gas filling preparation can be undertaken.

Following a cell filling procedure, any materials with alkali metal on it needs to be thoroughly cleaned to prevent adverse reactions taking place. A mixture of tert-butanol with a small quantity of methanol (to keep the tert-butanol in liquid state) is used to dissolve left over alkali metal in a safe manner within a controlled environment cabinet.

3.2.2 Gas loading

In initial experiments in section 4.2 and 6.1, the cell was moved from the optical table to a separate gas loading manifold in order for gas loading to take place. However, it was noted that time-consuming laser alignment would need to take place after each gas loading on the separate rig, to aid reproducibly. It was therefore decided to implement an *in situ* gas loading which could take place on the optical table without the need for realignment of the laser, thus improving reproducibly of multiple gas mix filling. This method was used in Chapter 5 and sections 4.3 and 6.2.

The gas loading procedure, Figure 3.4, begins with evacuation of the cell to the mid 10^{-5} torr range and heating of the alkali metal to remove any dissolved
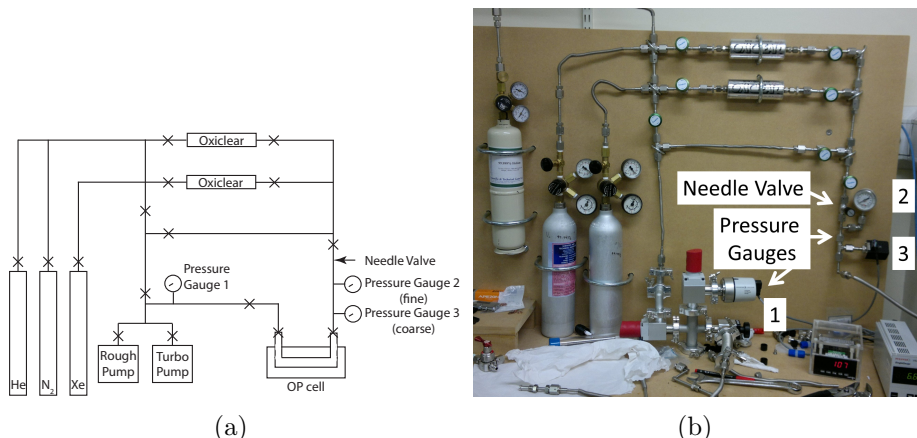
Figure 3.4: Schematic and photograph of gas loading manifold for Xe, N$_2$ and He. The numbers in the photograph refer to the various pressure gauges shown in the schematic. In (b) the rough and turbo pumps are below the table. The OP cell is on the optical table for *in situ* loading.

gases that may have been trapped during the pipette method. After the cell has cooled and been re-evacuated using first the rough pump to $\sim 10^{-3}$ torr and then the turbo pump to $\sim 10^{-5}$ torr, measured using pressure gauge 1 shown in Figure 3.4, the gas rig can be prepared for filling the OP cell. This comprises several steps. Initially the lines are evacuated and then the Alltech OxiClear disposable purifiers (AT8864) are filled for the first two gases to be loaded. The OxiClear purifier has two uses; primarily it acts to remove O$_2$, H$_2$O and organic substances to parts per billion (ppb) levels, second it acts as a storage vessel for the gas, such that the gas cylinder is closed when performing a load into the OP cell. The gas is loaded into the OP cell using the needle valve to regulate the flow whilst monitoring the pressure using gauges 2 and 3. Two gauges are needed for the precision (gauge 2) of a low density gas e.g. 100 torr, but this gauge will not provide a reading above 1250 torr, as such a coarse instrument (gauge 3) is needed to read up to the total cell pressure used in the bulk of experiments of 2000 torr.

3.2.3   Lasers

After the cell was filled with a particular gas mixture, it was aligned to the
pump laser beam. The beam size was determined by a collimating optical
lens, Figure 3.5 and the cell was positioned to the centre of the Helmholtz
coils and the pump laser beam. Various pump lasers were used for the SEOP
experiment depending on the desired experimental procedure. For example,
in Chapter 6, Rb and Cs lasers were used, namely the QPC Ultra 50 and 100
Brightlock and Brightlase. The Brightlock lasers are frequency narrowed to
~0.2 nm, whereas Brightlase lasers are relatively broadband at ~2 nm. The
broadband and narrow band lasers were utilised in section 3.5.2 to examine the
difference in buffer gas temperature with spectral profile. The spectral profile
of the frequency narrowed laser can be shifted by the use of a water cooled
chiller plate to tune the centroid wavelength of the laser by ~1 nm over the
region of interest around the alkali metal transition, Figure 3.6.

In addition, some experiments (section 6.1) utilised a flexible ~ 30 cm long op-
tical fibre output from the pump laser (Figure 3.7(b)), whereas improvements
were made with the retention of a greater percentage of linear polarisation
when a short ~ 5 cm solid fibre was utilised (Figure 3.7(a)), allowing a max-
imum amount of polarised laser light to reach the OP cell. After the pump
laser light leaves the fibre, it enters the collimating and polarising optics, Fig-
ure 3.5. Firstly, the beam is collimated to a 2.54 cm beam diameter which
then passes through the polarising cube, where linear polarised light (Figure
3.8(a)) of the correct orientation passes straight through, else it is deflected to
the beam dump. Subsequently, the vertically polarised light passes through
the $\lambda/4$ wave-plate at a 45° angle (Figure 3.8(b)), where it becomes circularly
polarised, Figure 3.8(c). This light then traverses towards the OP cell for
SEOP to occur.
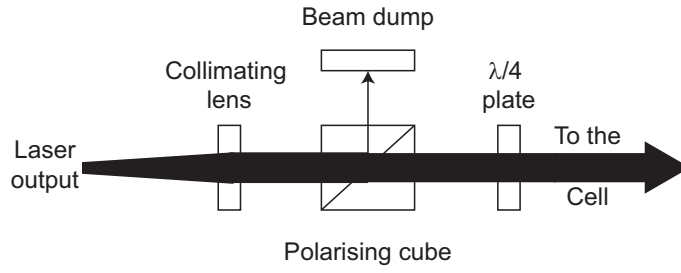
Figure 3.5: Schematic of the collimating and polarising optics used for SEOP. The thickness of the line is a representation of the amount of light passing through the optic. Initial experiments used a flexible 30 cm fibre from the pump laser to the collimating lens, this lost a maximum of $\sim 30\%$ of light at the polarising cube. The advent of the solid fibre allowed the retention of a high quantity of polarised light exiting the laser and thus less loss occurred at the polarising cube (less than $\sim 3\%$) as shown in this diagram.
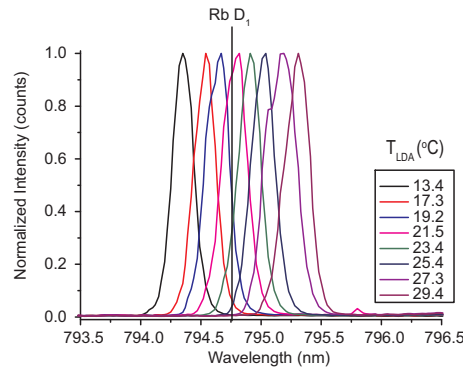
Figure 3.6: Spectral profile of frequency narrowed laser showing the tunable nature of the array by utilising a water cooled chiller plate to vary the temperature, T_{LDA}, of the laser diode array (LDA).
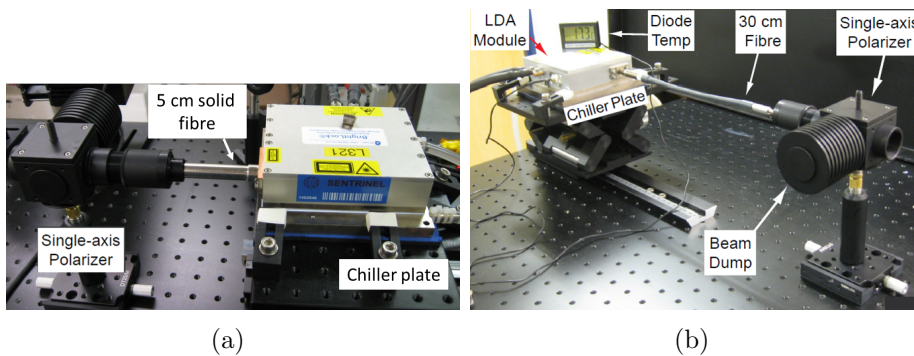
Figure 3.7: Annotated photograph of pump laser shown with a) short $\sim$5 cm solid fibre and b) long 30 cm flexible fibre along with collimating/polarising optics described in 3.5.

(a)

(b)

(c)
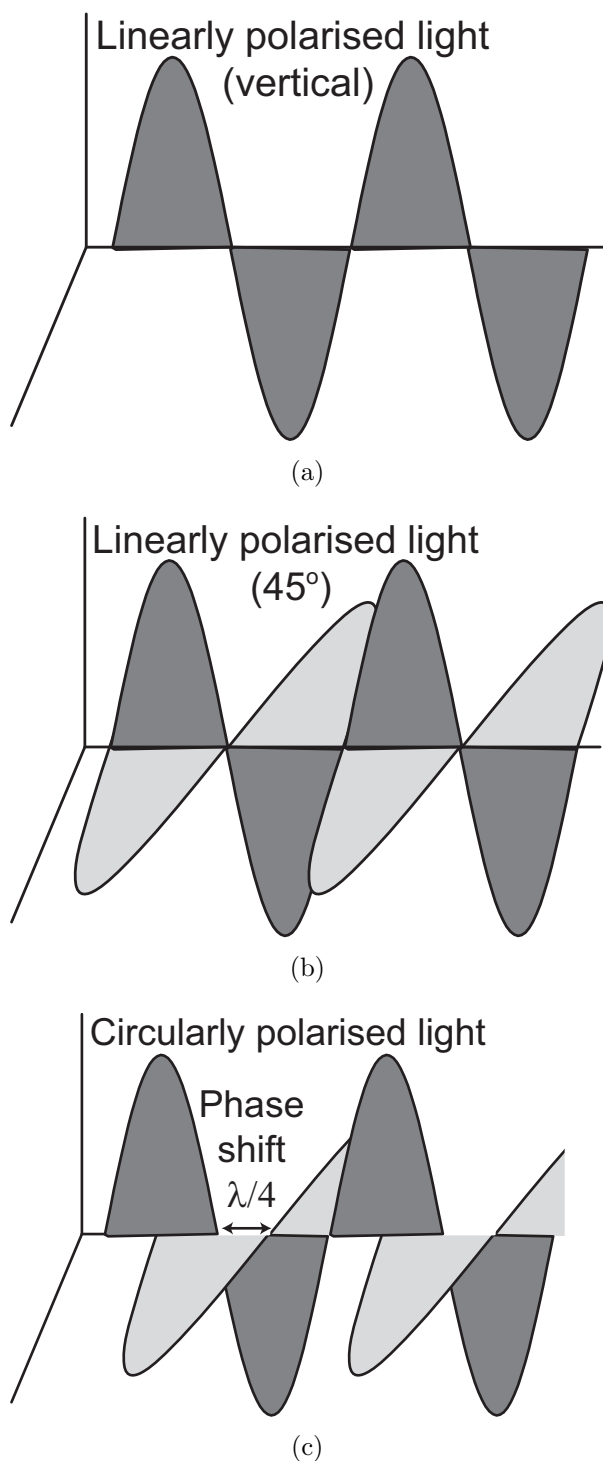
Figure 3.8: Optical waves describe the polarisation state of light. (a) A vertically polarised wave has the electric field lines only propagating along one axis. (b) Light polarised at 45° has equal amplitude and phase for both vertically and horizontally polarised light. (c) Circularly polarised light has a $\lambda/4$ phase shift of one electric field component relative to its perpendicular component.

3.3 Low-field NMR

3.3.1 Introduction

The first diagnostic technique for the SEOP experiments described herein, is low field NMR spectroscopy. This is used to measure the polarisation of ^{129}Xe nuclei. The introduction of the newly design optical cells described in section 3.2.1 along with the coil mount shown in Figure 3.3, allow for the ^{129}Xe polarisation to be spatially probed at the front, middle and back positions.

3.3.2 Spin dynamics

For a nuclear spin of spin-1/2 (e.g. ^{1}H or ^{129}Xe), applying a magnetic field B_0, splits the energy levels into two sub levels of magnetic quantum number, m_I, shown as +1/2 and -1/2 in Figure 3.9. As shown in Figure 3.9, the Zeeman splitting energy level difference is

$$\Delta E = E_{upper} - E_{lower} = \frac{1}{2}\gamma\hbar B_0 - \left(-\frac{1}{2}\gamma\hbar B_0\right) = \gamma\hbar B_0 \qquad (3.1)$$

where γ is the gyromagnetic ratio of the nucleus as shown in Table 3.1.

For a spin system in thermal equilibrium, the population difference between the spin states is shown to be [66]

$$\frac{N_\uparrow}{N_\downarrow} = \exp\left(\frac{-\Delta E}{kT}\right) \qquad (3.2)$$

where $N_\uparrow$ and $N_\downarrow$ are the populations of the upper and lower states respectively, k is the Boltzmann constant and T is the room temperature in Kelvin. The nuclear spin polarisation, $P_{thermal}$, is defined as the difference in spin po-
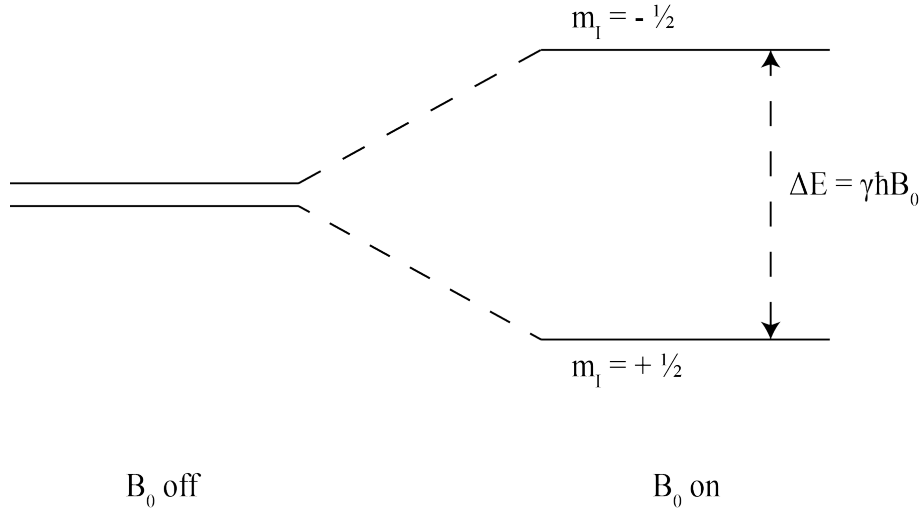
Figure 3.9: Energy levels of a spin-1/2 nucleus with a positive gyromagnetic ratio (e.g. ^{1}H) in a magnetic field. Note that for a system with a negative gyromagnetic ratio (e.g. ^{129}Xe) the magnetic quantum number, m_I, is positive for the upper state and negative for the lower state.

larisations [67]

$$P_{thermal} = \frac{N_\uparrow - N_\downarrow}{N_\uparrow + N_\downarrow} \approx \frac{\Delta E}{2kT} = \frac{\gamma \hbar B_0}{2kT} \tag{3.3}$$

3.3.2.1   Polarisation Calculation

The polarisation of a hyperpolarised xenon sample can be calculated by comparison with a proton sample by keeping the precession frequency constant and varying the B_0 by the gyromagnetic ratio of the nuclei, Table 3.1. Keeping the precession frequency constant has other additional advantages, as the Q factor and gain of the coil would vary with frequency and would complicate the calculations. In experiments shown here $B_0(^1H) = 8.4$ G, $B_0(^{129}Xe) = 30.2$ G and the frequency was 36.3525 kHz. The proton sample, in an optical cell, was doped with 10 mM of $CuSO_4$, equating to ~ 0.11 g in an optical cell with

Table 3.1: Nuclear Spin Properties from ref [20]

Nuclide	Gyromagnetic ratio, γ /MHzT^{-1}	Natural abundance
^{1}H	42.5759	0.99985
^{129}Xe	11.7769	0.2644

a volume of 68 ± 2 cm^3. This concentration gave a T$_1$ of 0.149 ± 0.002 s at Earth's field [68] which is similar to the T$_1$ experienced at 8.4 G. This allows for a lower repetition time than that required for pure water, given a T$_1$ of $\sim$ 3-4 s and the need for approximately 5 times the T$_1$ for full relaxation back to thermal equilibrium after application of an rf pulse. The proton molar concentration, c_H is 111.12 M, which is derived from utilising the molar mass of water (18 g/mol) for 1 litre (1000 g) of water, with the factor of two deriving from H$_2$O, i.e. 2 parts of hydrogen in every water molecule.

$$c_H = 2\text{x}\frac{1000 \text{ g}}{18 \text{ g/mol}} = 111.12 \text{ M} \tag{3.4}$$

The molar volume of an ideal gas at 1 atmosphere of pressure at 0°C is known to be 22.414 L/mol as shown in equation 3.5 utilising the ideal gas law.

$$V_m = \frac{V}{n} = \frac{RT}{p} = \frac{8.314 \text{ Jmol}^{-1}\text{K}^{-1} \text{ x } 273 \text{ K}}{101.325 \text{ kPa}} = 22.414 \text{ Lmol}^{-1} \tag{3.5}$$

Given the definition of the molar volume, the concentration of xenon, c_{Xe} is calculated from

$$c_{Xe} = \frac{\beta_{Xe}}{V_m} \frac{p_{Xe}}{p_{760}} \frac{T_{273}}{T_{Xe}} \tag{3.6}$$

where β_{Xe} is the natural abundance of xenon as shown in table 3.1, p_{Xe} is the pressure of xenon loaded in the optical cell, p_{760} is the pressure of 1 atmosphere, i.e. 760 torr, T_{273} is 0 °C as defined above and T_{Xe} is the temperature at which the xenon gas is loaded into the cell. Combining the elements described above, a polarisation enhancement factor, $\epsilon_{enhance}$ can be calculated to determine the enhancement of the hyperpolarised xenon signal compared to the thermally polarised proton signal. This is similar to the equations set out in Ruset's PhD [69].

$$\epsilon_{enhance} = \frac{c_H}{c_{Xe}} \frac{sin(\alpha_H)}{sin(\alpha_{Xe})} \frac{\gamma_H}{\gamma_{Xe}} \frac{S_{Xe}}{S_H} \tag{3.7}$$

where α_H and α_{Xe} are the flip angles for proton and xenon respectively as described in section 3.3.5.1, S_{Xe} and S_H are the signal intensities of the xenon and proton samples respectively. A compensation factor for T_2^*, $C_{T_2}^*$, is introduced to take into account loses in NMR signal due to the acquisition delay, T_{aq}, and T_2^*, see the SI of ref [59] for further information on this effect.

$$C_{T_2}^* = \exp\left(\frac{T_{aq_{Xe}}}{T_{2_{Xe}}^*} - \frac{T_{aq_H}}{T_{2_H}^*}\right) \tag{3.8}$$

Combining equations 3.3, 3.7 and 3.8, the xenon polarisation, P_{Xe} can be calculated.

$$P_{Xe} = \epsilon_{enhance}.C_{T_2}^*.P_{thermal}.100 \tag{3.9}$$

The largest error in the system is generally due to the proton spectrum signal to noise. The error on hyperpolarised (HP) Xe polarisation is therefore calculated from the reciprocal of the signal to noise ratio of the proton spectrum, equation

$$\text{error}_{HP} = \frac{1}{\text{SNR}} * P_{Xe} \tag{3.10}$$

3.3.3   Low field ^{129}Xe NMR methods

The requirement for a ^{129}Xe magnetic field of $\sim$30 G was created by two coils with an inner diameter (ID) of 81.28 cm placed into a Helmholtz configuration with 179 turns each, powered by a Sorenson XG80-21 programmable power supply unit, Figure 3.10(a). Calibration with a Gauss meter to measured the field at various currents supplied by a power supply, Figure 3.10(b). This field provided a resonant frequency for ^{129}Xe of $\sim$36 kHz, and this was the probe frequency generated by a Magritek Kea2 and delivered to surface coils (2.54 cm diameter) with 350 turns. A simple pulse and acquire sequence was used as shown in Figure 3.11. Pulse length and height are set along with the acquisition delay between the pulse and the collection of the signal.

(a)   (b)
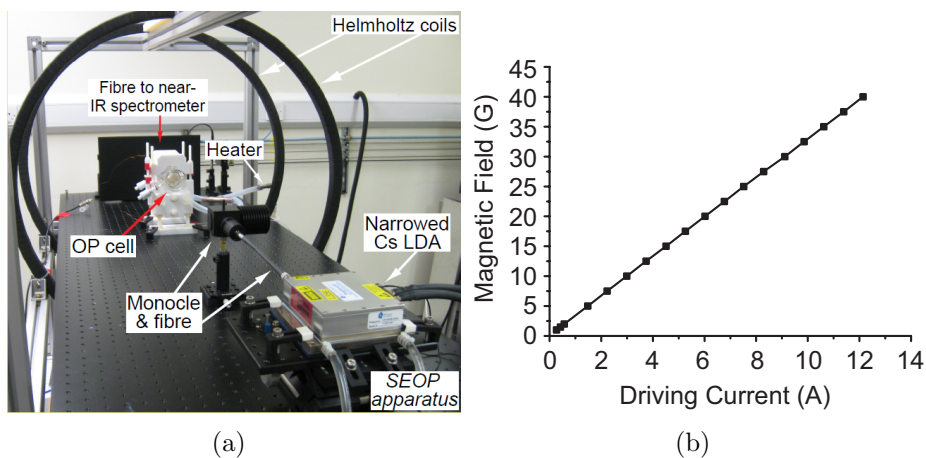
Figure 3.10: a) SEOP apparatus utilising low-field NMR but without additional detection methods such as *in situ* Raman spectroscopy. b) Calibration plot for Helmholtz Coils, produced using a Gauss meter to measure the magnetic field at increasing current.
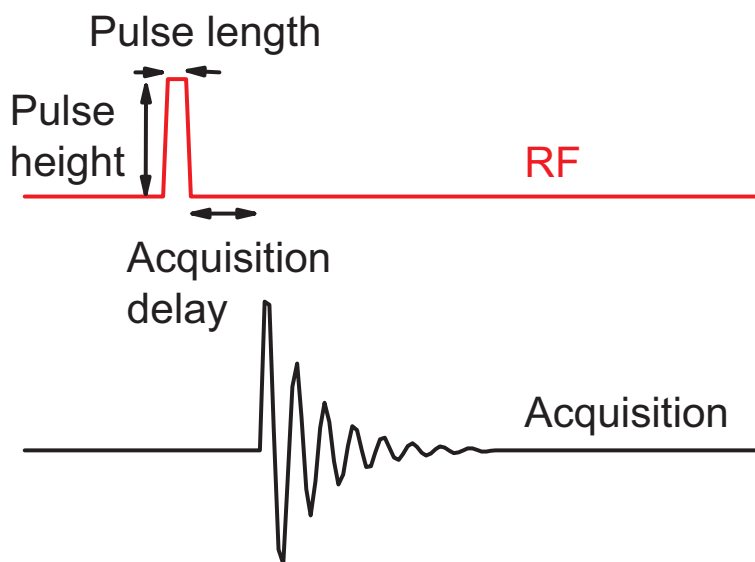
Figure 3.11: Simple pulse and acquire NMR sequence used for low field NMR acquisitions

37

3.3.4   Data analysis protocol

Subsequent to the pulse and collect NMR probe experiment, the data were automatically saved utilising the Kea2 Prospa user interface feature. This can then be implemented into a data processing program, which in this thesis is Matlab, where the data were Fourier transformed from the free induction decay (FID) and then plotted ± 1.5 kHz either side of the probe resonant frequency. Upon acquisition of a NMR spectrum, the peak maximum is taken and then utilised to calculate the ^{129}Xe polarisation present by comparison with a reference thermally polarised proton peak.

3.3.5   Calibration of polarisation

3.3.5.1   Flip angle calibration

The flip angle needed for equation 3.7 is computed by sweeping through incremental pulse durations and integrating the area under the peak at each point and then fitting a sine curve to the resulting plot to calibrate the flip angle for a set pulse duration. For the proton calibration, Figure 3.12(a), 22,464 scans were performed with 100 steps in increments of 4 μs, to determine a 90° pulse at $\sim$81 μs. This was implemented using a Magritek Kea2 NMR spectrometer with the Pulse Duration Sweep program. The repetition time was 0.5 s. The xenon flip angle calibration was performed manually using a pulse acquire program on the Kea2 NMR spectrometer, Figure 3.11. Following a 10 minute build up of hyperpolarised xenon in an optical cell, the pulse sequence was applied. Subsequently the remaining signal was killed using crusher pulses. Figure 3.12(b) shows a 90° pulse is equivalent to $\sim$260 μs pulse duration. The difference between the two 90° pulse durations acquired for ^{1}H and ^{129}Xe is due to the ratio of the gyromagnetic ratios, Table 3.1. At greater flip angles, an asymmetry of the flip angle calibration peak is observed. This is due to the
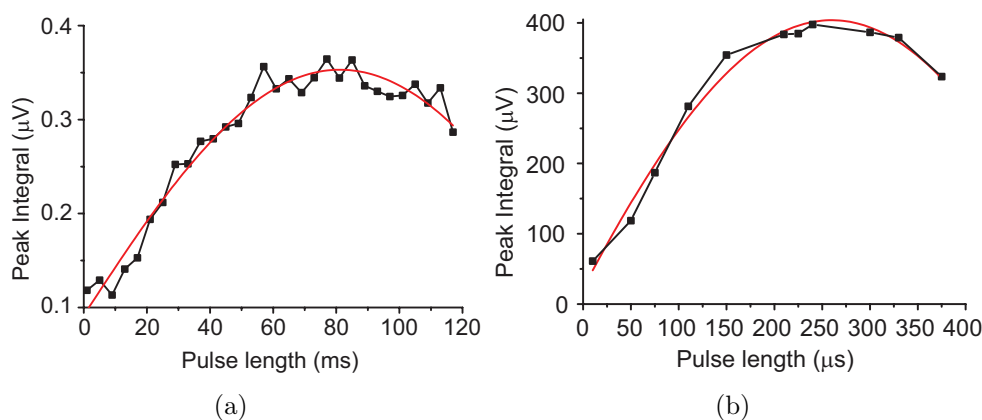
Figure 3.12: Flip angle calibration for proton (a) and xenon (b). A 90° pulse is obtained using a 81 μs and 260 μs pulse for ^{1}H and ^{129}Xe respectively.

experiment being performed on a surface coil with a small volume of interest, hence the 90° flip only occurs at one location whereas the signal is present in a larger volume.

3.3.5.2 Acquisition of reference signal

The reference proton NMR spectrum was acquired by averaging over 950,400 scans on a 10 mM CuSO$_4$ doped water sample, Figures 3.13(a), 3.13(b). The pulse duration used was 77 μs equating to $\sim 86°$ pulse, a 0.5 s repetition time, 36.3525 kHz frequency and 5 μs acquisition delay. A spectral width of 50 Hz and 4096 complex data points were acquired, resulting in an acquisition time for each FID of 81.92 μs. The same parameters were used for xenon, however, a single pulse of duration 200 μs was employed for this sample, Figures 3.13(c), 3.13(d). In later experiments, it was found that 7200 scans could be used to produce a proton signal with a signal to noise ratio which was sufficient for polarisation calculations and could be run in one hour.

(a)

(b)

(c)

(d)
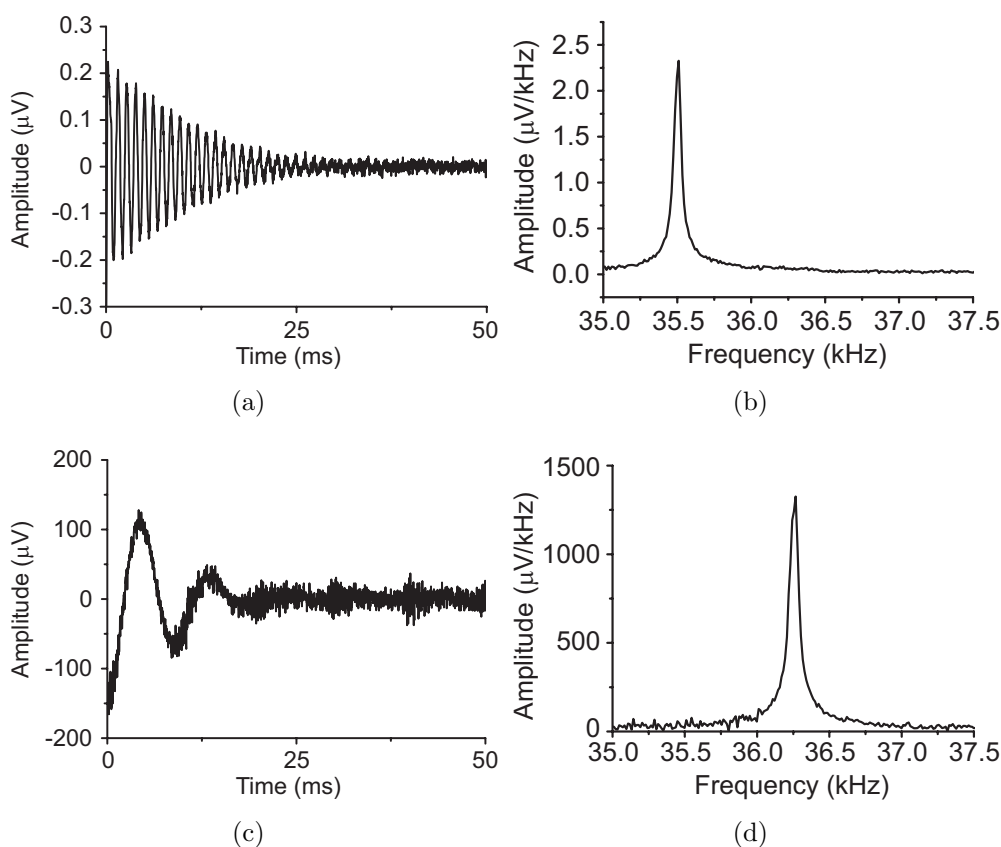
Figure 3.13: a) and b) Proton reference FID and spectrum, signal averaged to be equivalent to a single scan, acquired from 950,400 scans using a 10 mM $CuSO_4$ doped water sample using $\sim$86° pulse. (c) Single scan hyperpolarised xenon FID and (d) spectrum obtained using $\sim$74° pulse.

3.4   Optical absorption of laser light

3.4.1   Introduction

When light passes through the OP cell, it is absorbed by the rubidium electrons
via the process of optical pumping. The amount of optical absorption is a
direct measure of the quantity of rubidium vapour absorbers, due to polarised
rubidium being unable to absorb more light. Thus the Rb polarisation is also
indicated by this method, as shown by Nikolaou *et al.* in Figure 3 of ref [8].

3.4.2   Methods

An OceanOptics HR2000+ (or HR4000) fibre-coupled high resolution spec-
trometer was used to check the wavelength tuning of the lasers and to record
the optical absorption as a global quantity at a particular point in time. In
initial experiments, the data were manually saved using OceanOptics' Spec-
traSuite program, at the same time as low field NMR spectroscopy data were
recorded. However with the addition of OceanOptics' new software Ocean-
View, the user was able to set up for the spectrometer to automatically record
data at fixed time intervals for the duration of the experiment. For the later
experiments described in Chapter 5, data were recorded every 20 seconds for
30 minutes.

The optical absorption spectrometer fibre was positioned to collect reflected
light off a power meter situated behind the OP cell, Figure 3.14. The power
meter gives a second indication of the quantity of light absorbed and the two
techniques act as a verification of each other. The power meter will collect all
light without discrimination for wavelength and so is a global determination of
the light passing through the cell. The spectrometer can be tuned to accumu-
late pump laser light over a particular wavelength region, thus ignoring changes
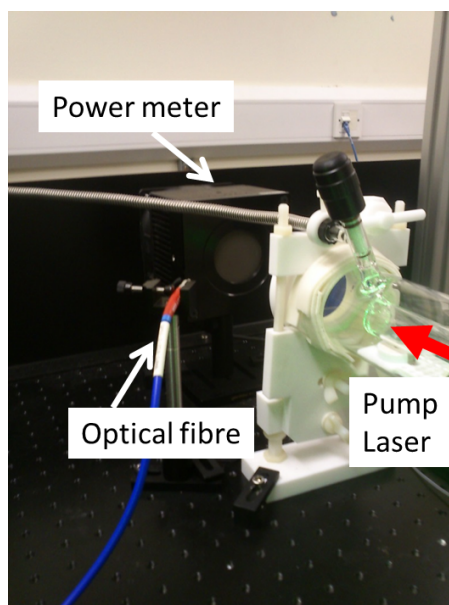
Figure 3.14: Power meter is situated directly behind the OP cell to measure the quantity of light absorbed through the cell relative to a cold cell. The optical fibre collects pump laser light scattered off the power meter into an Ocean Optics spectrometer, as a second probe.

in the environment or any unlocked output from the laser at wavelengths away from the region of interest.

3.4.3 Data analysis protocol

Upon acquisition of a full dataset of absorbed pump laser light, it was processed using a computer analysis program (Matlab) where the data were imported and then the region of interest selected. A percentage difference was calculated between the integral of the data taken and the integral of a cold cell (20°C) spectrum and then the absorption was determined as a global measurement at a specified time point.
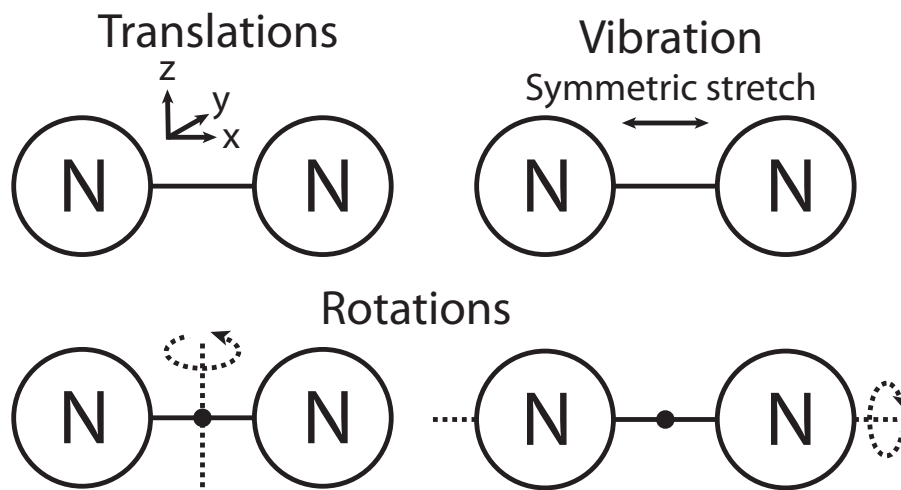
Figure 3.15: A molecule has three types of degrees of freedom: translations, vibrations and rotations. For the case of nitrogen which is a simple diatomic molecule, there are 3 translations shown as x, y and z; 2 rotations as the molecule can rotate around a point and 1 vibration which is a symmetric stretch. Note that the line shown between the two nitrogen atoms represents the nitrogen molecule's triple bond.

3.5   Measurement of N$_2$ buffer gas temperature

It has been shown by Walter *et al.* [51] that the temperature measured by the thermocouple in the oven is not representative of the temperature of the gas within the cell. For this reason, measurement of energy transport within an optical pumping cell is a very important diagnostic tool. It was discussed by Walter *et al.* that when optical pumping can be performed with little or no ^{4}He as a buffer gas and with frequency-narrowed lasers, the topic of energy transport should be revisited. In our research group, we have shown that binary mixes give high polarisations and that frequency-narrowed lasers can be utilised to give increased laser absorption and ^{129}Xe polarisations [70, 71]. The reasons for these high polarisations is not fully understood and investigations into energy transport may help to further the understanding of the SEOP process.

Within the SEOP apparatus shown in Figure 3.2(a), the outer glass cell of
the vessel forms an oven which is heated by a 400 W heat pipe and controlled
by a CAL9500 temperature control unit with a Pt100 temperature sensor at
the oven inlet positioned at the back of the cell. There is a second CAL9500
and Pt100 to monitor the oven temperature at the oven outlet near the front
of the cell. The rotational temperature of the N_2 buffer gas, T_{N_2}, can be mea-
sured using Raman spectroscopy and compared to the temperature recorded
via the thermocouple, T_{cell}. Nitrogen is the only gas in the SEOP cell able to
be used as a probe for Raman spectroscopy due to the its change in polarisabil-
ity making the diatomic molecule Raman active. A molecule is only Raman
active if it has a change in polarisability, α, upon application of an incident
electric field, E, leading to a dipole, μ, which is induced by interaction with
this linearly polarised radiation.

$$\mu = \alpha E \tag{3.11}$$

This phenomena arises from how easily the electrons are able to be moved in
response to an external electric field. Nitrogen is a centrosymmetric molecule
and its degrees of freedom for a linear molecule are shown in Figure 3.15. It
has three translational degrees of freedom which are 3 vectors (x, y, z) in three
perpendicular directions, 2 rotations due to its ability to rotate both around
and about a point and 1 vibration arising from a symmetric stretch along the
triple bond.

3.5.1   Utilising   Raman   Spectroscopy   to calculate internal gas temperatures

Figure 3.16 shows a typical Raman spectrum acquired using the orthogonal
method described in section 4.2 with a long acquisition time to obtain good
SNR. The spectrum shows the Stokes and anti-Stokes spectral lines along with
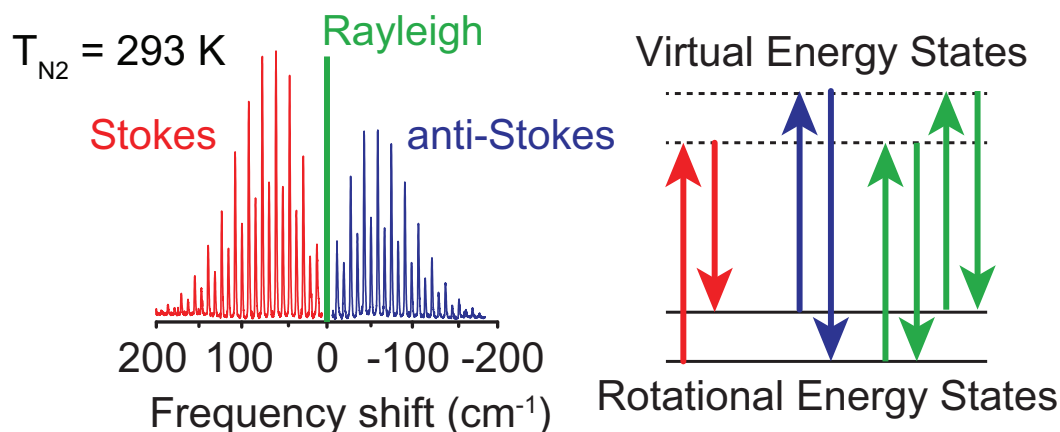
Figure 3.16: Full background corrected Raman spectrum acquired from 3 atm of N_2 in a Schlenk tube using the orthogonal method for probing and collection, acquisition time of 360 s per detection window. Stokes lines are shown in red and have a gain in energy upon return to the rotational energy level, anti-Stokes lines are shown in blue and have an decrease in energy. Rayleigh lines are shown in green as they originate from elastic collisions.
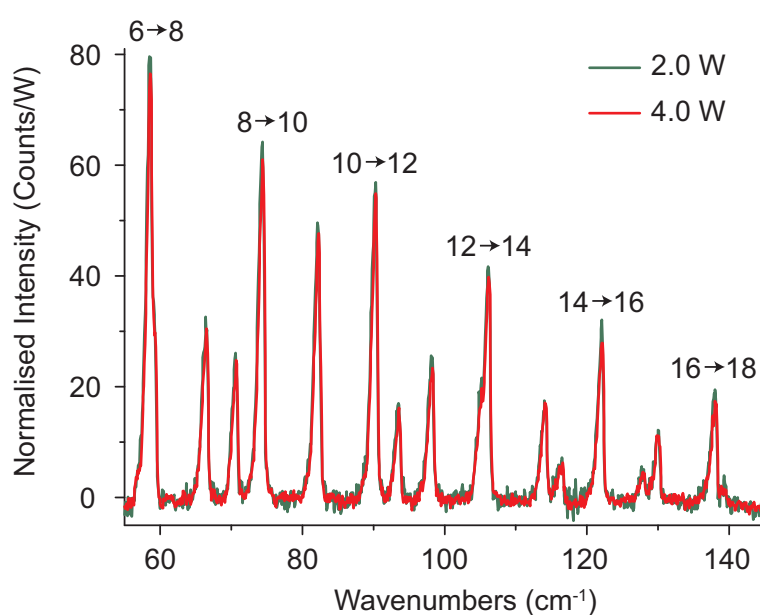
Figure 3.17: Stokes Raman spectra showing the effect of equation 3.12 where the linear increase in probe laser power causes a linear increase in Raman scattering intensity. In the plot the spectra have been normalised for the probe laser power, with the 2.0 W spectra in green and the 4.0 W in red. It can be seen that both spectra follow the same Boltzmann distribution and thus the probe laser does not induce any noticeable heating. The rotational transitions are shown for the nitrogen peaks with rotational quantum number J from its initial to final state, the transition is referred to by its initial state.

the corresponding energy level diagram. Both Stokes and anti-Stokes transitions are inelastic, whereas Rayleigh transitions are elastic. The Rayleigh transitions are much more intense than the Raman scattering, approximately only 1 in 10^6-10^8 photons lead to Raman scattering. As such the intensity of the Raman scattering needs to be improved and the Rayleigh scattering and probe laser light needs to be reduced to prevent the light from flooding the detector, this is especially important when energy levels close to the laser line are trying to be detected as is the case in this thesis. There are two methods for collecting Raman scattering, a 90° and a 180° geometry. The 90° arrangement has light passing through the sample and then collected at 90° to the probe laser through a different lens, whereas the 180° method involves light passing through the same lens to and from the sample. Raman scattering occurs uniformly in a spherically symmetric manner.

In combination with the two geometries, the intensity of the Raman lines can be manipulated according to the knowledge of the theory of Raman scattering. The intensity of the Raman scattering, $I_{scattering}$ is dependent on the power of the exciting laser, P_{laser} and the fourth power of the frequency of this source, ω along with the square of the polarisability of the molecule [72], equation 3.12:

$$I_{scattering} = P_{laser}.\alpha^2.\omega^4 \tag{3.12}$$

The signal to noise ratio (SNR) can therefore be improved by increasing the probe laser power or going to shorter wavelengths. The effect of increasing laser power to increase SNR is shown in Figure 3.17; this also proves as a demonstration that the laser is not heating the sample and artificially changing the temperature recorded via this method.

In order to calculate the rotational Raman temperature, the relative line intensity, $I(J)$, of a transition, J, is compared to the signal received by the

spectrometer, $S(J)$. A constant of proportionality, G, includes all the experimental constants (as referred to by Walter *et al.* [51]) of a particular set-up, including the volume of the nitrogen gas, cross-section of the transition, photon scattering cross-section and intensity of probe beam.

$$S(J) = GI(J) \tag{3.13}$$

The following derivation which originates from Hickman *et al.* [73] can be exploited to extract temperature information from the nitrogen Raman spectra. Firstly, we consider the relative line intensity equation for a ro-vibrational spectrum from a J to J' state:

$$I(J) \propto \nu^4 n_J P_{J \to J'} \tag{3.14}$$

where

$$n_J = g(2J+1)exp\left(\frac{-BJ(J+1)hc}{k_B T}\right) \tag{3.15}$$

and for Stokes scattering where the selection rule for the transition is defined as $\Delta J = +2$

$$P_{J \to J'} = \frac{3(J+1)(J+2)}{2(2J+1)(2J+3)} \tag{3.16}$$

where J is the rotational quantum number, ν is the frequency of the rotational line (assumed to be constant over the range that we work in), g is the ground state degeneracy due to nuclear spin, B is the rotational constant for N$_2$ ($\sim$ 2 cm^{-1}) [74] see Appendix A, c is the speed of light, and k_B is Boltzmann's constant.

Starting from equation 3.14, the proportionality relation can be removed by utilising a constant, for example C:

$$I(J) = C\nu^4 n_J P_{J \to J'} \tag{3.17}$$
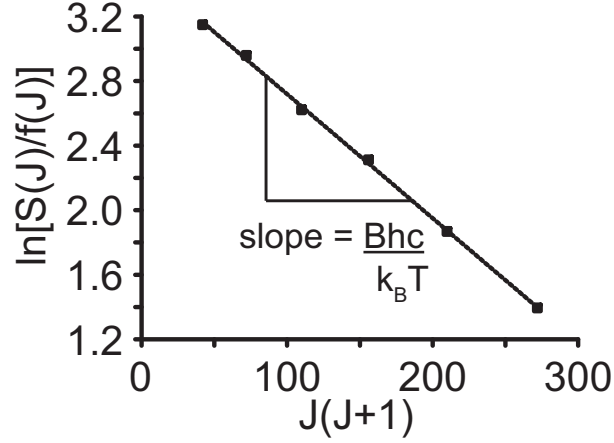
Figure 3.18: A sample plot of equation 3.27 from which the temperature of the nitrogen gas, T_{N_2}, can be calculated, where $S(J)$ is the signal intensity of a particular line with rotational quantum number J, $f(J)$ is defined in equation 3.21.

If we make $C = 1/G$ where G contains all experimental optical factors as described above, then we arrive at equation 3.18.

$$S(J) = I(J)G = \nu^4 n_J P_{J \to J'} \tag{3.18}$$

From equation 3.18 we can substitute in equations 3.15 and 3.16.

$$S(J) = g\nu^4(2J+1)exp\left(\frac{-BJ(J+1)hc}{k_BT}\right)\frac{3(J+1)(J+2)}{2(2J+1)(2J+3)} \tag{3.19}$$

Cancelling out the $(2J+1)$ terms,

$$S(J) = g\nu^4 exp\left(\frac{-BJ(J+1)hc}{k_BT}\right)\frac{3(J+1)(J+2)}{2(2J+3)} \tag{3.20}$$

Simplifying equation 3.20 using $f(J)$,

$$f(J) = \frac{3(J+1)(J+2)}{2(2J+3)} \tag{3.21}$$

Following through we arrive at equation 3.26.

$$S(J) = g\nu^4 f(J)exp\left(\frac{-BJ(J+1)hc}{k_BT}\right) \tag{3.22}$$

$$\frac{S(J)}{g\nu^4 f(J)} = exp\left(\frac{-BJ(J+1)hc}{k_B T}\right) \tag{3.23}$$

$$ln\frac{S(J)}{g\nu^4 f(J)} = \frac{-BJ(J+1)hc}{k_B T} \tag{3.24}$$

$$ln\frac{1}{\nu^4} + ln\frac{S(J)}{g f(J)} = \frac{-BJ(J+1)hc}{k_B T} \tag{3.25}$$

$$-J(J+1)\frac{Bhc}{k_B T} = ln\frac{S(J)}{g f(J)} + 4ln\frac{1}{\nu} \tag{3.26}$$

It is possible to translate a spectrum of Raman peaks (Figure 3.16) into a rotational temperature measurement, taking the peak heights, $S(J)$ for six even J Stokes line ($J = 6, 8, 10, 12, 14, 16$). Taking equation 3.26 with $g = 1$, and comparing to the equation of a straight line, a plot can therefore be created with a linear fit

$$J(J+1) \text{ versus } ln\frac{S(J)}{f(J)} \tag{3.27}$$

enabling T to be determined as illustrated in Figure 3.18, with the slope equal to $Bhc/k_B T$.

3.5.2   Methods

In this thesis, two contrasting methods were investigated for measuring the rotational temperature of the N_2 gas using Raman spectroscopy. This has lead to two publications within our research group by Newton *et al.* [11] and Whiting *et al.* [10]. The two experimental setups will be discussed in more detail in Chapter 4 with a brief overview only presented in this section. The probe laser light has to travel through collimating optics and then onto the sample, denoted by a star in Figure 3.19. When Raman scattering occurs at the sample it will uniformly distribute scattered light in a spherical arrangement in all directions. Therefore, there is flexibility as to where the experimentalist
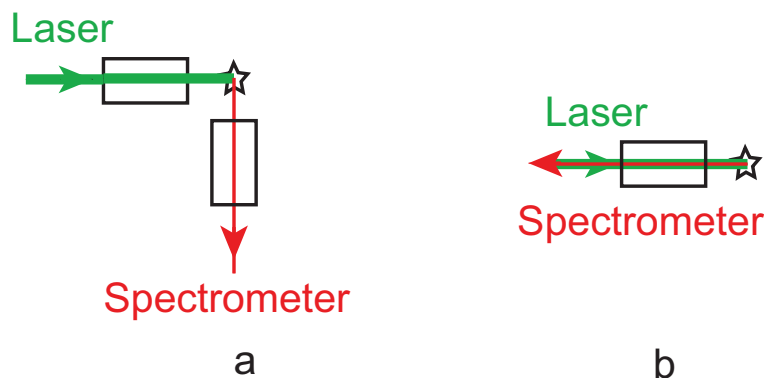
Figure 3.19: Spatially variant setups for Raman spectroscopy. The star represents the sample, the arrows denote the direction of light travel through the fibres, green is laser input and red is the Raman scattered light. The boxes represent the optics needed for expansion, collimating and beam separation. a) is a 90° arrangement, b) is a 180° inline module where the same optics are used for transmitting and receiving light.

wishes to collect and detect this light. In one of two main methods of collection, light is collected perpendicular to the probe laser beam such that the laser is spatially filtered from the collection optics and doesn't enter into the spectrometer; this is easier than placing the detection optics behind the initial optics as the spectrometer will be flooded with probe laser light and the less intense Raman scattered light (compared to the Rayleigh and probe light) will be hard to detect. This first method, Figure 3.19(a), utilises simple optics but it difficult to spatially align due to sub-mm accuracy and may drift over time. The second approach, which is self-aligning, leads to increased SNR due to the pump and probe regions being identical as they follow the same optical path which is not true for the orthogonal method, Figure 3.19(b). This enables quick and simple alignment but expensive optics are needed to block the probe laser light from re-entering the module and the spectrometer.

3.5.3   Data analysis protocol

This section aims to inform the reader about the process required to quickly analyse data collected from a Raman spectrometer. Initially the data were analysed manually using BioRad Knowitall for baseline correction, OriginPro
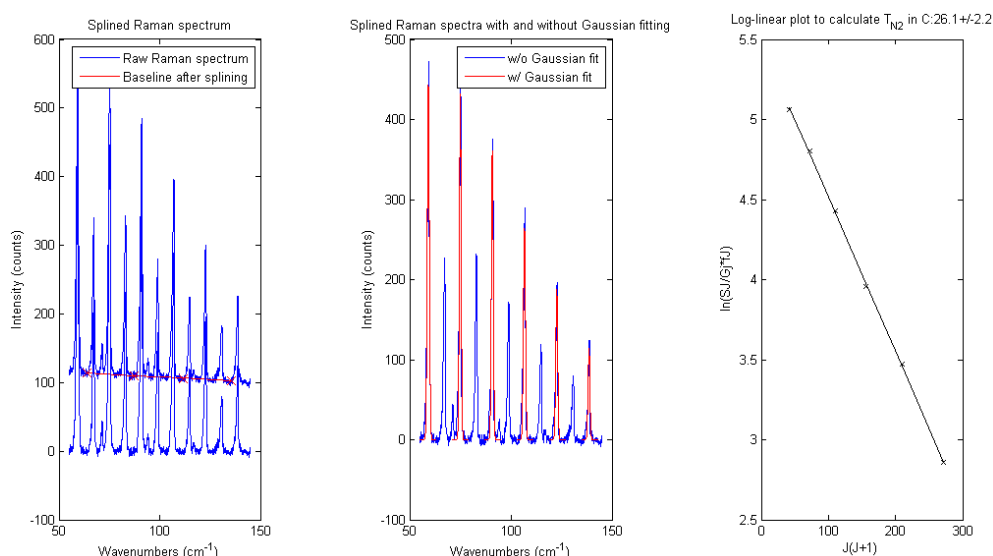
Figure 3.20: Original data which have had a baseline correction programmatically applied, followed by Gaussian fitting, giving a temperature of 26.1 $\pm$ 2.2°C, for a measured cell thermocouple temperature of 25 °C.
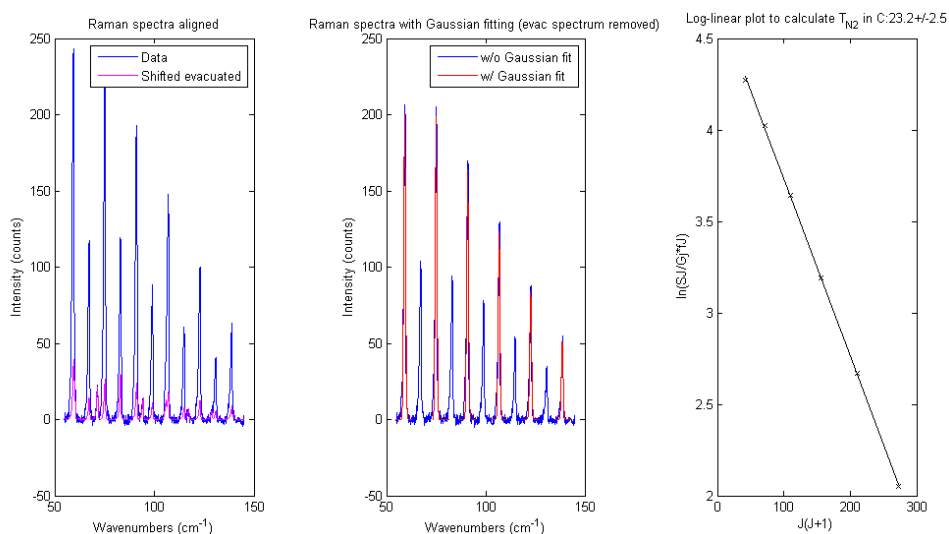
Figure 3.21: Data analysed using all the techniques reported in section 3.5.3: baseline correction, oxygen peak removal using an evacuated cell spectrum allowing removal of Raman scattering along the optical path and consideration of the transmission efficiency for filters in the in-line module. A cumulative of these methods gives a calculated temperature of 23.2 $\pm$ 2.5°C, for the same spectrum shown in Figure 3.20 with a cell thermocouple temperature of 25°C.

for Gaussian fit to the Raman peaks and Microsoft Excel for temperature cal-
culations, but then the process was simplified and the processing time reduced
by automating this process in a Matlab program. In an experiment in which
a total of 93 Raman spectra, collected every 20 seconds over a 30 minute time
period, analysis could be completed in a few minutes rather than many hours.
The automation also allowed the inclusion of some other features such as the
removal of a scaled, shifted evacuated cell spectrum to eliminate the back-
ground oxygen peaks along the optical train of the inline module box and the
inclusion of the transmission efficiency of the filters within the in-line module.
The automation of the analysis of a Raman spectrum from a raw text file di-
rect from the spectrometer to a temperature result with its associated error is
described, including the steps of background correction and Gaussian fitting
of the even J value Raman Stokes spectral peaks. All examples shown in this
section are in the absence of spin-exchange optical pumping. The Matlab code
is performed following the series of steps shown below.

Following cosmic ray removal described in section 3.5.4.4, a correction is ap-
plied for the transmission efficiency of the filters supplied from Ondax:

$$\text{corrected intensity} = \left(-4 * 10^{-9}x^2 + 8 * 10^{-5}x - 0.5201\right) * \text{intensity} \quad (3.28)$$

where x is in wavenumbers relative to 532.21 nm as the central wavelength.
See Figure 3.21 for implementation of this filter correction. Next the data are
baseline corrected, similar to the process applied in BioRad Knowitall, but au-
tomated into the Matlab code. Four noise regions in the spectrum are located
and a line is fitted through these regions, this line is subsequently removed
from the spectrum, see left part of Figure 3.20.

When the inline module is utilised, a small amount of Raman scattering is
collected from the optical path as well as the focal point of the laser, due to

52

atmospheric oxygen and nitrogen. The method for removing this is to collect a Raman spectrum from a evacuated cell, $\sim 10^{-5}$ torr, which was acquired over 30 minutes and averaged over two scans to remove cosmic rays. This can then be compared to the data spectrum following baseline correction and the optical path Raman spectrum can be removed. Slight spectral drift of the spectrometer means that the two spectra need to be lined up, this is done by the nitrogen peak locations being found in both the evacuated cell and data spectra. A scaled evacuated cell spectrum is then produced by taking the ratio of the peak heights of the oxygen peaks present in both datasets. Subsequently a difference spectra is calculated from the data spectrum and the shifted, aligned evacuated cell spectrum, see Figure 3.21.

A Gaussian fit is applied to the even J value N_2 peaks in the difference spectrum using a non-linear least squares fit and the max peak heights are recorded. The rotational temperature is calculated according to the equations in section 3.5.1. The error on the temperature is computed from the reciprocal of the signal to noise of the data spectrum multiplied by the temperature.

3.5.4   Calibration techniques

3.5.4.1   Wavelength calibration of Raman spectrometer

The wavelength of the Raman spectrometer was calibrated using an OceanOptics CAL-2000 light source with a Hg/Ar high pressure gas discharge light. The Hg/Ar source has many sharp peaks which are commonly used to tune an instrument to a particular wavelength. Several lines in the spectrum were chosen as being close to the probe laser line (532 nm), these were 435.833, 546.074 and
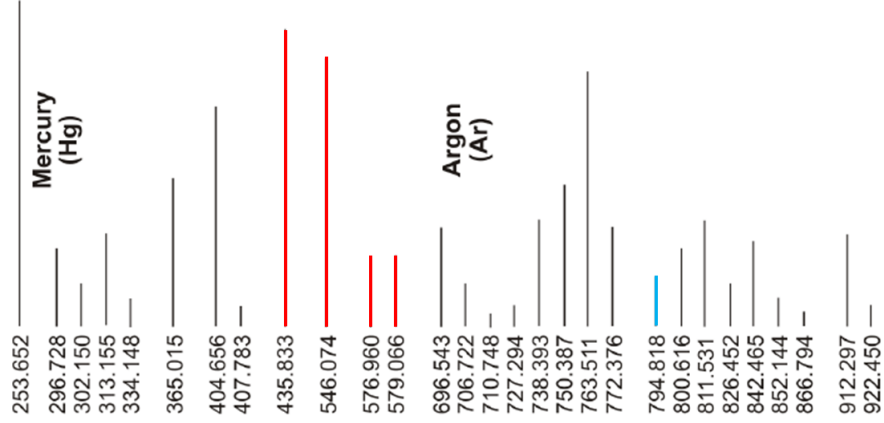
Figure 3.22: Calibration lines for a mercury argon source. Red lines denote lines used for Raman spectroscopy calibration and the blue line is for the calibration of the optical spectrometer for the pump laser light. Figure adapted from CAL2000 manual [75].

a pair of doublets at 576.960 and 579.066 nm, red lines in Figure 3.22. This allowed the correct wavelength to be set on the spectrometer; a similar process was also performed on the HR2000+/4000 spectrometers to ensure that the correct wavelength for the Rb D_1 transition was found, for example by using the Hg/Ar peak at 794.818 nm, blue line in Figure 3.22.

3.5.4.2   Verification of in-cell temperature

Two thermocouples (Pt100) were placed into the SEOP oven with one in the oven inlet to control the oven temperature and one in the oven outlet to monitor the out-going air temperature. This allows the oven temperature gradient to be measured, with the mean of these two values giving T_{cell}. The temperature calculated from the Raman spectra, T_{N_2}, was calibrated by varying the temperature of the oven, T_{cell}, with no pump laser, i.e. no spin exchange optical pumping taking place. T_{cell} was compared to T_{N_2}, as shown in Figure 3.23. This shows a good correlation between the two values so no calibration factor is needed.
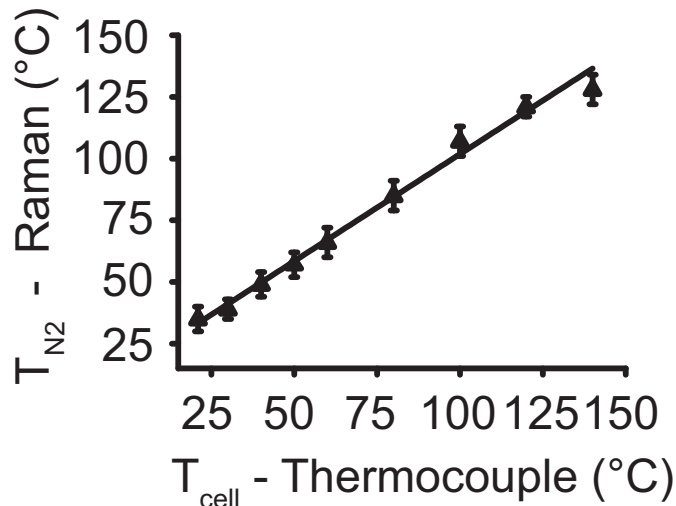
Figure 3.23: A calibration plot for T_{N_2} and T_{cell}, this was repeated for front, middle and back positions and repeated five times for each position. This demonstrates that the temperatures recorded utilising the Raman spectrometer are reliable, due to a R^2 value of 0.99.

3.5.4.3 Background spectra removal

The validity of removal of the air contribution along the optical path and oven via the subtraction of a Raman spectrum acquired from an evacuated optical cell is shown in Figure 3.24. It can be seen how the evacuated cell spectrum peaks are programmatically aligned to the position of the peaks from the data spectrum and the heights of the peaks are scaled proportionally. These methods are further confirmed in Figure 3.25, where a residual plot is shown for measurements at the front, middle and back of the cell and repeated five times at each position. The dashed line shows the temperature recorded by the thermocouple in the oven inlet and outlet (25°C). The application of the removal of the evacuated cell spectrum lowers the temperature deviation and this is further lowered by the inclusion of the efficiency of the filters, such that the accuracy of the temperatures increases with the implementation of these additional analysis tools.
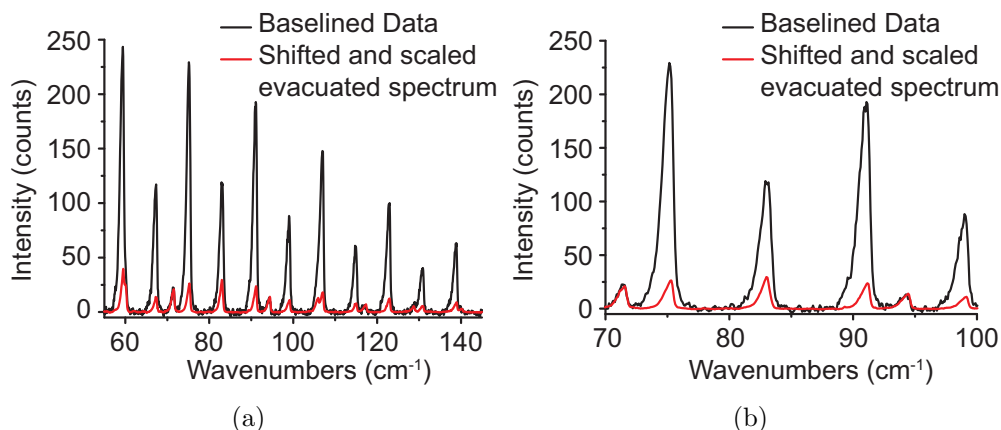
Figure 3.24: a) Spectrally aligned and scaled evacuated spectrum with data spectrum. b) Zoomed in version of (a).
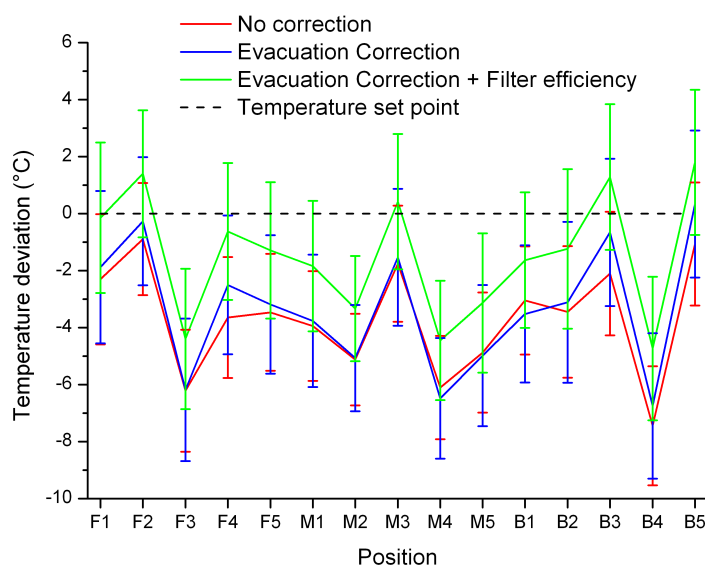
Figure 3.25: Residual plot for 25°C data spectra at 3 positions in cell front (F), middle (M) and back (B), repeated 5 times at each position.
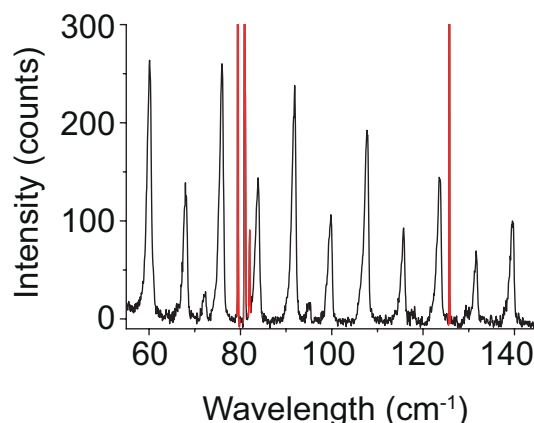
Figure 3.26: A typical Raman spectrum shown with cosmic ray peaks highlighted in red.

3.5.4.4   Cosmic rays

High energy particles called cosmic rays are often detected with the charge
coupled device array detector (CCD). These manifest on a Raman spectrum
as a sharp peak or spike of high intensity counts as shown in Figure 3.26.
As they are distinctive from the Raman scattering peaks they can be easily
removed by cosmic filtering. Cosmic filtering is performed before any other
data processing and can be carried out by a variety of methods including using
in-built programs on the instrument computer which requires two successive
scans to be taken and the lowest intensity pixel being recorded, however, this
doubles the acquisition time needed for each scan, so neglects the 'real-time'
nature of the experiment. We used a different cosmic filtering method in
which cosmic ray peaks are manually removed post experiment using an in-
built computer tool on the Horiba LabSpec program.

3.5.5   Temperature dependence of absorption
coefficient

In this section, the variation of absorption coefficient with temperature is ad-
dressed. It has been noted that as the temperature increases, the signal to

(a)   (b)
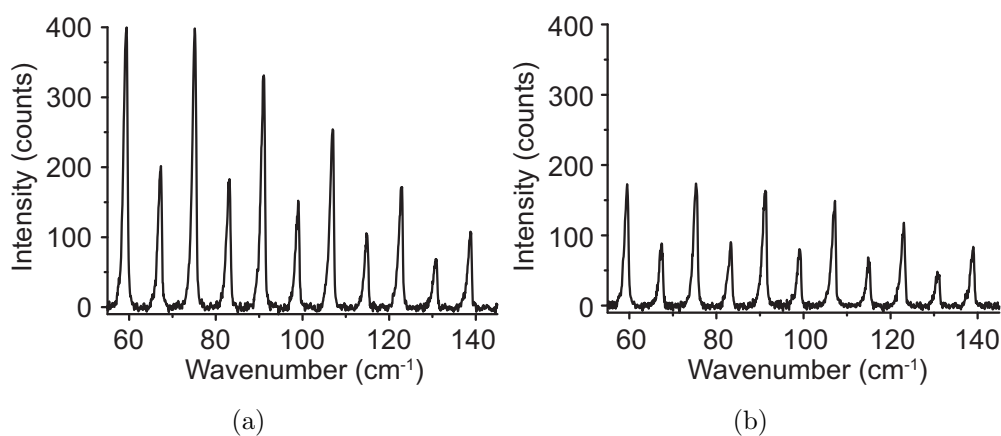
Figure 3.27: Comparison of intensities and corresponding absorption coefficient with temperature: a) 25°C and b) 150°C Raman data spectrum.
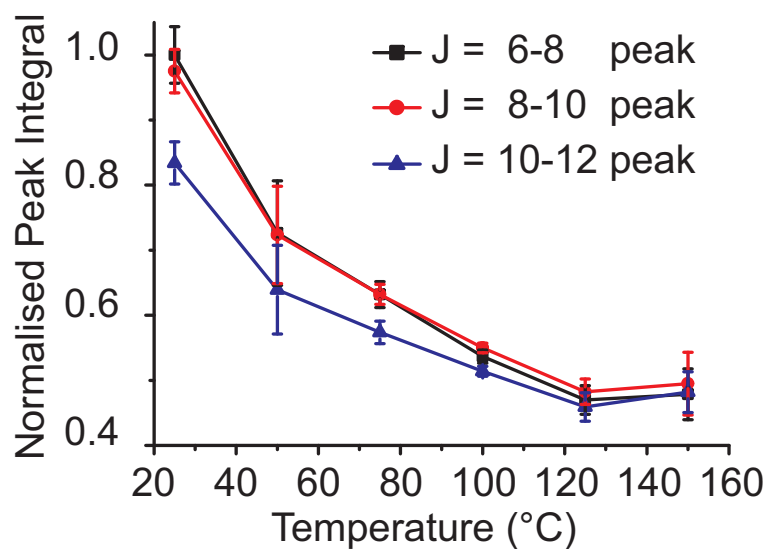
Figure 3.28: Normalised relative absorption coefficient dependence with temperature

noise drops, as the intensity of the Raman peaks decreases, as illustrated in
Figure 3.27.

The Beer-Lambert law describes the absorbance of a material [76–78],

$$I = I_0 exp(-k(\nu)l))$$ (3.29)

where radiation of intensity I travels through a sample of length l with an
absorption coefficient, k which is a function of the wavenumber, ν. The total
strength of a transition is known [76] to be $\int k(\nu)\delta\nu$, such that the sum of
relative Raman scattering cross-sections can be determined from the integrated
peak areas as discussed by Simonelli and Shultz [79]. They showed that as the
temperature of a sample increases (in their case an ammonia/water complex),
the cross-section of the transition decreases, this is shown in our experimental
data in the absence of spin-exchange optical pumping, in Figure 3.28.

3.6   Data reproducibility

It is imperative to ensure that experiments are reproducible. As a quality con-
trol, some experiments were repeated several times and analysed to compare
the data. It was noted that the data were comparable within experimental
error. A sample plot of this quality control is shown in Figure 3.29 where intra
cell reproducibility was tested by running the same experimental conditions
on the same cell. The open and closed symbols represent the two repeats and
it can be seen that the data agree within the spread of the error bars.

(a)   (b)
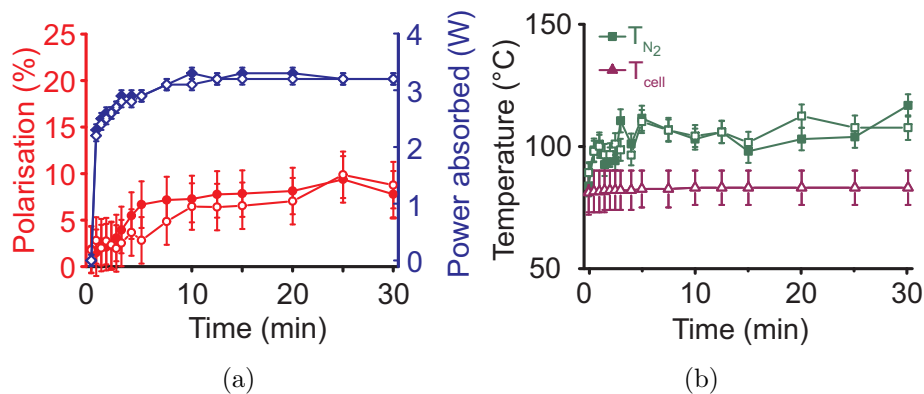
Figure 3.29: Repeatability checks were carried out by performing the same experiment several times on one set of experimental conditions, an example of which is shown here. ^{129}Xe polarisation is denoted by red circles, power absorption measurement by blue diamonds, thermocouple temperatures by purple triangles, and T_{N_2} by green squares. The two experiments shown here are indicated by open and closed symbols; good repeatability is shown within experimental error.

3.7 Summary

This chapter has laid out the theory and methods for the majority of experiments performed within this thesis, including the processes required for loading an optical pumping cell with alkali metal and gas along with the techniques to probe the experimental parameters within a dynamic system. These include low field NMR spectroscopy, optical absorption using a power meter and an optical spectrometer and Raman spectroscopy to measure the temperature of the nitrogen gas within the cell. Raman spectroscopy will be discussed in more detail in the next chapter where two contrasting methods will be debated which have resulted in two publications for the author.

Chapter 4

in situ Raman spectroscopy geometries to probe in-cell energy transport

4.1 Introduction

Energy transport within a SEOP cell is a useful quantity to examine as many of the spin exchange and spin destruction terms have temperature, T, dependent aspects. There is an expected $T^{0.3}$ dependence on the Rb absorption line shift, asymmetry and line broadening which varies with Xe and N_2 density arising from the van der Waals model [80]. As the temperature within the OP cell varies, the diffusion coefficients, viscosity and heat conductivity of the various gases alter [81]. In addition, the alkali metal number density will increase with rising temperature. Utilising the ideal gas law and vapour pressure equations the Rb number density, [Rb] in units of m^{-3}, as a function of T can be computed [81–83]. The Rb vapour pressure, p, is valid in the range from the melting point of Rb to 550 K according to Alcock [83].

$$[Rb] = \frac{p}{k_B T} \tag{4.1}$$

$$[Rb] = \frac{10^{9.318-4040/T}}{k_B T} \qquad (4.2)$$

Wagshul and Chupp [84] found that the actual Rb number density varied by about a factor of 2 from the predicted vapour pressure curves (Figure 2.5) from apparent uniform temperature distributions, measured from a cell wall thermocouple, T_{cell}. Fink *et al.* [81] showed numerical simulations of non-uniform temperature and xenon polarisation distributions within the OP cell. Consequently, Six *et al.* [82] proposed that the divergence between the theoretical and observed noble gas polarisations could be due to the temperature not being well characterised between the internal gas temperature and T_{cell}.

Raman spectroscopy can be used to probe these energy transport considerations by examining the ro-vibrational manifold of nitrogen, as discussed in section 3.5. Walter *et al.* [51] showed that the temperature measured by a thermocouple in the oven (T_{cell}) was not reflective of the gas temperatures experienced during the OP process (T_{N_2}). In particular towards the end of the paper, they noted that when optical pumping could be performed with significantly good polarisation without the use of helium as a buffer gas and with high powered frequency-narrowed lasers, the topic of energy transport should be revisited.

In addition to the work carried out by Walter *et al.*, Fink *et al.* [81, 85] have performed simulations and experimental comparisons of transport processes in SEOP experiments. Oven temperature, xenon and nitrogen density, and laser power were varied as key hyperpolarisation parameters, particularly interesting is the spatial distribution maps presented in [81] which show the convection patterns of the spin polarisation that occur at increasing temperatures.

(a)   (b)
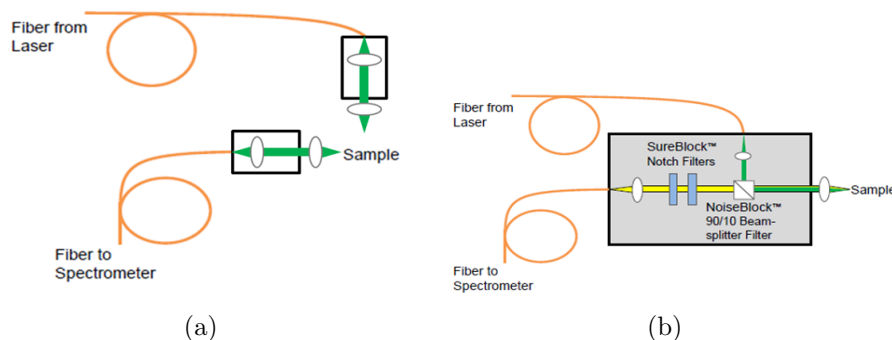
Figure 4.1: Schematics of the two contrasting Raman arrangements, a) a simple orthogonal set-up utilising spatial filtering with two modules which have to be a set distance from each other at a 90° geometry. b) Optical filters are utilised to remove Rayleigh scattering and laser reflections, thus enabling an in-line module with a 180° collection geometry.

Evidence of laser heating was also shown by Parnell *et al.* [86] via the use of NMR diffusion gradients. This gave a method to examine the temperature and pressure of the gas during ^{3}He SEOP, the authors describe the additional challenges required to perform the same treatment on ^{129}Xe SEOP due to the lower gyromagnetic ratio resulting in a decreased NMR sensitivity and the lower diffusion coefficient of ^{129}Xe necessitating stronger NMR gradients.

This chapter builds on the discussion presented in section 3.5.2, where two contrasting methods for exploring Raman spectroscopy were presented in Figure 3.19. Firstly a 90° optical Raman arrangement will be discussed, Figure 4.1(a). Followed by a 180° optical Raman instrument which was designed in collaboration with Ondax Inc., Figure 4.1(b).

4.2   90° Optical Raman Arrangement

The work in this section is a manuscript in preparation for submission [10], with the author of this thesis being a co-author of this work.

Following on from the work by Walter *et al.* [51], our initial Raman studies utilised a 90° set-up as shown in Figure 4.2. The orthogonal arrangement
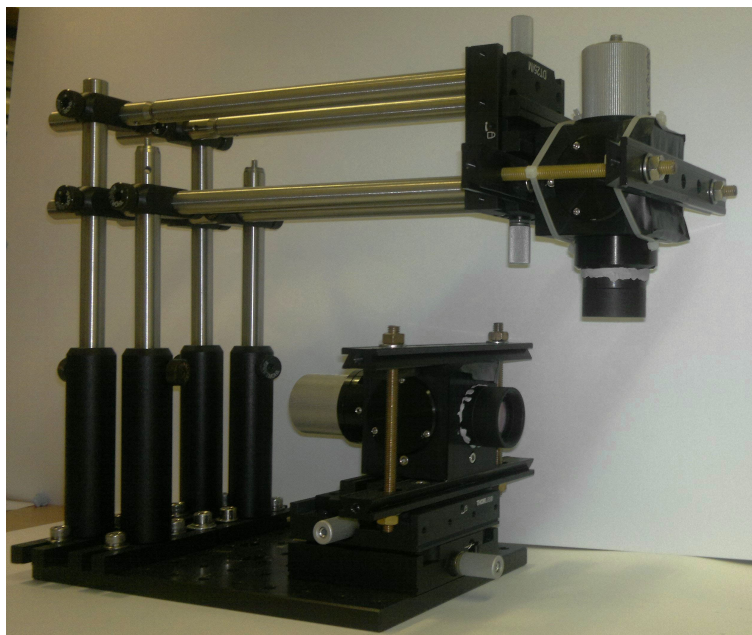
Figure 4.2: Photograph of the orthogonal set-up showing the position of the excitation and detection modules and the struts required to hold them in place.

consists of two modules placed at 90° to each other, one module is for excitation and the other for detection of Raman scattered light, Figures 4.2 and 4.3. The two modules have several purposes, firstly they were used to support fibre collimation. In addition, one unit houses a lens to focus the 532 nm 5 W probe laser light (Verdi V5 Coherent) onto a point inside the OP cell, whilst the second unit collects the scattered light through a lens which then travels to the Raman spectrometer (Horiba-Yvon U1000) for analysis. The U1000 Raman spectrometer, Figure 4.4, is a double additive monochromator with a long 2 x 1 m focal length and ultra high spectral resolution, this allows for Stokes and anti-Stokes line to be obtained close to the laser line.

Translational stages are positioned beneath both modules to enable optical alignment to less than 1 mm accuracy. These two modules act as spatial filtering, as the probe laser light is not directly collected. However, reflections and Rayleigh scattering will be detected, accordingly a second layer of filtering is applied at the spectrometer. Upon entry into the Raman spectrometer,
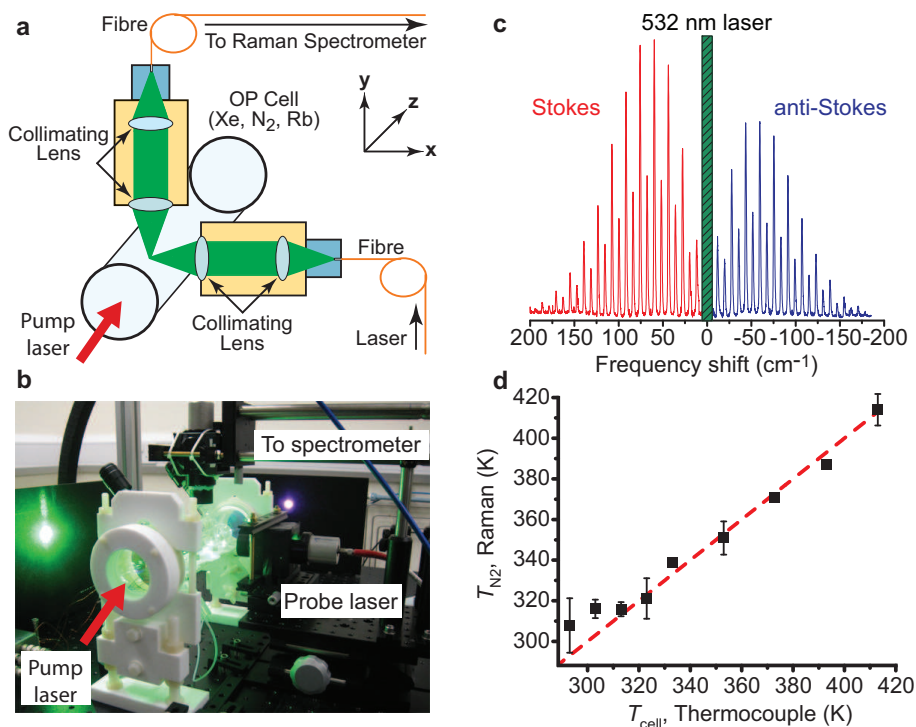
Figure 4.3: a) Schematic of orthogonal set up, with b) corresponding photograph *in situ* with OP cell, c) a typical Raman spectrum showing both Stokes and anti-Stokes scattering and d) a temperature calibration curve for T_{cell} and T_{N_2}. Figure adapted from ref[10].
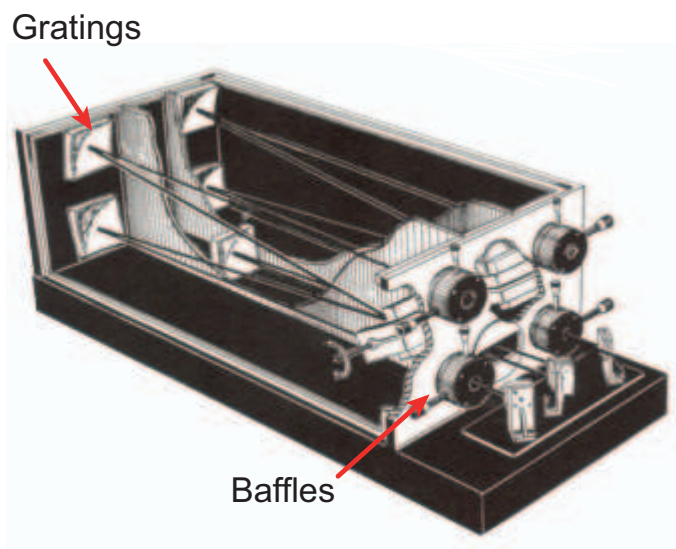
Figure 4.4: Illustration of a double additive monochromator for a U1000 Raman spectrometer. The gratings can be seen which disperse the light. The baffles are used in the 90° method to remove the probe laser light as a physical filter by blocking the light. Figure from ref [87].
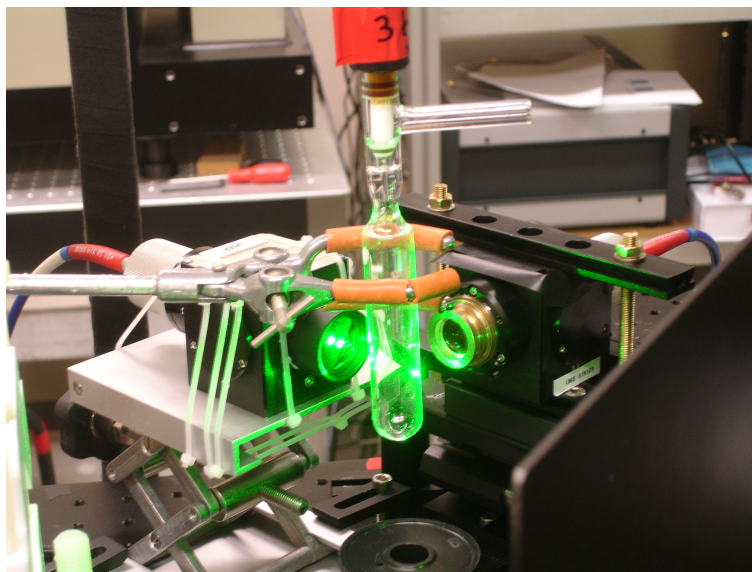
Figure 4.5: Photograph showing experiments performed using the 90° arrangement on a Schlenk tube containing 3 atm of N_2. This was used to obtain optimum performance of the Raman spectrometer for testing out protocols.

the light is diffracted and thus physical blocks known as baffles between the two stages can be used to block out the probe laser light and prevent it from reaching the CCD detector, Figure 4.4. This results in a Raman spectrum from either the Stokes or anti-Stokes scattering. Figure 4.3(c) shows a baseline corrected Raman spectrum acquired from initial experiments performed on a sample of 3 atm of N_2 held in a Schlenk tube, Figure 4.5 over a time period of 360 s per acquisition window, ~ 100 cm^{-1}. Due to the baffles within the spectrometer this spectrum was performed from two separate acquisition windows, the first window was to remove the probe light and the anti-Stokes lines. The second was to remove the probe light and the Stokes scattering, this resulted in a cumulative spectrum as shown in Figure 4.3(c).

After initial optimisation of the 90° method with the Schlenk tube, a temperature calibration was preformed under conditions of no spin exchange optical pumping, as discussed in section 3.5.4.2. Experiments were performed by heating the oven air to set temperatures, T_{cell}, and then comparing with the

calculated N_2 temperatures recorded from the Raman spectra, T_{N_2}. This was
repeated five times at three locations across the SEOP cell to ensure repeatability. A sample plot is shown in Figure 4.3(d), good agreement is seen between
the surface thermocouple measurements, T_{cell} and T_{N_2} values. Following on
from the optimisation and calibration, SEOP experiments could be performed
using this set-up. These include effects of P_{Xe} and T_{N_2} which were studied
for different Xe/N_2 gas mixtures and laser power; longitudinal position within
the OP cell on P_{Xe} and T_{N_2}; and polarisation build up curves over time with
varying T_{cell}.

4.2.1 Experiments performed using 90° Raman arrangement

Several experiments were performed with the orthogonal Raman arrangement
with a ~70 W, ~0.25 nm full width half maximum (FWHM) tunable frequency
narrowed Rb D_1 laser. *In situ* ^{129}Xe polarisation and T_{N_2} were monitored during studies. Due to the forced air oven being heated from the back and the
removable windows creating heat loss, a temperature gradient across the cell
was experienced of about 30-40°C. In experiments described here, T_{cell} refers
to the rear thermocouple in the oven inlet.

In situ monitoring of P_{Xe} and T_{N_2} on a comparison of Xe/N_2 gas mix ratios was
explored for different laser powers, Figure 4.6. Increased laser powers led to
elevated ^{129}Xe NMR signals, this is indicative of the current setup being laser-power limited for P_{max}. For the three gas mixes: 100/1900, 500/1500, 1500/500
torr of Xe/N_2 respectively, corresponding trends of increasing T_{N_2} measurements are observed. The highest gas temperatures of ~650 K are detected
at the highest Xe partial pressure. These elevated results were detected after
only 5 minutes of SEOP and are greater than 200 K above the T_{cell} value. A
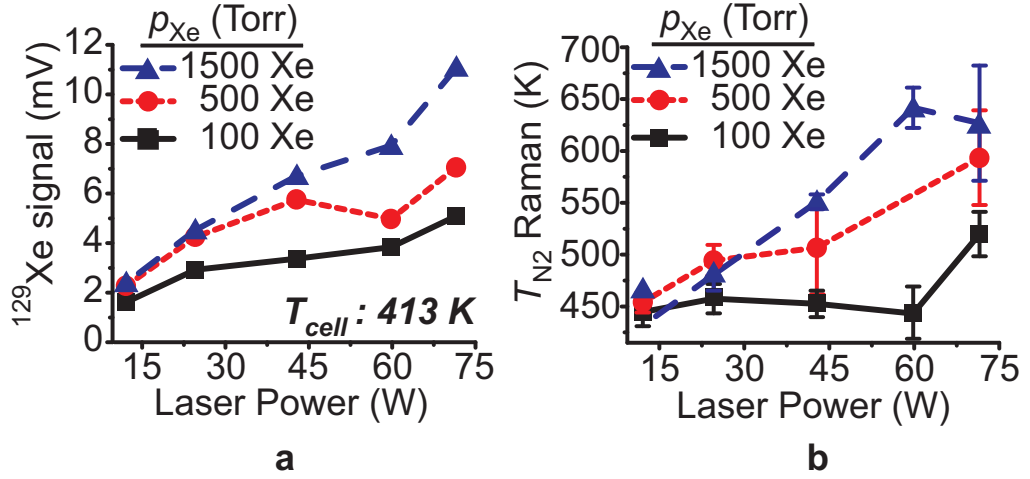
Figure 4.6: Comparison of three Xe/N_2 gas mixtures (total gas pressure 2000 torr). a)
Effect of increasing laser power on ^{129}Xe NMR signal with b) corresponding T_{N_2} values
with the y-axis baseline set to be equal to T_{cell}. Data acquired from the middle of the
cell after 5 minutes of optical pumping with a Rb D_1 laser tuned to 794.77 nm and oven
temperature of 413 K at the back of the cell. Data collected with 90° arrangement. Figure
from [10].
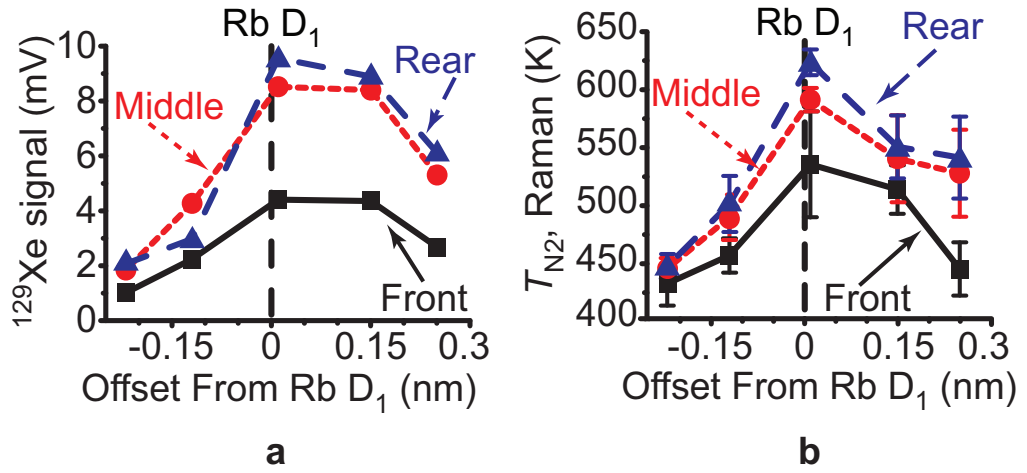
Figure 4.7: LDA tunability is utilised to collect P_{Xe} and T_{N_2} measurements as a function
of pump laser spectral offset away from the Rb D_1 laser line. Data was collected at front
(black), middle (red) and back (blue) positions within the optical pumping cell with a gas
mixture of 1500 torr Xe, 500 torr N_2, and laser power of ~60 W. T_{cell} at the back of
the cell, measured in the oven inlet with a thermocouple, was 403 K. Data collected with
90° arrangement. Figure from [10].

68

simple explanation of this would be from increased laser power and therefore increased absorption. However, with further insight, it can be shown that this effect may arise from the decreased N_2 partial pressure and therefore a greater amount of energy per N_2 gas molecule absorbed. Furthermore, Xe has a lower thermal conductivity than N_2 (Xe: 0.7; N_2: 3.09; x 10^{-2} $Wm^{-1}K^{-1}$), and thus in a high Xe density mix, energy is more slowly dissipated onto the cell walls. Despite high T_{N_2} values at the high Xe partial pressures, which may be expected to be detrimental to ^{129}Xe polarisations and organic wall coatings, the highest NMR signals intensities ($p_{Xe}.P_{Xe}$) were observed with this gas mix.

The centroid laser wavelength was varied around the Rb D_1 transition using the temperature tunability of the LDA to examine the effect of the ^{129}Xe NMR signal and T_{N_2}, with a gas mixture of 1500 torr Xe and 500 torr N_2, Figure 4.7. In addition, the longitudinal position of the 90° Raman arrangement and the NMR coil position was varied to allow measurements to be collected from the front, middle and rear of the OP cell. After only 5 minutes of optical pumping, internal gas temperatures were elevated by $\sim$220 K above T_{cell}. The highest NMR signal (which is proportional to the P_{Xe}) and T_{N_2} were observed at the rear of the OP cell. This could be due to the forced air oven heating the cell from the rear and therefore a T_{cell} gradient is expected, this would subsequently cause a [Rb] gradient and thus increased laser absorption and T_{N_2} at the rear of the cell. Uneven cell heating would likely lead to a non-symmetrical distribution of energy transport and mass flow and thus a change in convection flow patterns, [81]. This may be able to be an advantage though, as uneven cell heating may help to reduce Rb runaway effects, as discussed by Witte *et al.* [88]. The profile shown in Figure 4.7 shows the asymmetric broadening exhibited on the Rb D_1 transition, as described by Romalis *et al.* [80].

In another example of the 90° Raman arrangement, the T_{N_2} and ^{129}Xe NMR
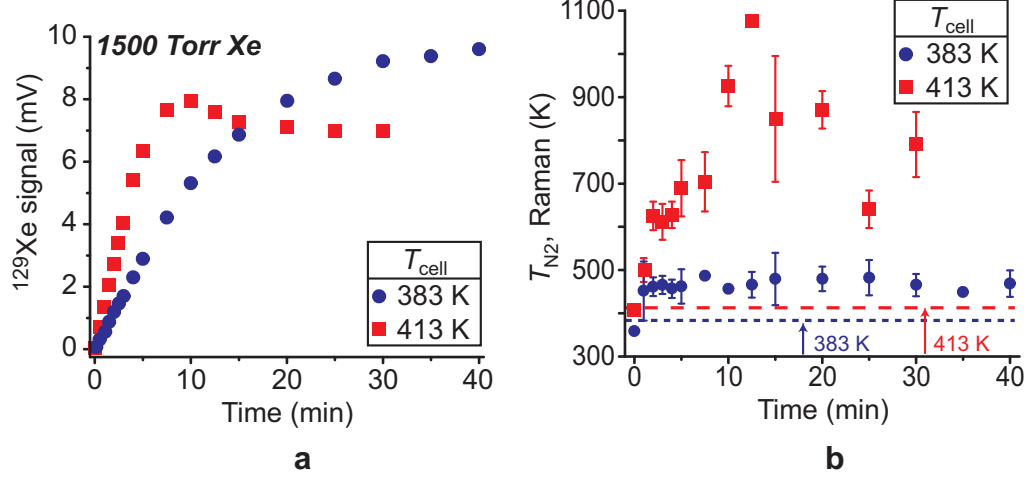
Figure 4.8: a) Low field ^{129}Xe NMR build up curves for two different oven temperatures. b) Simultaneous T_{N_2} data collected using the 90° arrangement. Data collected in the middle of the cell, with ∼60 W pump laser power, 1500 torr Xe, 500 torr N$_2$ gas mixture, 794.77 nm centroid wavelength. T_{cell} is denoted by the dotted (383 K) and dashed (413 K) lines and measured via a thermocouple in the oven inlet at the rear of the cell. Figure from [10].

signals were monitored over a longer time period (30-40 minutes), Figure 4.8, with a gas mixture of 1500 torr Xe and 500 torr N$_2$. Dramatic changes in the P_{Xe} and T_{N_2} were observed with only ΔT_{cell}=30 K where the system changes from steady state (T_{cell}=383 K) to Rb runaway effects (T_{cell}=413 K). Under steady state conditions, the T_{N_2} quickly plateaus and remains at a constant temperature throughout the 40 minute experiment. This corresponds to a steady build up in polarisation and a nearly constant laser absorption profile. Raising T_{cell} to 413 K creates an contrasting performance profile within the SEOP dynamics. Within 15 minutes, temperatures are driven to ∼1000 K, which is elevated almost 600 K above the set T_{cell} value. A steep rise in the NMR profile is observed within the first 10-12 minutes with a fast build up rate. After P_{max} is reached, a drop in ^{129}Xe polarisation is detected with internal gas temperatures simultaneously dropping slightly and then fluctuating over time. This seems to be indicative of Rb runaway, [33, 89, 90], where a high gas temperature leads to an elevated cell wall temperature, where the gas is in contact with the Rb droplet and therefore the Rb number density

increases. Increased turbulence is created within the cell. This effect is seen
more at higher Xe densities gas mixes due to the reduced Xe thermal conduc-
tivity compared to buffer gases and hence its diminished ability to transfer
heat to the cell walls for dissipation.

The examples shown here have shown that internal gas temperatures can be
elevated much above the cell wall temperatures, for example, for a surface
temperature of $\sim$400 K, the internal gas temperatures are raised to around
1000 K. These heightened temperatures are seen most prominently at high
laser powers, long SEOP time periods, on resonance and slight red-shiftening
of the laser centroid wavelength relative to the Rb D_1 absorption transition and
high xenon densities. These effects might not be too dramatic for a continous
flow polariser due to the low average gas residence time within the OP cell
and the typically low xenon partial pressures utilised. Nonetheless, the effects
shown here will be highly relevant to batch mode/stop flow polarisers, due to
long average gas residence times, particularly when high xenon (or other heavy
gas) partial pressures are used.

4.3 180° Optical Raman Arrangement

This work in this section has been published by Newton *et al.* [11]. This inline
module was designed in collaboration with Ondax Inc.

The work described in section 4.2 has provided a useful insight into the en-
ergy transport dynamics and how the internal gas temperatures can help to
provide more understanding into the SEOP process. Despite achieving this
useful information, the signal to noise ratio of the Raman spectra was low and
hence the resulting errors were large on the T_{N_2} values. Sub-mm^3 accuracy is
needed to align the focal points of the excitation and detection modules which
leads to labour-intensive set-up and over time the system is prone to drift.

71
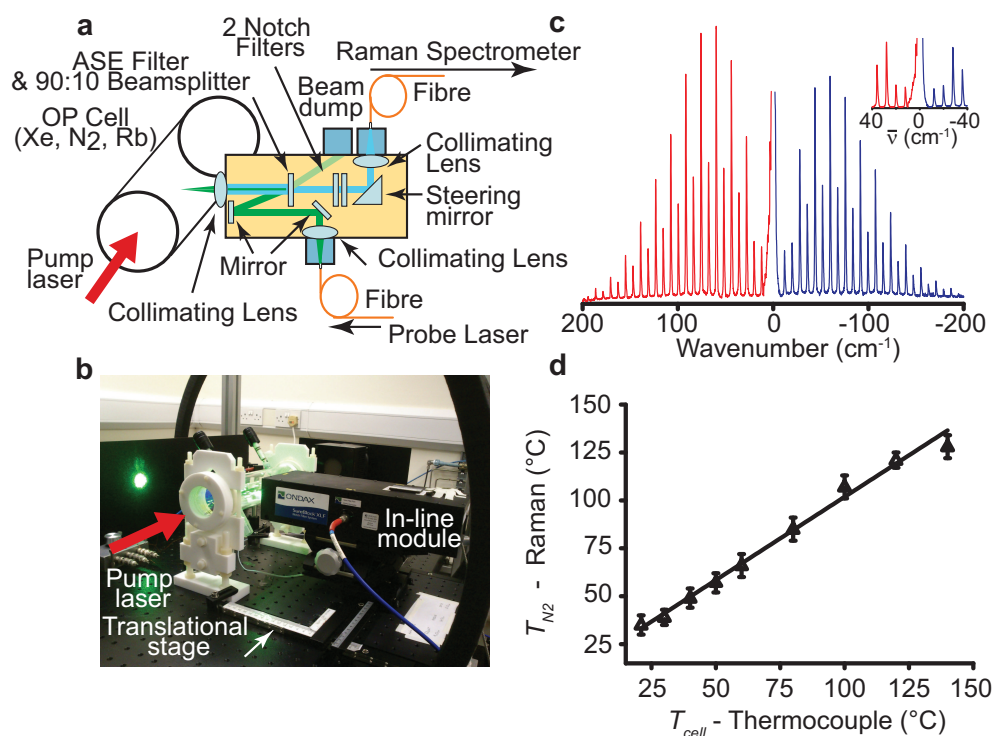
Figure 4.9: a) Schematic of 180° Raman module, with (b) a corresponding photograph. c) A typical background corrected spectrum with Stokes and anti-Stokes peaks shown within a few wavenumbers of the probe laser line. d) Temperature calibration curve of the thermocouple and Raman measurements. This figure is comparable to Figure 4.3 for the 90° Raman arrangement. Reprinted figure from Newton *et al.* [11] with permission from Springer.

The conventional orthogonal arrangement used a combination of intrinsic spatial filtering and the internal baffles of the Raman spectrometer to block the probe laser light and the Rayleigh scattering. A new in-line module has been developed which has a $\sim$23 fold improvement in detection sensitivity leading to faster data acquisition and more accurate real-time monitoring of energy transport.

The 180° method incorporates optical filters to suppress the probe laser light and allow the weak Raman lines only a few wavenumbers away from the probe laser to be resolved. As shown in Figure 4.9(a), the Raman excitation and detection occur along the same optical path, as such once the module has been aligned, it does not require any future adjustment. Two Ondax Sure-Block ultra narrow-band notch filters are included in the module. The angular tunability of the notch filters greatly attenuates background scattered light, allowing ultra-low frequency Raman spectroscopy to be performed, Figure 4.9(c). Moser and Havermeyer [91] showed that combining several reflective volume holographic gratings together with different slant angles could lead to a filter with an optical density of 4 and a transition width of $\sim$10 cm^{-1}. In addition, there is one Ondax NoiseBlock ASE filter (Amplified Spontaneous Emission). This serves two purposes, firstly, on the pathway towards the cell (shown in green, Figure 4.9(a)) it will transmit to the beam dump: laser sidebands, spontaneous emission from laser diodes and fibre-induced fluorescence resulting in a single frequency source being reflected and focused into the cell. On return from the cell (shown in blue), it acts as a spectrally sensitive 90:10 beam-splitter to transmit Raman scattering and reflect Rayleigh light. The device with its translational stages are shown *in situ* within the SEOP apparatus in Figure 4.9(b). The focal length of the module can be varied by the choice of entry/exit collimating lens, in our device the focal length is 50 mm on an A coated plano convex lens (Thorlabs LA1131-A).
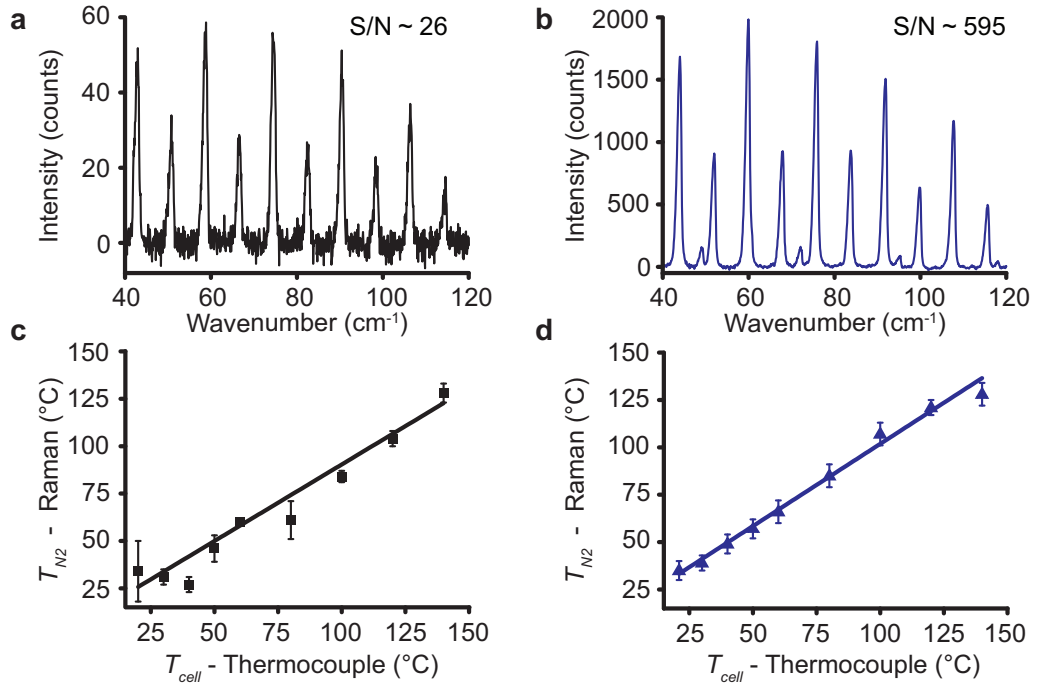
Figure 4.10: Comparison of 90° and 180° excitation and collection methods. a) A typical spectrum produced from the 90° arrangement, b) under the same acquisition times (15 s), cell temperature (24°C) and gas loading (100 torr Xe, 1900 torr N_2) a ~23 fold improvement in SNR is shown in a typical spectrum acquired from the 180° setup. Corresponding temperature calibration curves for the 90 and 180° methods are shown in c) and d) respectively. Oxygen peaks appear from the 180°setup from contributions along the optical pathway, as discussed in section 3.5.4.3 this contribution can be removed by background correction. Reprinted figure from Newton *et al.* [11] with permission from Springer.

A comparison of the 90° and the 180° Raman arrangements is shown in Figure 4.10. Example spectra are plotted for identical cell conditions of 100 torr Xe, 1900 torr N_2 with a 15 s acquisition time at 24°C, under conditions of no SEOP. The spectra show a ~23 fold improvement in SNR between the 90°, Figure 4.10(a), and 180° methods, Figure 4.10(b). This results in more precise temperatures measurements as shown in the temperature calibration plots, Figures 4.10(c) and (d). In Figure 4.10(b), O_2 peaks can be seen manifested in the spectra in addition to the N_2 peaks. These arise from Raman scattering that occurs along the line of the optical path and can be removed by an evacuated cell spectra, as described in section 3.5.4.3. At our excitation

wavelength the molar scattering intensity is ∼1.5-2 times greater for O_2 than
N_2 [92], but these peaks are fully removed in our background correction.

4.3.1   Experiments   performed   using 180° Raman arrangement

Demonstration of 'real-time' (3 s) *in situ* measurements of internal gas tem-
peratures with a gas mix of 100 torr Xe, 1900 torr N_2 show pump laser induced
cell heating in Figure 4.11(a). The 180° module is able to be spatially trans-
lated and thus measurements were acquired perpendicular to the main pump
laser beam transversely across the front of the cell, Figure 4.11(b). Data was
acquired after 5 minutes of SEOP whilst using either a broadband laser (QPC
Brightlase Ultra 100 with a FWHM=2.13 nm, Figure 4.11(c)) or a frequency
narrowed laser (QPC Brightlock Ultra 100 with a FWHM=0.26 nm, Figure
4.11(d)). Temperature elevations of ∼40°C above T_{cell} were observed with the
broadband pump laser beam, whereas with the frequency-narrowed laser tem-
peratures were in excess of 200°C above T_{cell}. This effect is likely due to the
increase in resonant photon energy and will be dependent on gas mixture and
SEOP pump up time.

Figure 4.12 illustrates the effect of illuminated laser power on ΔT_{N_2} (T_{N_2}-T_{cell})
for various T_{cell} values. A linear trend is shown with ΔT_{N_2} being observed for
increasing laser powers for increasing T_{cell}. The highest T_{N_2} is measured at the
highest P_{Xe} and T_{cell}. Increased T_{cell} will likely give rise to increased Rb num-
ber density and therefore a greater number of absorbers in the gas phase to
absorb the pump laser light leading to more energy deposition into the N_2 gas.
Low T_{cell} gives a relatively stable T_{N_2} across the incident laser powers.
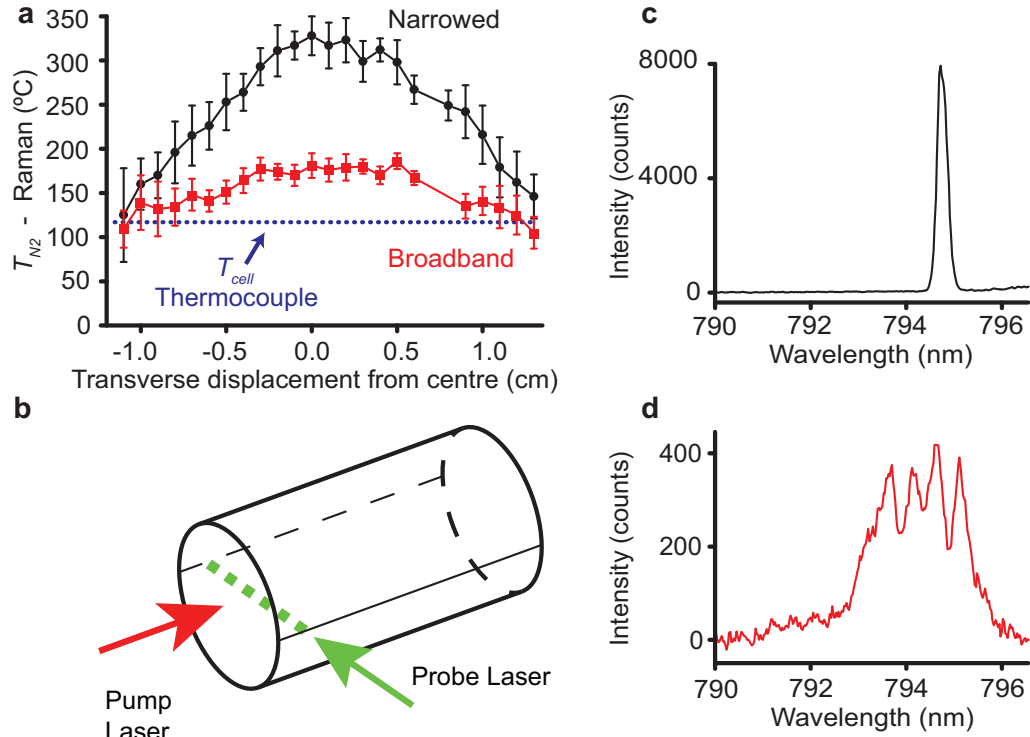
Figure 4.11: (a) Two Rb D_1 pump laser excitation methods were compared to observe the effect on T_{N_2} with spatial position across the cell perpendicular to the pump laser beam (b). These steady state T_{N_2} values were acquired (3 second acquisition time) after 5 minutes of illumination by a broadband (c - 60 W, FWHM=2.13 nm) and a frequency-narrowed laser (d - 60 W, FWHM=0.26 nm). Data collected with 180° arrangement, T_{cell} was 150° at the back, 110° at the front of the cell, T_{N_2} were acquired at the front of the cell (21 mm behind the front window). (Lines are meant to guide the eye). Reprinted figure from Newton *et al.* [11] with permission from Springer.
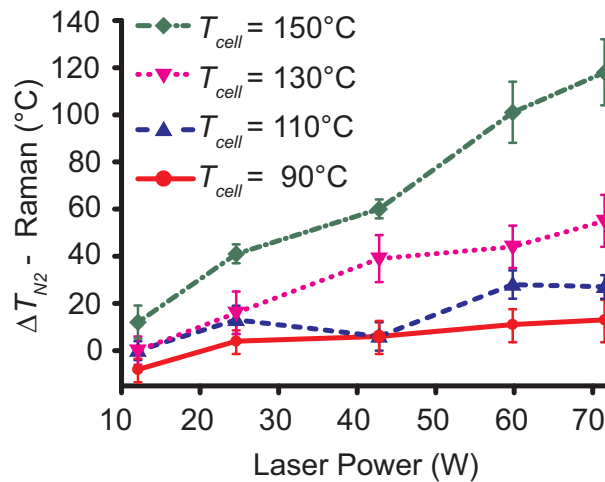
Figure 4.12: Relative changes in T_{N_2} versus T_{cell} measured in the middle of the OP cell at various laser powers after 2 min of SEOP. Data collected with 180° arrangement. Reprinted figure from Newton *et al.* [11] with permission from Springer.

4.4   Summary

Raman spectroscopy can be used to measure internal gas temperatures *in situ* during the spin exchange optical pumping process. A $\sim$23 fold improvement in detection sensitivity has been shown with the 180° arrangement utilising optical filters as opposed to the 90° setup which encompasses spatial filtering and the internal baffles of the spectrometer to manually block out the probe laser and Rayleigh scattering. The increased SNR when using the in-line module results in improved accuracy and precision in T_{N_2} and enhanced ease of use for spatial measurements. This module will be used for further Raman temperatures in future chapters of this thesis.

Chapter 5

Thermal management in the spin exchange optical pumping process

5.1 Introduction

Spin exchange optical pumping systems are very sensitive to many experimental parameters, in particular the oven temperature dramatically changes the maximum possible ^{129}Xe polarisation (P_{Xe}) and the spin exchange times. Although it was demonstrated by Walter *et al.* [51] that the cell surface temperatures (T_{cell}) are not a good indication of the internal cell temperatures, due to limitations of budget and equipment, many research groups use surface thermocouples to get an indication of optical cell and oven temperatures or to return to a particular set of conditions.

A dependence of transmitted pump laser spectra with T_{cell} was shown by Zook *et al.* [90]. Relative Rb densities can be inferred by these transmission spectra. Low temperatures were shown to have too little absorption and higher T_{cell} suggested greater Rb number density, [Rb], thus light could be blocked

from reaching the back of the cell. For sufficient illumination across the length
of the cell, an optimal oven temperature needs to be found. Simulations by
Fink et $al.$ [81] noted that the external temperature governs the [Rb] and
convection patterns. P_{Xe} was shown to increase with increasing T_{cell} and laser
power until a maximum polarisation was reached and then the polarisation
dropped off exponentially as these two variables continue to increase. This led
to some early suggestions that SEOP experiments should not be performed
at high laser powers to mitigate uneven heating distributions [89]. Deviations
seen by Fink et $al.$ [81] and Six et $al.$ [82] between simulated and experimen-
tal values of P_{Xe} are thought to be due to external cell temperatures being
used to calculate the spin-exchange terms and thus the [Rb] will vary between
the actual and calculated values. As well as T_{cell} altering the amount of [Rb],
over time the vapour pressure of rubidium will decrease due to contaminants
creating rubidium oxides on the surface of the rubidium droplet and thus ex-
periments need to be run at hotter temperatures to generate the same Rb
vapour density [81]. Numerical simulations of P_{Xe} across a polarisation cell
showed that low temperatures where the laser light penetrates the whole cell
leads to transverse convection rolls. However, high cell temperatures create
longitudinal convection patterns from uneven temperature distributions and
thus decreased P_{Xe} arising from a greater amount of spin destructive wall col-
lisions [81].

The interdependence between T_{cell} with P_{Xe} was further investigated by Whit-
ing et $al.$ [33] with the Xe polarisation dynamics being examined with various
xenon partial pressures. It was shown that optimal cell temperatures (T_{OPT},
the temperature at which steady state P_{Xe} is maximised) varied such that
T_{OPT} was higher for lower xenon partial pressures (e.g. 110°C for 50 torr Xe,
compared to 80°C for 1400 torr Xe, in 2000 torr total cell pressure). This
inverse relationship between partial pressure and T_{OPT} was attributed to the

xenon as when similar experiments were performed with constant xenon partial pressure and varying nitrogen partial pressure, there was little variation in T_{OPT}. As the accumulation rate of P_{Xe} increases with T_{cell} causing the [Rb] to increase, it can be seen from equation 2.10 that the spin-exchange rate, γ_{SE} will increase. High T_{cell} causes [Rb] to increase to a detrimental level, absorbing a high percentage of pump laser light and thus poor illumination of the middle and back of the cell is observed. This leads to a decrease in P_{Rb} which directly results in lowered P_{Xe}. This instability within the SEOP cell is known as rubidium runaway [33, 89, 90]. The process of rubidium runaway is initiated by increased light absorption which creates heat due to energy pooling into the nitrogen [50]. This increase in internal temperature creates more Rb vapour which raises the opacity through the cell resulting in the majority of the light being absorbed at the front of the cell. As the cell becomes more opaque, the rubidium polarisation decreases resulting in more available absorbers which absorb more of the pump laser light thus creating a self-reinforcing feedback loop.

Rubidium runaway has a severely adverse effect on the P_{Xe} as this dramatically drops, therefore it becomes crucial to monitor and prevent this harmful process for taking place. Currently, there are three main practices to impede this effect. Firstly, implementation of a pre-saturation column where rubidium can be heated to a particular temperature in the absence of any lasers before entering the OP vessel [55]. Rubidium runaway can not take place as the source of rubidium is outside the SEOP region. This method will only work in a continuous flow polariser as the gas is required to flow through the pre-saturation column then in the laser absorption region. In addition this creates a bulky system as multiple glassware regions are required.

A second approach is to control the thermal management of the global pump cell vessel by obtaining a full parameter space of different T_{cell} values and

avoiding the regions of this space where rubidium runaway is known to take place [33, 59]. Nikolaou *et al.* [59] have demonstrated this thermal mapping, with a feedback loop to control the Rb concentration in the gas phase by a thermistor on the optical pumping external cell surface. As previously shown by Whiting *et al.* [33], an inverse relationship between [Xe] and T_{OPT} was observed, a suggested explanation is that the Rb spin destruction by Xe becomes more dominant at high [Xe]. This can be reduced by lowering the operating temperature and thus maintaining a sufficient 'photon-to-Rb' ratio with a high volume averaged Rb polarisation, $<P_{Rb}>$, and maximum P_{Xe}. Spin exchange rates were noted to not be constant with the external cell temperature at different partial pressures. Therefore it was proposed that higher internal cell temperatures might be seen for high Xe densities resulting in higher than expected Rb vapour densities, this was explored with Raman spectroscopy in Figure 4.6. Nikolaou *et al.* [93] performed further studies and found a ramped temperature method might present the optimal SEOP conditions. In this procedure initially the cell is heated to an optimal SE rate and then cooled to a region of optimal P_{Xe}, thus utilising multiple temperatures to create a high polarisation in a short period of time whilst avoiding rubidium runaway.

Witte *et al.* [88] presented a third technique to alleviate rubidium runaway effects in a continuous flow polariser, whereby regional cell temperatures are monitored and altered. Surface thermocouples were attached to the surface of an optical pumping vessel at the front, middle, and back, Figure 5.1, and although they did not have the capabilities to monitor internal gas temperatures, they utilised the thermocouples along with transmitted laser spectra into a feedback loop to know when rubidium runaway was starting. Using this method, they were able to observe temperature gradients across the cell of greater than 80°C during rubidium runaway with the hottest temperatures at the front. This team were able to cool the front of the cell by several tens of
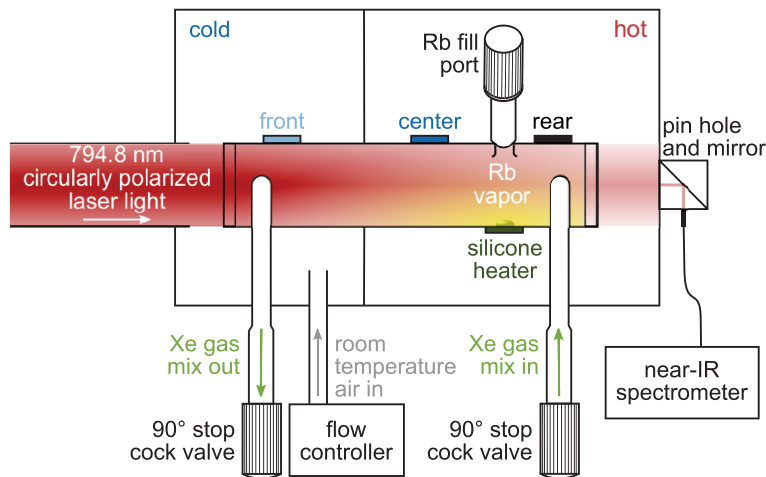
Figure 5.1: Schematic showing a technique of temperature control utilising surface thermocouples at the front, middle and rear of cell in a continuous flow polariser. Reprinted figure with permission from ref [88], copyright 2014, AIP Publishing LLC.

degrees, to dissipate the heat and create a stable temperature gradient. This resulted in a 2-3 fold enhancement in P_{Xe} compared to the more conventional global heating method.

In order to hinder this rubidium runaway mechanism and to aid future experiments with increased xenon polarisations we need to understand it further. Within this chapter, temperature dependent SEOP experiments were conducted whilst monitoring P_{Xe}, T_{N_2} and transmitted laser spectra, are shown in Figures 5.2 and 5.3.

5.2 Experimental investigations of thermal management and rubidium runaway

The response of T_{cell} to a spin exchange optical pumping system is shown in Figure 5.2. At low SEOP temperatures (under these conditions, 90°C), the polarisation builds slowly due to low power absorption. This is reflected in the internal gas temperatures, measured via Raman spectroscopy, see Chapter 3 and 4 for methods. Under conditions of slow ^{129}Xe polarisation build up,

(a)

(b)

(c)
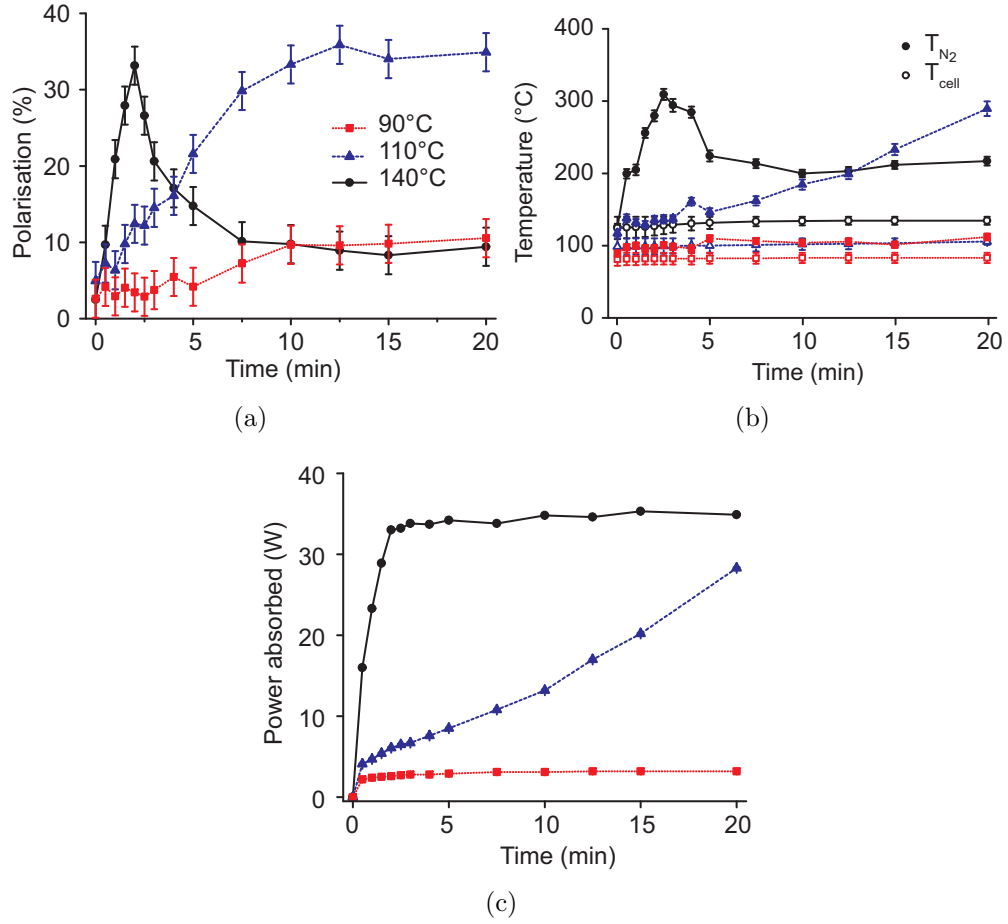
Figure 5.2: Temperature variation of (a) polarisation, (b) internal gas temperatures and (c) power absorbed as a function of time and oven temperature. $T_{cell} = 90$, 110, $140°$C denoted by red squares and dotted lines, blue triangles and dashed lines, and black circles and solid lines respectively. T_{cell} and T_{N_2} are distinguished by open and closed symbols in (b). Gas mix: 100 torr Xe, 1100 torr N_2, 800 torr He; 60 W frequency narrowed laser power; obtained from the middle of the cell.

T_{N_2} is slightly elevated above T_{cell} by about 20°C, this temperature elevation
is stable and maintained at a constant value throughout the experiment. This
is indicative of a steady state experiment. At a slightly higher temperature
of 110°C, the pump laser power is absorbed at a steadily increasing rate over
time, resulting in more energy being dumped into the nitrogen. This arises
from laser light being absorbed by the excited state Rb which is quenched by
N_2 (50:50 ratio of depletion to m $= \pm 1/2$ states, see Grotrian diagram, Figure
2.2) and thus the Rb relaxes to its ground state. The majority of the optical
energy absorbed by the Rb is transferred to the nitrogen (95-99%) [51], this
is converted to heat energy which raises the temperature of the gas. Elevated
temperatures increase the rubidium vapour density and thus more power is
absorbed as there are more available unpolarised rubidium electrons which are
subsequently quenched by nitrogen creating a feedback loop which occurs with
a rapidly increasing temperature. In this particular case (110°C), conditions
are on the edge of steady state as the ^{129}Xe polarisation plateaus but we are
approaching a rubidium runaway scenario, as seen by increasing power absorp-
tion and rising temperatures of 185°C above the set oven temperature.

Rubidium runaway describes the non-ideal case where the xenon polarisa-
tion is seen to quickly increase and then dramatically decrease, hence the
word runaway, as seen in the 140°C conditions in Figure 5.2. In the initial
stage of Rb runaway, SEOP appears to occurs as normal with the increasing
^{129}Xe polarisation, however, this is often very rapid with dramatically elevated
temperatures (T_{N_2}-$T_{cell}\sim$200°C) and a high percentage of pump laser light be-
ing absorbed. After maximum polarisation is reached, a rapid deterioration
in polarisation is observed, with a corresponding drop in the gas temperature,
whilst the power absorbed reaches a plateau. It is thought that the unpo-
larised Rb density is large at the front and therefore optically opaque due to
a high rate of nitrogen quenching (returning excited Rb to its ground state)

resulting in high temperatures. This occurs predominantly at the front of the
cell as the light initially enters here, subsequently if most of the laser light
is absorbed at the front, it will not be able to travel through to the back of
the cell, thus power absorbed plateaus at a maximum. After maximum power
absorption is reached, the middle of the cell has limited photons available for
absorption (due to high absorption at the front of the cell) and hence there
are few polarised rubidium electrons to be quenched by the nitrogen, leading
to a drop in T_{N_2} (T_{N_2}-T_{cell}=100°C) and thus a drop in Xe polarisation. It
can be seen how the final P_{Xe} is much reduced compared to the polarisation
obtained from a 110°C experiment. Rubidium runaway has been used as an
advantageous effect in the work by Nikolaou *et al.* [93], where high P_{Xe} can
be quickly achieved (for example with T_{cell}=140°C in Figure 5.2(a)) then the
cell temperature is actively reduced (e.g. to 110°C in Figure 5.2(a)), so that
high xenon polarisations are rapidly produced using active feedback to control
cell temperatures.

In order to examine spatial effects of the steady state (120°C, under condi-
tions in Figure 5.3) and rubidium runaway processes (130°C), three NMR
coils were used to correspond to three spatial probe Raman positions along
the longitudinal length of the cell, Figure 5.3(a). Global power absorption was
examined using a HR4000 Ocean Optics Spectrometer, Figure 5.3(b). A cold
cell measurement at 25°C, in the absence of optical pumping, was acquired for
comparison to the SEOP measurements at 120°C and 130°C. In Figure 5.3(b)
spectra are shown after 30 minutes of SEOP with 57% and 90% absorption at
120°C and 130°C respectively, with the dip from the Rb D_1 transition observed
at 794.77 nm.

Under steady state conditions, with the optical pumping cell heated from the
rear, the highest in cell temperatures are observed at the back, Figure 5.3(d),
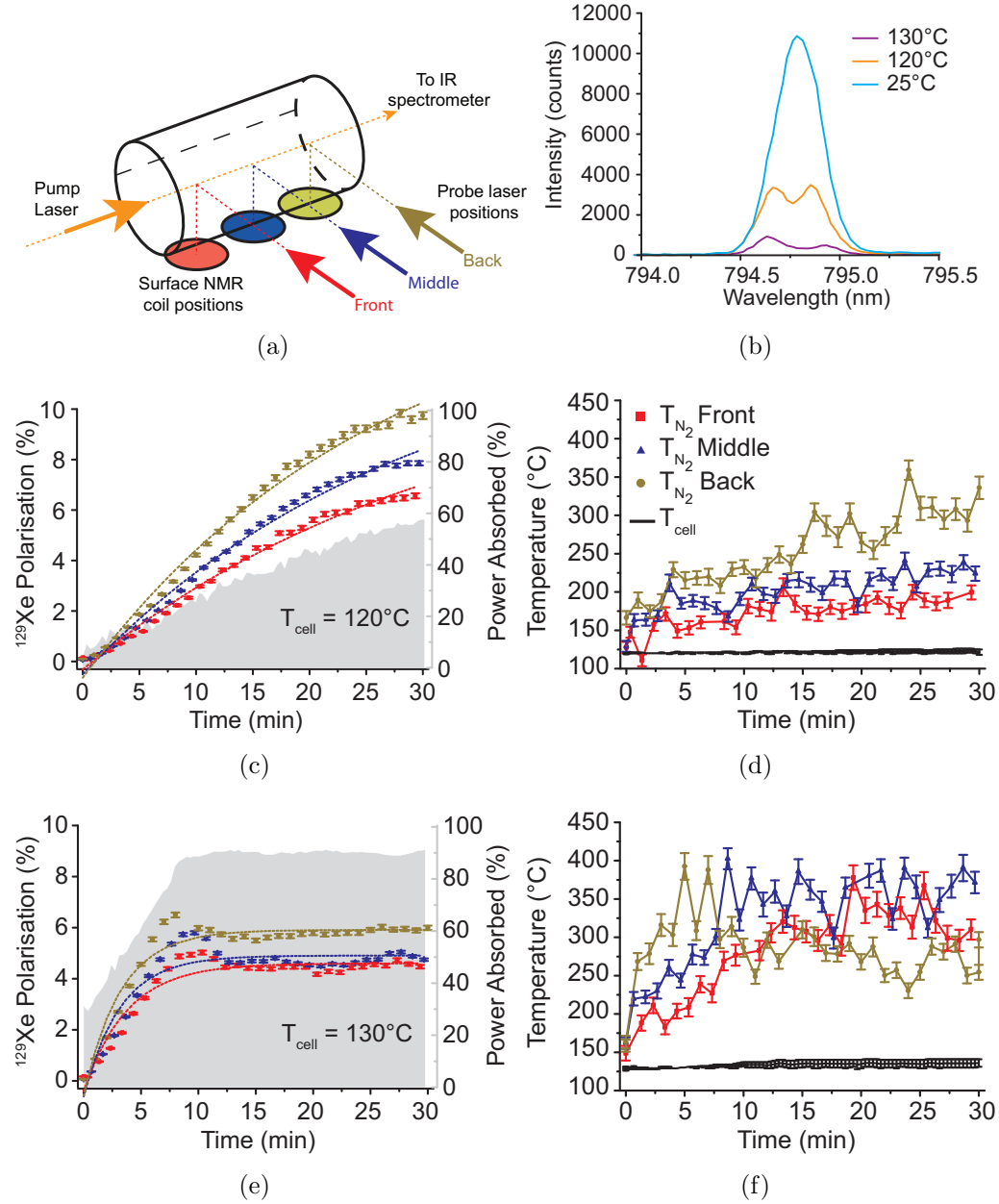
Figure 5.3: Characterising polarisation and internal gas temperatures in steady state and rubidium runaway conditions. (a) Schematic of spatial probing of low field ^{129}Xe NMR and Raman spectroscopy along the longitudinal length of the OP cell. Colours denote the spatial positions of front (red), middle (blue) and back (green). (b) Transmitted pump laser spectra for a cold cell (cyan), T_{cell}=120°C (orange) and T_{cell}=130°C (purple). (c) and (d) represent ^{129}Xe and T_{N_2} build up curves at 120°C under steady state conditions, (e) and (f) are at 130°C showing rubidium runaway. The grey area in (c) and (e) signifies the percentage power absorbed within the optical pumping cell relative to a room temperature cell. Black error bars in (d) and (f) show the spread of oven temperatures (T_{cell}) recorded by a thermocouple placed in the oven inlet (back) and outlet (front). A large deviation is seen between T_{cell} and T_{N_2} in both experimental conditions.

suggesting that there is a higher rubidium number density in that position. Given a higher rubidium number density, it is possible that there is an increased rubidium polarisation, P_{Rb}, resulting in an increased P_{Xe} at the rear of the cell, Figure 5.3(c). After 30 minutes of SEOP, an approximately 40% spread in the values of P_{Xe} is observed across the length of the cell from 6-10% in this high Xe density mix (1500 torr Xe, 500 torr N_2), with a corresponding temperature difference of T_{cell}=122°C, T_{N_2}(front)=199°C, T_{N_2}(middle)=223°C, and T_{N_2}(back)=335°C. Along the length of the cell, the resultant temperature gradient is 136°C, and a $\sim$175% temperature elevation between T_{cell} and the back internal gas temperature is observed with a numerical value of 213°C. This temperature elevation and gradient is a contributing factor as to why the simulations and SEOP experiments do not agree.

When the conditions of rubidium runaway are examined with a spatial focus, very different dynamics are observed relative to steady state. Although all three positions initially, at time $t = 0$, exhibit the same temperature, the back rapidly increases in temperature to almost 400°C (T_{cell}=120°C). After 8 minutes of SEOP, a maximum ^{129}Xe polarisation is seen and this plummets as more absorption is seen in the front and middle of the cell which is observed as increasing temperatures in these positions. A positional crossover in maximum temperature is seen at the point of Rb runaway (when maximum P_{Xe} is reached and absorption reaches a plateau at almost 100% absorption). After further SEOP, the front and middle positions become fairly homogeneous with similar P_{Xe} and T_{N_2}, but the back is very different with elevated P_{Xe} and lower T_{N_2}.

5.3   Conclusions

It is seen that the global temperature of the gas approximately follows the global xenon polarisation (Figure 5.2). This is validated by the knowledge that

the nitrogen quenching the excited rubidium states produces heat in the nitrogen and non-radiative relaxation to the rubidium ground state. This allows a build up of spins in a single state creating a rubidium polarised state which can spin exchange with xenon. However, when the spatial variants are examined, it is seen that this is a highly sensitive system with position dependent conditions. When typical optical pumping conditions are used a steady state xenon polarisation is obtained and a constant temperature elevation above the surface thermocouple is observed, with temperatures greatest at the back of the cell. However, when rubidium runaway takes place, a rapid rise and then fall in P_{Xe} is detected, which changes the internal gas temperatures with the back temperature plummeting as the laser light is absorbed at the front of the cell. Although convection has been shown to take place during optical pumping [51, 81], these results suggest that minimal mixing occurs across the cell. Temperatures at the front of the cell were $\sim$110°C hotter than the back, and elevated by $\sim$240°C relative to the surface thermocouples. This validates the discussion that a high percentage of pump laser light is prevented from reaching the back of the OP cell due to a high [Rb] at the front of the cell resulting from high internal cell temperatures. In the future, if these Raman experiments to spatially measure internal gas temperatures could be combined with a localised alkali metal number density measurements, such as that shown by Appelt *et al.* [89], then further advances could be made to link together SEOP theory and experiments.

Chapter 6

Alkali metal choice for SEOP

6.1 Investigations of rubidium vs. caesium

6.1.1 Introduction

Rubidium has long been the alkali metal of choice for hyperpolarised gas preparation during the SEOP process. This is primarily due to its large spin exchange cross section, relatively high vapour pressure and the availability of high power lasers at the D_1 wavelength [28]. With the advent of caesium lasers at the D-line wavelengths it became possible for SEOP to be considered using Cs as the alkali metal for the optical pumping process, as investigated by Whiting *et al.* [28]. Cs is a good prospect for SEOP due to the 1.5 - 2 times greater binary spin exchange cross section for Cs-^{129}Xe when compared to Rb-^{129}Xe, [5, 28, 39, 44–46]. In addition, Cs has lower energy absorption lines leading to more photons per Watt of light, a lower spin destruction rate and a higher vapour pressure, Figure 2.5, [30, 31].

The advantages of the lower melting point and higher vapour pressure of Cs enable SEOP to be performed at lower temperatures. There are many technical reasons why this may be preferable, for example in section 3.2.1 an organic
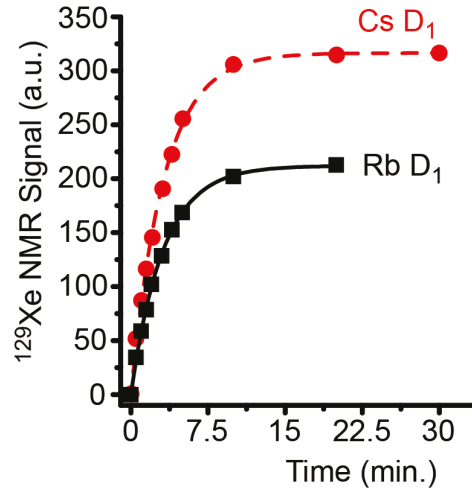
Figure 6.1: Comparison of P_{Xe} buildup curves (collected at $\sim$32 G) for Rb and Cs alkali metal laser pumping on the D_1 transition. Each run was carried out using 2000 torr Xe, 600 torr N_2 with the optimal T_{cell} and laser power for each set of runs being 70 $^{\circ}$C & $\sim$46 W for Cs D_1, and 80 C & $\sim$53 W for Rb D_1 excitation. Reprinted figure from ref [28], with permission from American Physical Society.
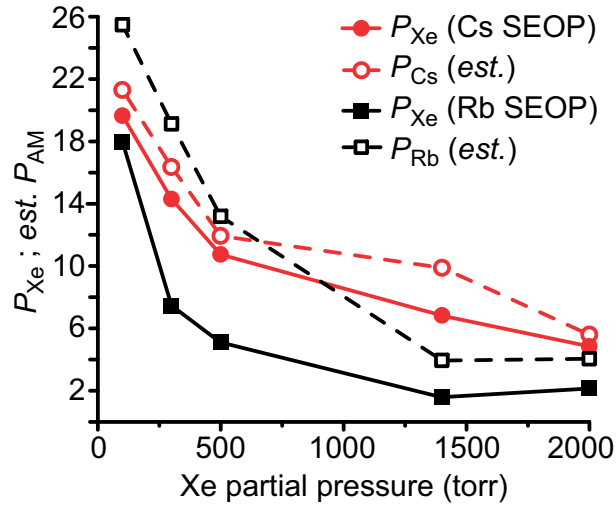
Figure 6.2: Xe polarisation, P_{Xe}, (measured at 9.4 T) as a function of Xe partial pressure for Cs (red-solid) and Rb (black-solid) SEOP, with corresponding estimated alkali-metal electron spin polarization (P_{AM}) values for Cs (red-dashed) and Rb (black-dashed). Laser powers are 48 W for Cs and 52 W for Rb. Reprinted figure from ref [28], with permission from American Physical Society.

cell wall coating (SurfaSil) was discussed to reduce ^{129}Xe relaxation via wall collisions, at high temperatures this surface coating deteriorates. At lower cell temperatures, thermal stability is expected to be easier to control. Finally, lower cell temperatures would enable faster heat up and cool down cycles required for production of HP ^{129}Xe in batch mode polarisers.

Previous studies by Whiting *et al.* [28], found that the spin-exchange rate for Cs-^{129}Xe is about 1.5 times greater than Rb-^{129}Xe under optimal conditions when pumping on the D_1 transition, Figure 6.1. The advantage seen for Cs SEOP is especially pronounced at high Xe densities, Figure 6.2, making it potentially viable for clinical use particularly with a batch-mode polariser, [8]. This work utilised two 40 W broadband LDAs tuned to Cs D_1 ($\sim$894.3 nm) and D_2 ($\sim$852.1 nm) and a comparable Rb D_1 laser ($\sim$794.8 nm) with a linewidth of 1.9-2.9 nm. This allowed the direct comparison of D_1 and D_2 for Cs-^{129}Xe SEOP under similar experimental conditions.

The work in this chapter explores Cs-^{129}Xe SEOP under a higher powered ($\sim$60 W), frequency-narrowed LDA ($\sim$0.35 nm). Utilising this new laser technology, we were able to compare frequency-narrowed and broadband lasers for ^{129}Xe production using Cs. We examine whether similar improvements can be realised to the three fold improvement in P_{Xe} attained with Rb-^{129}Xe frequency narrowed light sources compared to broadband lasers [70]. In addition Cs-^{129}Xe and Rb-^{129}Xe can be directly compared using narrowed lasers. We aim to gain a further understanding of Cs-^{129}Xe spin exchange dynamics.
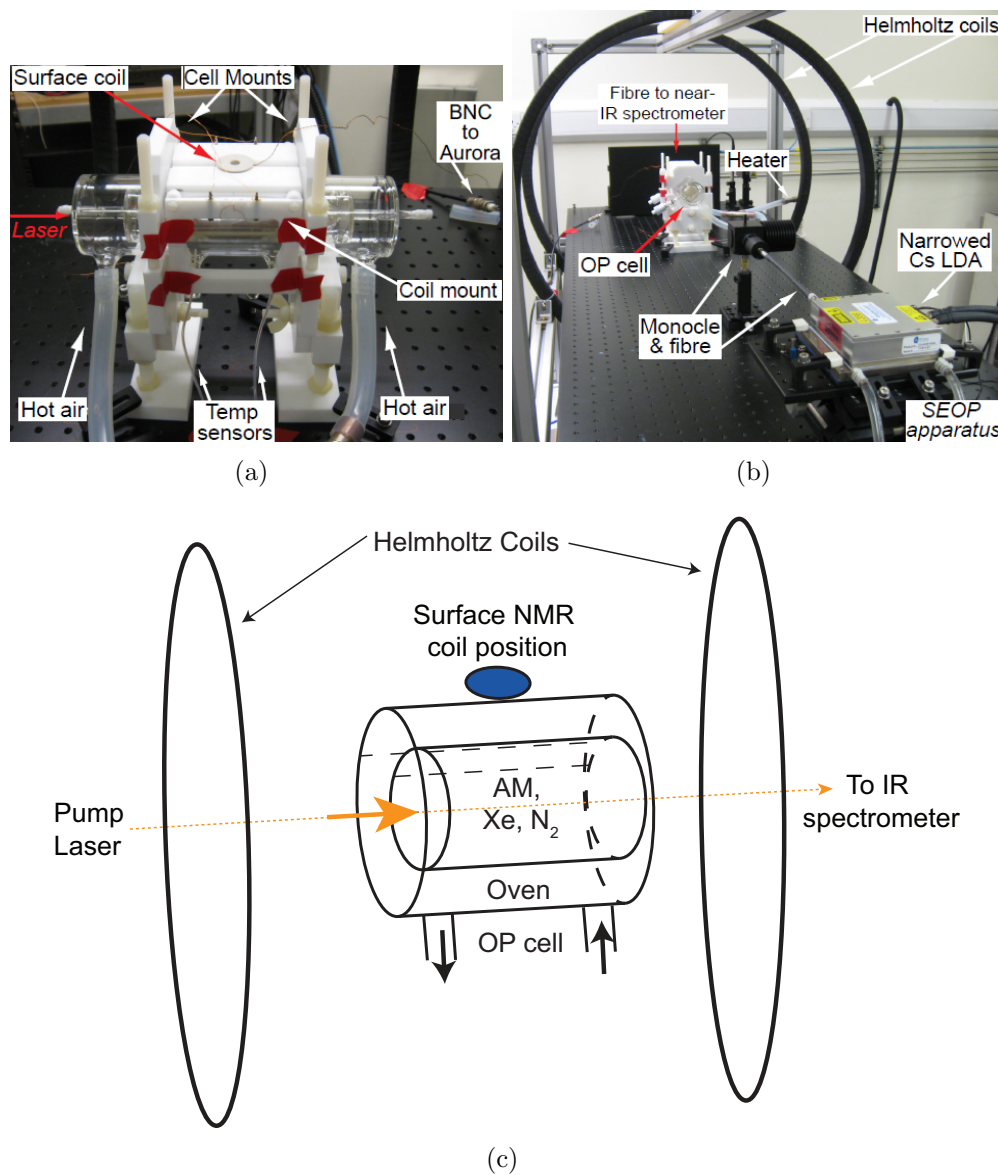
Figure 6.3: (a) Cs cell shown *in situ* with custom designed PTFE cell mounts and surface coil mount, (b) photo and (c) schematic of SEOP apparatus shown for Cs experiments.
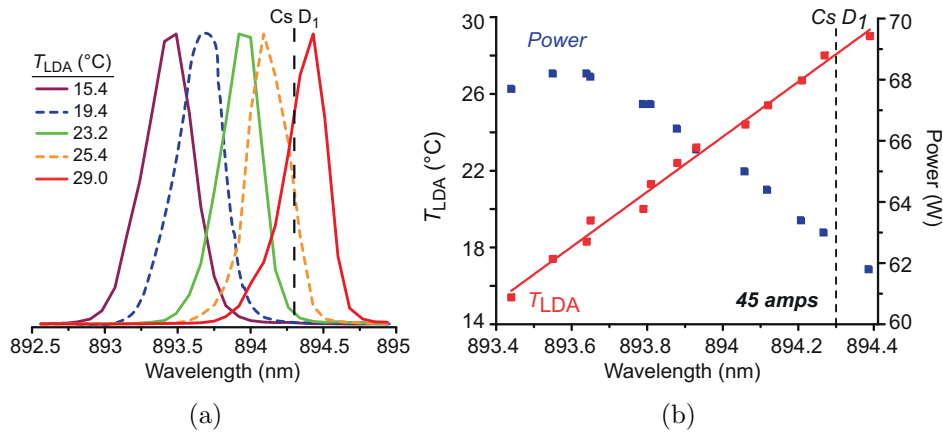
Figure 6.4: a) Example normalised transmitted laser profiles for frequency narrowed Cs pump laser. Laser wavelength can be tuned by varying the LDA temperature, T_{LDA}, controlled by a water chiller. Typical linewidth is $\sim$0.35 nm, spectral resolution is limited by the ability of the IR spectrometer. b) Red curve denotes the tuning for T_{LDA} with emitted laser wavelength. Corresponding change in laser power (blue) is shown with a constant 45 A driving current. Power loss is about 6 W over the range, this is less than a 10 % loss in total laser power.

6.1.2   Methods

The laser SEOP apparatus was set-up as outlined in Chapter 3, with the long fibre ($\sim$30 cm) shown in Figures 3.7(b) and 6.3(b). A Rosen style cell [63] ($\sim$3.8 cm diameter, $\sim$16.5 cm length) was held in place with custom designed PTFE mounts, Figure 6.3(a). The mounts are adjustable to facilitate cell alignment with the laser and magnetic field, in addition they are able to hold various sized OP cells. A small surface coil of $\sim$2.5 cm diameter was held in place outside of the Rosen cell and was used for pulse and acquire experiments with a Magritek Aurora spectrometer, Figure 6.3(c).

The Cs laser ($\sim$60 W, $\sim$0.35 nm FWHM) is able to be spectrally tuned via the 'on-chip' volume holographic gratings. Altering the temperature of the LDA, T_{LDA}, changes the spacing between the internal gratings and the tuning of the wavelength is reflected back into the diodes forcing the emission of a particular wavelength. An example of this spectral tuning can be seen in Figure 6.4(a). The effect of varying the laser wavelength and power is shown in Figure 6.4(b). Increasing the T_{LDA} red-shifts the spectral output by $\sim$0.07 nm/°C, whilst laser power decreases at 0.60 W/°C. In addition to this frequency-narrowed laser, comparative studies utilised a broadband Cs D_1 laser ($\sim$50 W, $\sim$3.8 nm FWHM) and a frequency-narrowed Rb D_1 laser ($\sim$80 W, $\sim$0.30 nm FWHM). Unfortunately, neither frequency narrowed laser had the capability to tune into the 'red' side of the respective absorption lines, preventing the in-depth study of changes to the alkali metal absorption profile at high xenon densities.

6.1.3   Results and discussion

The effect of T_{OPT} on xenon partial pressure, p_{Xe}, for Cs optical pumping on the D_1 transition is demonstrated in Figure 6.5(a). Higher p_{Xe} are shown to have a preference for lower T_{cell}. A stronger dependence of T_{cell} and p_{Xe} was seen previously for Rb-^{129}Xe SEOP by Whiting *et al.* [33], but this difference could be due to lower laser flux for the Cs-^{129}Xe SEOP under current experimental conditions. Sample ^{129}Xe polarisation build up curves are shown for 1750 torr Xe and 250 torr N_2 at various temperatures, Figure 6.5(b). Increased buildup times and ^{129}Xe NMR signal were achieved at low T_{cell} values. High T_{cell} values correlate to thermal runaway conditions being experienced and thus the ^{129}Xe signal is drastically reduced due to increased laser absorption.

Optimal T_{cell} is explored for the different alkali metal D_1 transitions in Figure 6.6. The optimal temperature for SEOP is lowered when traversing from Rb D_1 narrowed to Cs D_1 broadband to the Cs D_1 narrowed source. Observations of up to 3-fold improvement in ^{129}Xe NMR signal is observed for the narrowed compared to the broadband Cs laser source due to increased resonant laser flux in the frequency narrowed laser.

Polarisation build up rate curves are fitted to NMR datasets such as Figures 6.5(b), 6.7(a) using an exponential fit:

$$S(t) = P_{max}(1 - exp(-\Gamma t)) \qquad (6.1)$$

where the signal, $S(t)$, varies as a function of time, t, until it reaches a maximum polarisation, P_{max} with a time constant of the buildup curve being Γ. Γ is plotted as a function of T_{cell} and excitation method in Figure 6.7(b). Optically pumping with the Cs narrowed laser provides the highest Γ values which corresponds to the fastest P_{Xe} build up rates. Although Figure 6.7(a) shows
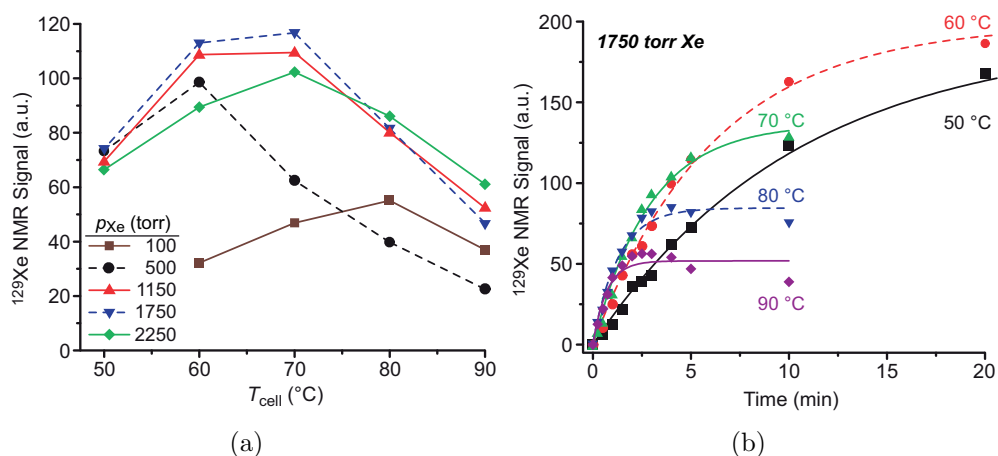
Figure 6.5: Optimal cell temperature was investigated using a Cs D_1 frequency-narrowed laser. a) Low field ^{129}Xe NMR signal acquired after 5 minutes of Cs D_1 optical pumping for a variety of T_{cell} and Xe partial pressures. b) Build up of ^{129}Xe polarisation monitored over time, increased T_{cell} above 80°C results in rubidium runaway and a poor fit to the NMR signal. Experiments performed using $\sim$60 W laser power, $\sim$0.05 nm 'blue-shifted'. Total cell pressure (balance N_2) was 2000 torr, except the 2250 torr Xe loading which had an additional 250 torr N_2.
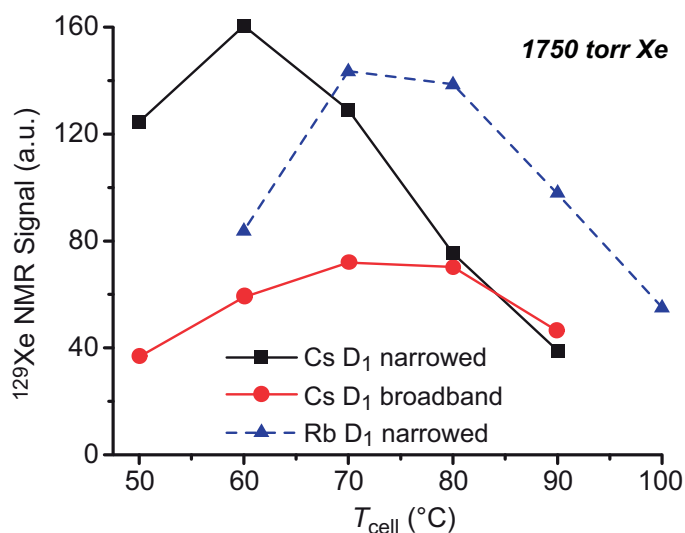
Figure 6.6: Low field ^{129}Xe NMR signal as a function of T_{cell} for Cs (narrow and broadband lasers) along with Rb narrowed laser. Similar experimental conditions were utilised: same gas loading (1750 torr Xe, 250 torr N_2), similar output laser power, data acquired after 10 minutes of SEOP, narrowed lasers were $\sim$0.05 nm 'blue-shifted'
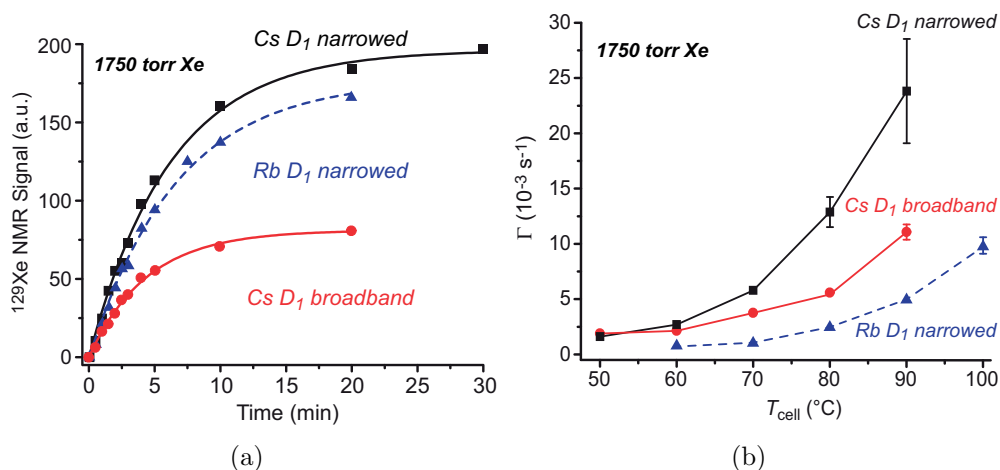
Figure 6.7: a) Three laser excitation methods are compared with optimal cell temperatures (T_{OPT}) being 70°C for Cs broadband, 60°C for Cs narrowed and 80°C for Rb narrowed. Example spectra shown for one gas mix - 1750 torr Xe, 250 torr N$_2$. b) ^{129}Xe buildup time constants, Γ, as a function of T_{cell}, faster buildup rates are shown for Cs optical pumping compared to Rb.
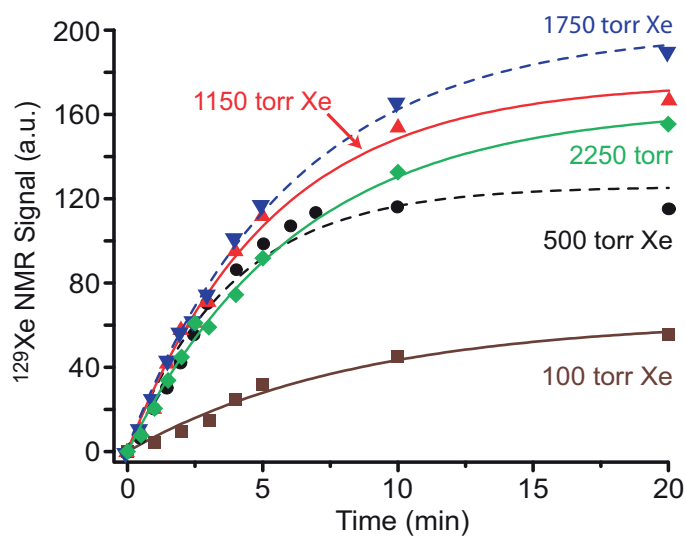
Figure 6.8: Cs-^{129}Xe NMR buildup curves shown for various partial pressures of Xe. ^{129}Xe NMR signal intensity is seen to increase with increasing Xe partial pressure except for the highest cell pressure. Experiments performed at 60°C, ~60 W laser power, ~0.05 nm 'blue-shifted', total gas pressure of 2000 torr with each mix having a balance of N$_2$, except 2250 torr Xe, which has an additional 250 torr N$_2$.

that the Cs D_1 broadband laser gives the lowest ^{129}Xe NMR signal, the buildup rate shown in Figure 6.7(b) is greater for both Cs D_1 lasers than for Rb D_1 and so it reaches it's steady state polarisation faster.

Increased build up times (Γ) are observed for the higher Xe densities (1750 torr Xe, 250 torr N_2) for a fixed total cell pressure (2000 torr), Figure 6.8. Less ^{129}Xe NMR signal was observed for the highest p_{Xe} gas loading (2250 torr Xe, 250 torr N_2), this could be due to a change in total cell pressure or due to laser limitations in the 'red-shifted' spectral offset, it may be that we were not able to optically pump under optimal experimental conditions for this gas mix.

6.1.4   Conclusions

It has been shown that Cs-^{129}Xe SEOP is a viable alternative to Rb-^{129}Xe, particularly at high Xe densities. As shown in work by Nikolaou *et al.* [8] high Xe densities are a clinical possibility with batch mode collection as it negates the need for a freeze out stage in the polariser. Hence the spin relaxation that occurs during the phase transitions is removed, [57], and the polariser design is simplified, further reinforcing the viability of Cs SEOP. Optically pumping with narrowed Cs lasers provided generally higher P_{Xe} than with narrowed Rb lasers, however, this was not as dramatic as previously observed by Whiting *et al.* [28] with Cs and Rb broadband lasers. This may be due to the limitations of the lasers not being able to fully explore the 'red-shifted' side of the absorption line.

Throughout a wide range of p_{Xe} and T_{cell} the Cs frequency narrowed laser gave increased ^{129}Xe NMR signal compared to the broadband laser. This is consistent with work on Rb-^{129}Xe SEOP by Nikolaou *et al.* [70] and further emphasises the necessity for frequency narrowed lasers for hyperpolarised xenon production when a large polarisation is required in a short space of time.

6.2   Investigations of rubidium-caesium hybrid

6.2.1   Introduction

Current laser technology is preventing full utilisation of Cs SEOP, as high power, on-resonance diodes are not available to the same standard as Rb lasers. If we had comparable laser technology for Rb and Cs, Cs would seem a better prospect for hyperpolarised noble gases than Rb, due to increased spin-exchange times and spin-exchange efficiencies. In order to aid more clinical applications of hyperpolarised gas MRI, higher polarisations would provide increased SNR and faster build up rates would allow for a higher throughput of patients who are able to be scanned in a specified time period.

The question that we wanted to investigate is whether we could apply the benefits of the larger spin-exchange cross section of Cs but with the improved laser technology that is present for Rb. This would also allow any improvements to be easily retro-fitted to current polarisers as most groups use a Rb laser with corresponding optics for the Rb D_1 wavelength. Hybrid SEOP was first proposed in a patent by Happer *et al.* in 2001 [41] with an approach being carried out on Rb-K-^{3}He by Babcock *et al.* [42], Figure 6.9. Increased build up rates were demonstrated when utilising the hybrid mixture and thus P_{max} was achieved in a shorter time scale. Hybrid SEOP relies on rapid spin transfer between the primary and auxiliary alkali metals. The primary alkali metal is the one which is optically pumped by the laser source and the auxiliary metal is polarised via spin-exchange collisions with the primary metal.

In Rb-K-^{3}He SEOP, spin exchange efficiences of hybrid cells exceeded those of pure Rb cells by an order of magnitude and the highest polarisations and polarising rates were observed with K/Rb ratios of 2-6, [42, 43]. In an anal-
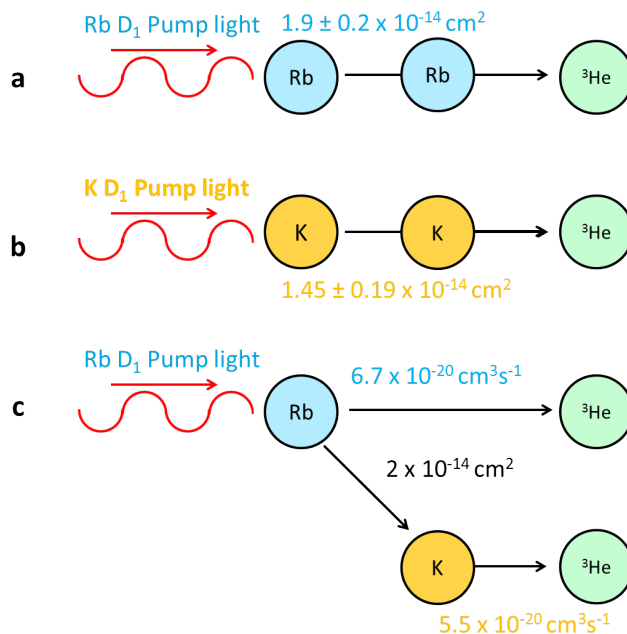
Figure 6.9: Schematics of Rb-^{3}He and K-^{3}He SEOP process. a) Rb-^{3}He SEOP using a Rb D_1 pump laser, b) K-^{3}He SEOP using a K D_1 pump laser, and c) Rb-K-^{3}He hybrid SEOP using a Rb D_1 pump laser. Numbers on the arrows denote spin exchange cross-sections and spin exchange rate coefficients, [5, 94–96].
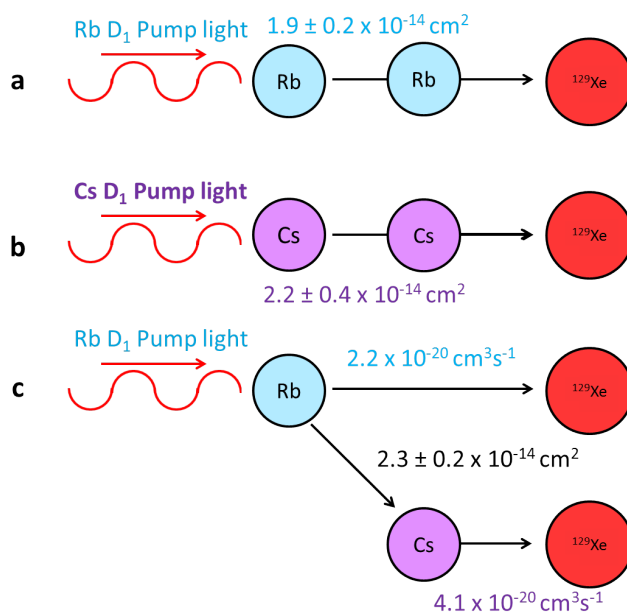
Figure 6.10: Schematics of Rb-^{129}Xe and Cs-^{129}Xe SEOP process. a) Rb-^{129}Xe SEOP using a Rb D_1 pump laser, b) Cs-^{129}Xe SEOP using a Cs D_1 pump laser, and c) Rb-Cs-^{129}Xe hybrid SEOP using a Rb D_1 pump laser. Numbers on the arrows denote spin exchange cross-sections and spin exchange rate coefficients, [5, 44–46].

ogous system for ^{129}Xe, a hybrid system was envisioned to be Rb-Cs due to the size differences and preferences for spin-exchange compared to a ^{3}He system. This system is demonstrated in Figure 6.10. Cs-^{129}Xe has a higher spin-exchange cross section than Rb-^{129}Xe SEOP (2.3 $\pm$ 0.2 x 10^{-14}cm^2 vs 1.9 $\pm$ 0.2 x 10^{-14}cm^2), [46], accordingly, it is more viable that Rb will spin exchange onto Cs than Rb or ^{129}Xe (which has a lower cross-section). Consequently, it follows that we could optically pump Rb with a Rb D$_1$ laser which would spin exchange onto Cs and then onto ^{129}Xe, with higher SE efficiency than Rb/^{129}Xe interaction.

6.2.2   Methods

Considering Figure 2.6, it is possible to see that due to colligative properties there is a depression of the melting point (liquidus) for the hybrid mixture compared to the pure Rb or Cs states. Thus if a 1:1 ratio of Rb and Cs was mixed together the liquidus point would be 9.78°C, which is dramatically lowered from the pure Rb (39.3°C) or pure Cs (28.5°C) melting points. In order to prevent loading liquid alkali metal which would never solidify at room temperatures and cause possible splashing onto the optical windows which would create local heating, we initially tried to run low ratio alkali metal combinations which were not mixed within the SEOP cell. The non pre-mixed cells were loaded with a droplet of Rb at one end and a droplet of Cs at the other
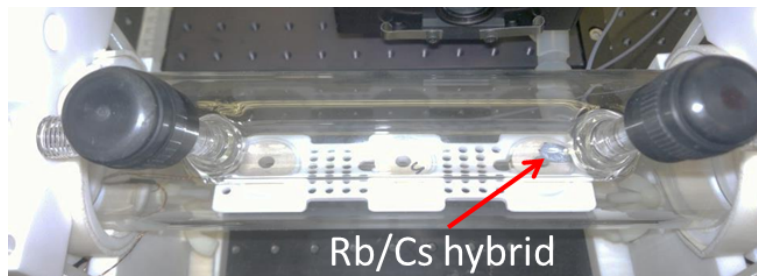
Figure 6.11: Photograph of a pre-mixed Rb-Cs-^{129}Xe hybrid cell

end. Over time, this was non-reproducible as upon cooling the alkali metal vapour would solidify onto the liquid metals and start to mix on the surface of the two metals and thus change the dynamics of the system. A small selection of results are shown here from non pre-mixed alkali metal cells before a cool down cycle and hence they can be considered as a comparison. For the higher percentage Rb in the hybrid mixture, the liquidus point approaches that of pure Rb and thus solidifies at room temperature.

The ratio of the hybrid mixture was determined by a mass balance, inside a controlled atmosphere glove box with an inert nitrogen environment. The overall aim was to weigh the components before and after alkali metal loading into a mixing tube to calculate the ratio, then calculate what quantity was transferred into the cell ($\sim$0.3 g). This was achieved by initially weighing the empty components: an empty mixing Schlenk tube with valve (m), a clean pipette and bulb (n), Rb Schlenk tube with valve (o). The pipette was then heated and Rb was transferred into the mixing Schlenk tube. After Rb transfer, the components were weighed again: mixing Schlenk tube with valve containing Rb (p), used Rb pipette bulb (q) and original Rb Schlenk tube (r). Calculate the mass of Rb transferred into the mixing Schlenk tube, mass of Rb = p-m. Consistency checks can be performed to check that m+n+o=p+q+r (i.e. original mass=final mass). This procedure is repeated for the Cs load into the mixing Schlenk tube, so now the ratio of the two metals can be determined. Once the two metals are in the mixing Schlenk tube, they need to be heated and mixed to result in a miscible liquid and then cooled to check then the mixture will solidify. To quantify the mass of the hybrid mixture being transferred into the OP cell, measure the weight of Schlenk tube, valve, pipette and bulb before and after loading. The cell should now to be ready to be aligned to the laser and filled *in situ* with a gas mixture, as described in sections 3.2.2 and 3.2.3.

For the Rb-Cs-^{129}Xe hybrid SEOP, a 60 W laser tuned to the Rb D$_1$ transition wavelength of 794.77 nm and emitting circularly polarised photons was used to perform optical pumping of Rb electrons. Several experimental tools were used to probe the pure Rb and hybrid cells to allow comparison of P_{Xe}, T_{N_2} and P_{Rb}. Polarisation build-up curves of low field ^{129}Xe NMR signal and Raman temperature were constructed by taking sequential measurements at the front, middle and back of the cell every 20 seconds for 30 minutes. These two techniques give the ^{129}Xe polarisation and the T_{N_2} *in situ* in the OP cell. In addition pump laser light absorption was measured to give an estimation of the P_{Rb} as a global measurement along the length of the cell, Figure 6.12. As discussed by Nikolaou *et al.* [8, 70], the transmitted laser light obeys the Beer-Lambert law, with the absorption, A, being

$$A = -\ln \frac{I_{hot}}{I_{cold}} \tag{6.2}$$

where I_{hot} is the intensity of light after travelling through a 'hot' cell and I_{cold} is the intensity of the pump laser light after a 'cold' cell. A 'cold' cell is defined as room temperature, $\sim$25°C and a 'hot' cell has been heated to 70-140°C for a SEOP experiment. Combining equation 6.2 with Figure 6.12(a) where the quantity of alkali metal absorbers varies with the magnetic field on or off, P_{Rb} can be computed.

$$| < P_{Rb} > | = \frac{A}{A_0} - 1 \tag{6.3}$$
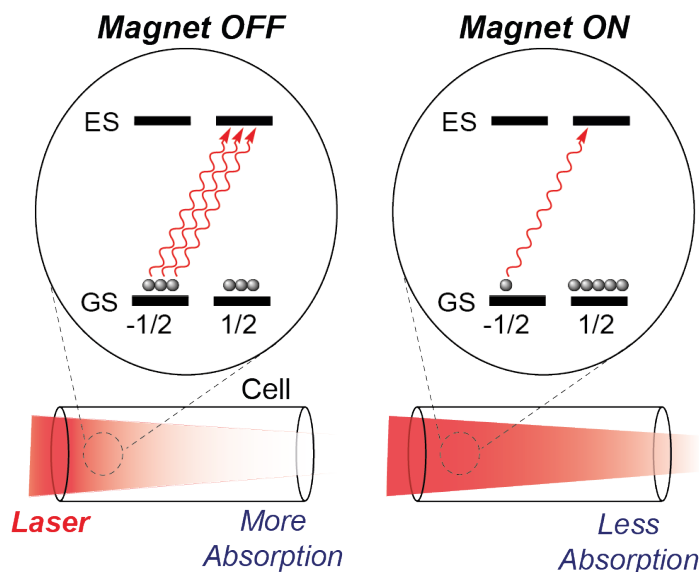
(a)
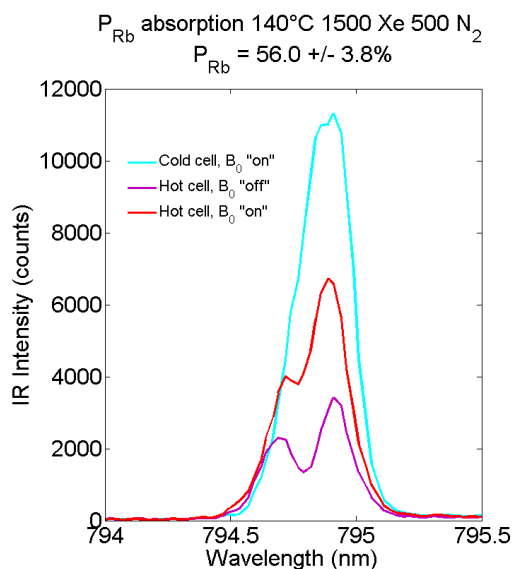
(b)

Figure 6.12: a) Methodology to estimate the alkali metal polarisation by utilising the change in pump laser light absorption with the magnetic field on and off. Near equal populations are expected in the ground electronic spin states when the magnetic field is 'off'. Consequently, a high quantity of absorbers are seen in the gas phase resulting in a large amount of pump laser light being absorbed. When the magnetic field is 'on', more efficient optical pumping occurs and thus unequal spin state distribution in the ground state, this ensues that there are less Rb electrons able to absorb the laser light. This figure assumes σ^+ circularly polarised light. Figure adapted from Nikolaou *et al.* [8]. b) Monitoring of global Rb polarisation within a hybrid cell of a 10:1 ratio of Rb and Cs. Cold cell is 25°C, hot cell is 140°C. Error bars on the Rb polarisation were determined from spectral SNR of cold cell measurements.

6.2.3   Results and discussion

Figure 6.12(b) shows that reasonably high P_{Rb} measurements have been achieved in a Rb-Cs-^{129}Xe hybrid cell, using the absorption technique described above, this is consistent with P_{Rb} being greater than P_{Xe}. In Figure 6.13, a comparison of P_{Xe} measurements is drawn between a pure Rb and a Rb-Cs (10:1 ratio) hybrid cell both in terms of overall P_{max} and the spatial distribution of polarisations across the length of the OP cell. It can be seen that the pure Rb cell has a greater variance of polarisations along the optical pumping path length compared to the hybrid cell. This could be due to the colligative properties of the two metals, which include elevation of boiling point and depression of freezing point. With the elevation of the boiling point, there would be less alkali metal in the vapour phase and thus less absorption of the pump laser light.

With Rb-K-^{3}He hybrid SEOP, as the ratio of the two alkali metals were varied, the buildup rate, Γ, and P_{max} altered. Therefore with the Rb-Cs-^{129}Xe hybrid it seems valid to also consider the ratio of the two metals. Figure 6.14 examines the effect of the ratio on the P_{Xe} over a thirty minute time period, with data being collected in the middle of the cell once a minute. It can been seen that hybrid SEOP with only a moderate quantity of Cs gives high P_{Xe}. The highest stbale P_{Xe} is observed with a 10:1 ratio (Rb-Cs), but the greatest Γ was obtained from a 20:1 ratio. Although, it looks like the Rb-Cs hybrid is approaching conditions of the pure Rb cell, with further optimisation of the hybrid state (gas mix, temperature, ratio of alkali metals, centroid wavelength, laser power) the hybrid SEOP may be able to surpass that of the pure Rb.

Further justification of the colligative properties disrupting the expected results from the Rb-Cs-^{129}Xe hybrid SEOP cell are shown in Figure 6.15. When the pure states were under investigation, e.g. Figure 6.6, the optimal operating temperature was reasonably low, with the T_{OPT} being lower for Cs than Rb as

(a)   (b)
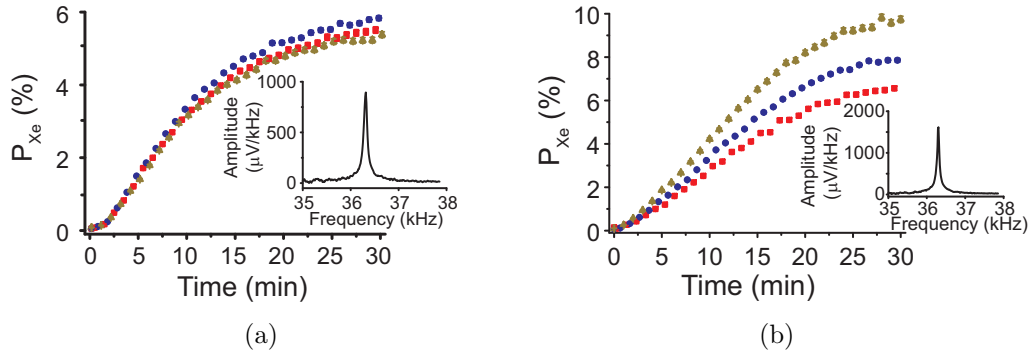
Figure 6.13: Polarisation build up curves for a) Rb-Cs hybrid cell (10:1 ratio) and b) pure Rb cell. Polarisations were measured as a function of position, front (red squares), middle (blue circles), and back (green triangles). Experimental were carried out at T_{OPT} for both cells: 140°C for hybrid and 120°C for the pure Rb cell, both had the same gas loading of 1500 torr Xe, 500 torr N_2. *inset*: NMR signal intensities.
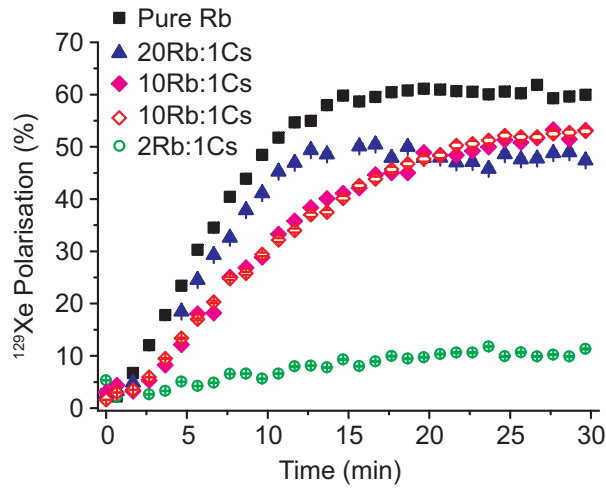
Figure 6.14: Polarisation build up curves for Rb-Cs hybrid cells as a function of ratio of the two alkali metals, considering only the middle NMR coil position. Rb-Cs-^{129}Xe exhibits high ^{129}Xe polarisations with the 10:1 ratio having the highest P_{Xe} and 20:1 ratio having the highest Γ (build up rate). The hybrid cells are approaching P_{Xe} values similar to those obtained in a fully optimised Rb cell and with further optimisation the P_{Xe} of the hybrid cell may exceed that of the pure Rb cell. Cell conditions: $\sim$60 W Rb D_1 laser light, 140°C oven temperature, 100 torr Xe, 1900 torr N_2. The open symbols denote experiments where the alkali metal was loaded into the pumping cell as separate metals, the filled symbols were pre-mixed prior to loading into the cell.

expected by the melting points and vapour pressures, Figure 2.5. However, in the hybrid state, even at 140°C the optimal operating temperature does not appear to have been located, as the highest polarisations are observed for the 140°C experiments in both the low and high xenon density mixes. Consistent with previous data published on pure Rb ^{129}Xe SEOP by Whiting *et al.* [33], the high xenon density mix, Figure 6.15(b), has a higher magnetisation as denoted by $P_{Xe}.p_{Xe}$ than the lower xenon density mix.

Finally, Figure 6.16 examines the effect of the fraction of Cs on the spatial distribution of P_{Xe} and T_{N_2} along the length of the OP cell. The build up rates of the pure Rb and 20:1 ratio hybrid cell are similar at about 0.14 and 0.15 min^{-1}, but a much lower build up rate of about 0.07 min^{-1} is observed in the 10:1 hybrid cell. As the quantity of Cs decreases, the spread of the P_{Xe} increases, but the overall average P_{Xe} seems to remain similar. The spatial distribution is also observed in the T_{N_2} values, with much elevated temperatures relative to T_{cell} observed in the pure Rb state and negligible temperature difference seen in the hybrid cell. As more SEOP appears to occur in the current experimental conditions within the pure Rb cell, more energy is dumped into the nitrogen and so this follows through to a higher rotational temperature.

(a)   (b)
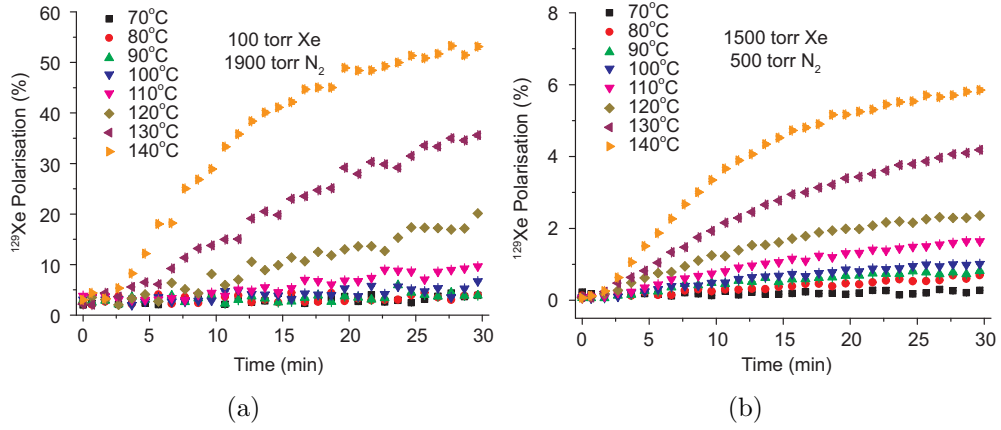
Figure 6.15: Dependence of T_{cell} on P_{Xe} for 10:1 Rb/Cs hybrid cell with two gas mixtures: a) 100 torr Xe/1900 torr N_2, and b) 1500 torr Xe/500 torr N_2). As T_{cell} increases, P_{Xe} increases and at 140°C a turning point in polarisation still has not been observed, experiments were not pursued above 140°C to prevent degrading the SurfaSil coating (as discussed in section 3.2.1). This is opposite to the effect seen in pure Rb or pure Cs cells as shown in Figure 6.6, where T_{OPT} occurs at low T_{cell} values. Despite the apparently low P_{Xe} for the high p_{Xe} mix, $P_{Xe}.p_{Xe}$ is greater (P_{Xe}=6%, p_{Xe}=1500 torr, $P_{Xe}.p_{Xe}$=9000; P_{Xe}=50%, p_{Xe}=100 torr, $P_{Xe}.p_{Xe}$=5000), which is consistent with previous results by Whiting *et al.* [33].

(a)   (b)
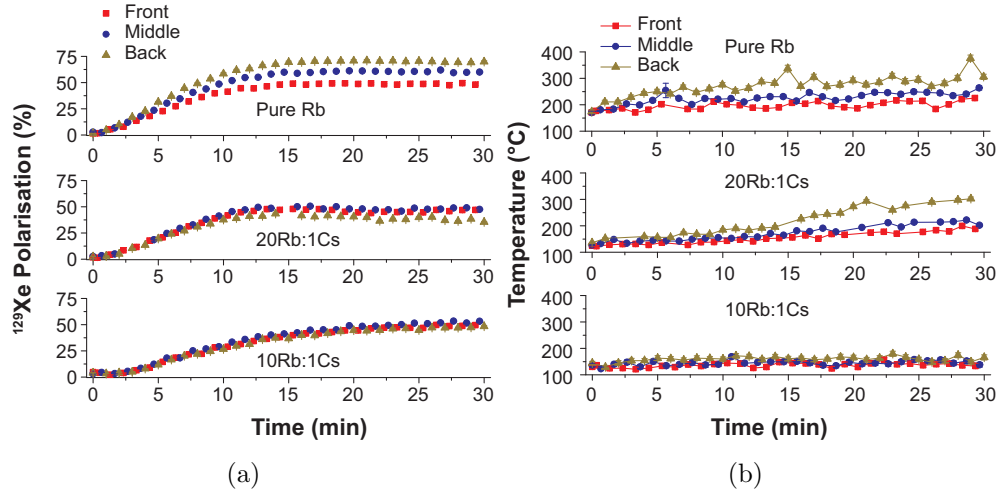
Figure 6.16: Dependence of Cs fraction on hybrid SEOP examining both performance and spatial dependence. As the quantity of Cs is reduced the P_{Xe} increases, as does the spatial distribution of the polarisations and T_{N_2} across the length of the OP vessel. T_{N_2} decreases with decreasing Cs concentration. This could be an effect of colligative properties increasing the vapour pressure of the two consistent alkali metals and thus the high temperatures are needed. Cell conditions: ~60 W Rb D_1 laser light, 140°C oven temperature, 100 torr Xe, 1900 torr N_2.

6.2.4   Conclusions

Within this section, it has been shown that as a proof of concept Rb-Cs-^{129}Xe is a viable technique with high P_{Rb} and P_{Xe}. However, from current investigations, the hybrid cells under investigation have not performed better in terms of P_{max} or Γ (build up rate) compared to the pure Rb cell. Future work within the research group will look at further optimising the hybrid state and examining more measurements to understand more about how to improve the hybrid system. These measurements would include P_{Rb} and P_{Cs}, either as described in Figure 6.12 or by utilising electron spin resonance which is described in detail by Baranga *et al.* [26], Young *et al.* [97], and Shah *et al.* [98]. In addition, *in situ* P_{Xe} and T_{N_2} allow diagnostic measurements as described above, this would be combined with measurements of spin-exchange and spin-destruction rates of Xe using steady-state polarisation build-up curves and T_1 decay measurements. Finally, a complete picture of the SEOP process could be determined by knowing about the Rb and Cs number density in comparison to pure Rb and pure Cs cells, this would justify the colligative properties arguments for lowering the combined alkali metal vapour pressure.

6.3   Summary

The choice of alkali metal for SEOP experiments has been examined in this chapter. It has been shown that Cs has a potential role in hyperpolarising noble gases with increased maximum polarisations and faster build up rates. However, Cs can't reach its full potential at this current time due to the lack of available laser technology when compared to Rb. Accordingly, a hybrid SEOP system was investigated to see if the benefits of Cs could be realised whilst pumping with a Rb D$_1$ laser via spin-exchange collisions from the Rb onto the Cs and subsequently onto the ^{129}Xe.

Chapter 7

A pathway to hyperpolarised ^{129}Xe clinical imaging

7.1 Introduction

The primary function of the lungs is to supply oxygen to, and eliminate carbon dioxide from, the blood. In order for this to occur, adequate gas exchange is required with a constant supply of fresh air and blood in the alveoli. Ventilation is the process of oxygen travelling to this gas exchange vessel where pulmonary perfusion supplies blood to the lungs so that oxygenated blood can leave the lungs. Pulmonary disorders affect the airways, alveoli, interstitium or pulmonary circulation. To aid diagnosis it is important to know how the air is regionally distributed in the lungs; whether there are airway constrictions or restrictions; and whether gas exchange is occurring effectively between the air and the blood at the alveolar walls.

Current measurement techniques include global pulmonary function tests and lung biopsies. In order to support diagnosis and treatment of lung diseases, investigations could be aided by obtaining structural and functional information in a regional manner. Regional structural information can currently be

provided by high resolution computerised tomography (HRCT) and in clinical
trials by hyperpolarised (HP) gas magnetic resonance imaging (MRI), [99].
However, a drawback of HRCT is the ionising radiation which prevents lon-
gitudinal drug development studies for managing disease progression. HP gas
MRI could aid new drug development as a non-toxic, non-ionising procedure
[61]. Regional functional information could be clinically supported by util-
ising xenon's solubility and chemical shift environment variability to obtain
dissolved and gas phase images to monitor gas exchange.

HP gas MRI is a promising future clinical tool as proton MRI is limited in the
lungs due to an intrinsic low proton density. Other issues that hinder proton
MRI functionality are respiratory and cardiac motion as well as lung deforma-
bility. In addition, there is a high susceptibility mismatch at the air/tissue
interface leading to very short T_2^*. Short T_2^* can be overcome in proton MRI
with ultra-short echo time sequences, [100, 101], but this is technically chal-
lenging. Gases have a low density and low sensitivity at normal Boltzmann
polarisation. However, hyperpolarisation greatly increases the signal at all field
strengths. The challenge of hyperpolarisation is how to make optimal use of
this non-renewable polarisation. In most studies, it is desirable to undertake
a MRI scan within the duration of a breath-hold ($\sim$15 seconds); for patients
with comprised breathing this time is further reduced, requiring short acqui-
sition times and fast imaging techniques. Fast techniques are also necessary
to examine the effects of gas diffusion. Prior to hyperpolarised ^{129}Xe clinical
MRI scanning in Nottingham, a series of calibration studies were performed.

7.2 Polarisation studies

7.2.1 Introduction

This section describes the determination of the polarisation from a sample of hyperpolarised xenon produced by a GE2000 continuous flow polariser. Polarisers were described in section 2.2, with some of the information repeated here for clarity of reading. The methodology of continuous flow polarisers is that a lean mix of xenon with its buffer gases (helium and nitrogen) are flowed through an optical pumping vessel containing rubidium which is heated via a hot air oven to create a rubidium vapour. Spin exchange occurs in this vessel between polarised rubidium electrons (optically pumped via circularly polarised light) and xenon nuclei. Upon exit from the pumping vessel, xenon needs to be separated from the buffer gases. Separation is through cryogenic collection in a liquid nitrogen trap. The xenon accumulation time, t_a, affects the polarisation decay, as stated in equation 2.14, repeated here to aid the reader, [32].

$$P_{Xe}(t_a) = P_{Xe}(t_0)\frac{T_1}{t_a}(1 - e^{-t_a/T_1}) \tag{7.1}$$

Relaxation rates, T_1, in the frozen xenon state have been found to be a constant 2-3 hours at 500 G or above (the mechanisms for the relaxation were discussed by Cates *et al.* [102], Gatzke *et al.* [103] and Morgan [104]). The 500 G field is implemented by permanent magnets surrounding the liquid nitrogen trap.

^{129}Xe polarisation calculation is determined from a series of steps, firstly, the flip angle is calibrated using a thermal xenon sample to obtain optimal signal to noise ratio (SNR) for a single shot acquisition. Then using the same flip angle for both a single scan hyperpolarised and signal averaged thermal xenon acquisition, the polarisation of the hyperpolarised sample is calculated using the steps discussed in section 7.2.2.2. Utilising these measurements, a continuous

flow GE2000 polariser was calibrated for flow rate, volume and accumulation
time to obtain optimal polarisations for future studies. A slow flow rate allows
more time for the spin-exchange process to occur between Rb/^{129}Xe within
the optical cell. However, for a set volume this requires a longer storage time
than for a fast flow rate. Following on, these xenon polarisation measurements
were compared with various wait times between a pre-calibrated polarisation
measurement station (0.2 mT) and a 1.5 T MRI scanner to examine relaxation
rates and mutual consistency between the two field strengths. A good corre-
lation is shown between the polarisation calculated at 1.5 T using a thermal
xenon sample and the pre-calibrated polarisation measurement station. It is
shown that the decay time of the polarisation in the corridor between the po-
lariser and the scanner is minimal for at least the first three minutes, with the
decay being dominated by the field gradients around and into the magnet (loss
of about 10% of the polarisation). This has implications for clinical studies as
this transfer can be controlled without hurrying into the magnet. These results
are in agreement with previous T_1 measurements of ^{129}Xe, which ranges from
a few minutes at Earth's field, (~ 5 x 10^{-5} T, [105]), through to about an hour
at typical SEOP rig magnetic fields ($\sim$30 mT, [106]) to several hours at 1.5 T.

7.2.2 Methods and results

7.2.2.1 Flip angle calibration

The same flip angle was used for the thermal and hyperpolarised signal acqui-
sition. This value was determined to gain the largest signal to noise ratio for
polarisation measurements (i.e. $\sim$90°). A flip angle calibration was conducted
using a xenon frequency tuned birdcage coil and thermal xenon sample. FiD-
CSI (Free induction Decay Chemical Shift Imaging) pulse sequence was used in
spectroscopy mode, ie. no gradients on (cfxfull = cfyfull = cfzfull = 0). A hard
pulse (to excite all frequencies) width (pw_rf1) was set to the default value of

(a) 90° pulse   (b) 180° pulse   (c) 200° pulse

(d) 90° pulse   (e) 180° pulse   (f) 270° pulse
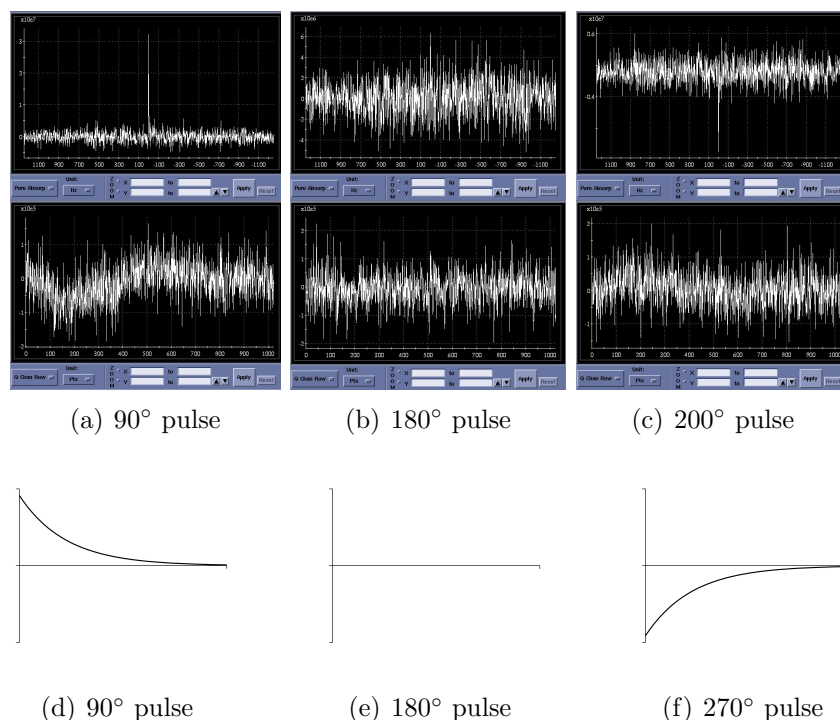
Figure 7.1: Flip angle determination, showing actual and simulated FIDs. a,b,c) top: absorption spectra and bottom: real part of FID for TG of 93, 186 and 200, approximately corresponding to 90, 180 and 200°. A 270° pulse was not possible due to constraints of a maximum TG of 200 under these conditions. d,e,f) simulated FIDs for 90, 180 and 270° pulses respectively showing the changes observed in the FID.

500 ms. The amount of radio frequency (rf) transmitted is determined by the sum of the voltage control (ia_rf1), the transmit gain (10 TG=1dB) and an attenuation factor (xmtaddSCAN) which is set to the default value of 11.5792. Increasing the ia_rf1 value, increases the amount of rf and therefore too large a number could result in multiple wraps of a spin revolution. It was found that a value of 10,000 gave a good range of values across the available TG starting with a low pulse angle, building up to a 90° pulse then dropping to a 180° pulse and confirming this by witnessing the increase of the pulse height past the 180° towards the next maximum at 270°, Figure 7.1.

In the spectroscopy prescan mode 'Q Chan Raw' - the real part of the FID and 'Pure absorp' - the real part of the fourier transformed complex data set, were

used. The xenon frequency is set to be on resonance (17,663,299 Hz), which
enabled a pulse angle calibration to be carried out using the knowledge that
a 90° pulse will be the first maximum, Figures 7.1(a) and 7.1(d). Due to the
180° pulse flipping the magnetisation into the opposite longitudinal plane, the
FID will show a flat line with no signal, due to no transverse magnetisation,
Figures 7.1(b) and 7.1(e). In a continuation of the pulse rotation, a 270° pulse
will be the next maximum but due to the opposite rotation in the transverse
plane, this will be an inverted signal, both in the FID and the absorption spec-
trum, Figures 7.1(c) and 7.1(f). This technique determined a 90° pulse to be
TG $\sim$ 93, which is used in polarisation calculations studies below.

7.2.2.2   Polarisation calibration

A GE2000 continuous flow polariser was used to produce hyperpolarised ^{129}Xe
using a 60 W Integra laser (two VBG narrowed Comet modules with a fibre
combiner), with f% xenon (typically 1-3%), 10% nitrogen and balance helium.
The polariser conditions were varied through a choice of gas flow rate and
storage time of the frozen xenon (at a field of 500 G) which determines the gas
quantity and production rate, according to equation 7.2.

$$\text{Time (min)} = \frac{\text{Volume (l)}}{\text{Flowrate (l/min)}} * \frac{100}{f} \tag{7.2}$$

Upon collection of the hyperpolarised xenon into a Tedlar bag (Jensen Inert
Products, USA), the bag is placed into a holding field of 2 mT to measure the
polarisation using a simple NMR pulse and acquire sequence, pre-referenced
to a known signal calibrated against a proton sample held at Polarean, [53].
This instrument is known as the polarisation measurement station.

The Tedlar bag containing hyperpolarised xenon is then transported to the
GE 1.5 T HDx MRI scanner. Once inside the bore of the magnet, the gas is

Figure 7.2: Two identical glass vessels used for xenon samples in MRI scanner. Left: thermal sample, right: hyperpolarised sample container.

transferred to an evacuated glass vessel ($\sim$ 200 ml volume), Figure 7.2. The sample then undergoes a spectroscopic NMR detection using a FiDCSI pulse sequence and a purpose built birdcage coil. The glass cell was subsequently attached to a pressure line to measure the pressure of xenon in the vessel using a Honeywell 26PCD pressure sensor which was used for the polarisation calculations.

Polarisation of the hyperpolarised xenon was calculated by comparison with a thermal xenon sample at 1.5 T. The thermal sample was filled with 1.046 bar oxygen and 2.870 bar natural abundance xenon, p_{th}, into a glass vessel of the same dimensions as the hyperpolarised sample, as shown in Figure 7.2, this eliminates the volume from the polarisation calculations. Oxygen was added as a relaxant for thermal xenon; it reduces the T_1 from tens of minutes for a pure Xe sample ($\sim$43 minutes for a 66 amagat sample) to less than a second, [107]. Shortening the T_1 allows for a repetition time, TR, to be selected which enables full relaxation back to the thermal equilibrium state. Jameson *et al.* [107] explored the relaxation mechanisms of pure Xe and Xe/O$_2$ mixtures.

The thermal sample was run overnight for 2048 scans for 9 hours 40 minutes

Table 7.1: Control variable parameters used on GE 1.5 T HDx MRI Scanner for polarisation studies in spectroscopy mode

Name of Control Variable	Value
Sequence	FidCSI
Coil	MNS 129Xe TR
Nucleus	129 Xe
Scan type	Axial 2D
Field of View, FOV	48 cm
Slice thickness	100 mm
Number of averages, NEX	1
Spectral width	2500 Hz
Number of points	1024
Scan mode	1 (spectroscopy)
rf pulse	0 (hard)
Repetition time (thermal), TR	17000 ms
TR_PASS	1100
Dummy time prior to scan, tlead	0
Dummy acquisitions, dda	0
Digitial gain, DG	28
Analogue gain (HP), AG	4
Analogue gain (thermal), AG	8
Transmit gain, TG	93
Frequency	17663299 Hz
Voltage transmit gain, ia_rf1	10000
x gradient, cfxfull	0
y gradient, cfyfull	0
z gradient, cfzfull	0
Save raw data file, autolock	1
rf amplitude, ia_rf1	10000
Repetition time for pass entry pt, TR_PASS	1100
Total number of scans (thermal)	2048
Total number of scans (hyperpolarised)	1

(a)   (b)
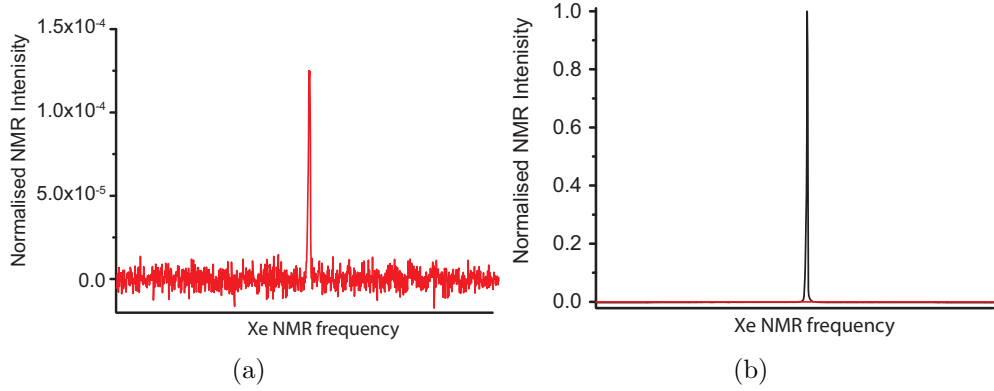
Figure 7.3: (a) Thermal and (b) hyperpolarised ^{129}Xe NMR normalised signal intensities acquired on a 1.5 T MRI system. (b) also shows the difference in signal intensity between the thermal (red line) and hyperpolarised (black line). Signals were acquired using parameters in Table 7.1.

and 16 seconds to obtain a good SNR. Due to a phase correction applied by the scanner, alternate FIDs were flipped by 180°. Consequently, it is necessary to accumulate the scans by multiplying each alternate scan by -1. To obtain a thermal spectrum which has an equivalent signal intensity to a single scan, the scans were accumulated and divided by the number of scans. Both the thermal, Figure 7.3(a), and hyperpolarised samples, Figure 7.3(b), were scanned using the same control variables, see Table 7.1. A few differences between the two scans were the total number of scans and the gain settings for the smaller thermal signal. The analogue gain was changed by 12 dB and accounted for by multiplying the hyperpolarised spectrum by 3.98 to get equivalent settings.

To compute the hyperpolarised xenon polarisation, firstly, it is necessary to obtain the pressure of the hyperpolarised xenon gas, p_{HP}, using a pressure sensor. The sensor records a voltage measurement, so this is converted to pressure using the manufacturer conversion factor of 3.33 mV/psi. The signals of the hyperpolarised and equivalent single scan thermal spectra are determined, taking into account the changes in gain settings. There are several stages which are analogous to the polarisation calculation steps laid out earlier in section 3.3.2.1; the thermal xenon polarisation, p_{th}, is calculated using equation 3.3.

Considering this value, a polarisation enhancement factor, $\epsilon_{enhance}$, aids in determining the hyperpolarised polarisation, equation 7.3 is similar to equation 3.7 described earlier.

$$\epsilon_{enhance} = \frac{S_{HP}}{S_{th}} * \frac{p_{th}}{p_{HP}} \tag{7.3}$$

Finally, the percentage hyperpolarised xenon polarisation, P_{HP}, is calculated using equation 7.3 which is equivalent to equation 3.9, with the error on P_{HP} being based on the SNR of the thermal xenon signal, such as it is in equation 3.10.

$$P_{HP} = \epsilon_{enhance} * P_{th} * 100 \tag{7.4}$$

7.2.2.3 Characterisation of the GE polariser - flow rate, storage time, volume of gas produced

According to equation 7.2, parameters of flow rate and storage time can be varied to give optimum conditions for a desired volume of gas. As previously discussed in section 7.2.1, a balance needs to be sought between the residence time of the gas within the optical cell where it is polarised and the time for which the gas needs to be stored in its frozen state to allow accumulation to a specific volume. T_1 relaxation will decrease the ^{129}Xe polarisation, due to the gas being stored in the frozen state for long periods of time, see equation 7.1. For small volumes of gas (Figures 7.4(a) and 7.4(b)), a short accumulation time is needed in the frozen state and therefore slower flow rates can be used to obtain relatively high polarisations of $\sim$5.5%. When the frozen xenon storage time increases with increasing gas volume (Figures 7.4(d) and 7.4(f)), the flow rate to obtain the optimal polarisation needs to increase correspondingly. For the gas mix used in Figure 7.4 of 3% xenon, 10% nitrogen, and 87% helium, the optimal conditions for the highest polarisations are: 0.2 l bag, 0.5 l/min
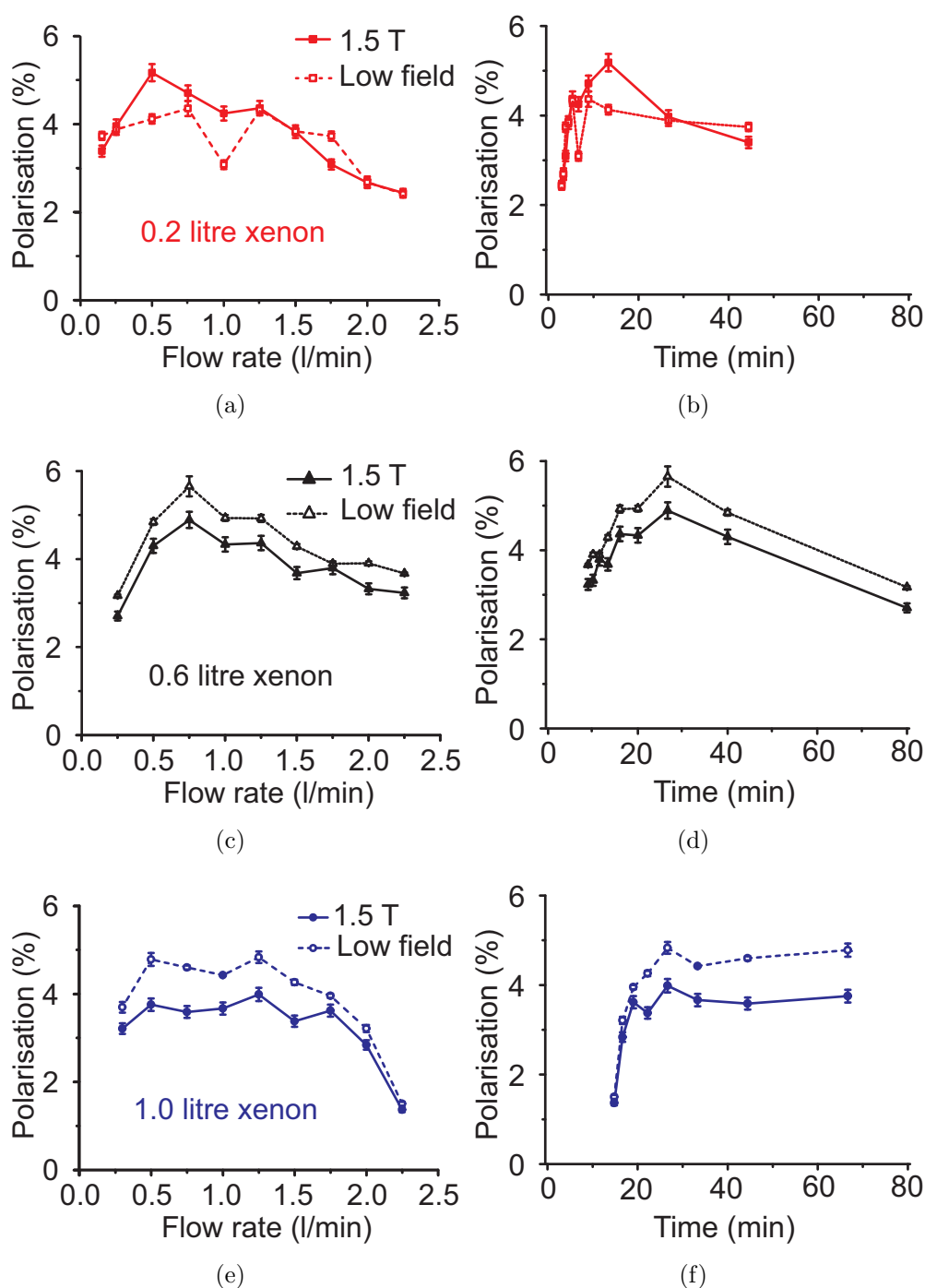
Figure 7.4: ^{129}Xe polarisation as a function of flow rate (left) and time (right) for three volumes of gas. A 0.2 l (red) bag of xenon would be suitable for a flip angle calibration or phantom study, whereas a 0.6 l (black) or 1.0 l (blue) bag of xenon would be suitable for a subject to breath in during a clinical study. Polarisations are measured at ∼2 mT and subsequently at 1.5 T. Gas mix: 3% xenon, 10% nitrogen, and 87% helium.

flow rate and 13 min 20 s storage time; 0.6 l bag, 0.75 l/min flow rate and
26 min 40 s storage time; and 1.0 l bag, 1.25 l/min flow rate and 26 min 40 s
storage time.

This study also compared the polarisations obtained at low field ($\sim$2 mT, po-
larisation measurement station) and subsequently at 1.5 T (GE HDx clinical
scanner). This study aimed to mutually verify the calibrations of both sys-
tems, as polarisation measurements should be similar but lower for 1.5 T due
to losses on transfer into the scanner and T_1 relaxation. Figure 7.4(a) shows
a rough correlation between the two magnetic fields but random fluctuations
are observed. These fluctuations arise from the polarisation measurement sta-
tion's lack of ability to measure accurate polarisations for a small volume of
gas. This is due to the region of interest above the NMR surface coil being
about 2.54 cm and if the volume of gas doesn't fill this region, even with com-
pression of the bag to attempt to fill the required volume, then the results will
not be as consistent. This is overcome with the larger volumes of gas (0.6 l
and 1.0 l) in Figures 7.4(c) and 7.4(e). A good correlation is seen in these
examples with the polarisation being higher at the polarisation measurement
station than at 1.5 T due to T_1 decay and transfer through field gradients
causing further loss in polarisation.

7.2.2.4 Polarisation decay tests

Further to the mutual consistency and polarisation optimisation tests shown in
Figure 7.4, further studies probed the hyperpolarised gas signal at low field pre
and post being held at 1.5 T. Polarisation was measured prior to a scan in the
2 mT field of the polarisation measurement station and then after transfer to
the glass vessel in the 1.5 T magnet. The residual gas remaining in the Tedlar
bag, which has experienced a field of 1.5 T but not an NMR pulse (due to non-
complete transfer into the glass vessel), is transferred back to the polarisation

measurement station. Here the xenon polarisation is measured to determine
the signal decay due to time and the field gradients during transportation
to and from the magnet. Unfortunately due to the permanent magnets used
during the freeze/thaw cycle in the polariser, it was not possible to measure
the ^{129}Xe polarisation *in situ* within the OP cell. Reasonable consistency was
shown between the different magnetic field measurements, as shown in Figure
7.5 on the right hand side of the plot.

In addition, the study probed the decay of the polarisation when delayed in
transit between the polariser and the MRI scanner, at the position of the red
star shown in Figure 7.6, for varying periods of time between 0 seconds and
20 minutes is as shown in Figure 7.5. The field at this position was measured
to be 0.08 mT in the direction of the Earth's field (typically $\sim$ 0.05-0.06 mT);
this slightly elevated field helped to maintain the ^{129}Xe polarisation, with only
about a 45% drop after 20 minutes. Relaxation of the gas is further increased
due to moving the sample through the magnetic field lines: from the polariser
via the measurement station and through to the 1.5 T clinical scanner. Relax-
ation due to magnetic field gradients was investigated by Schearer *et al.* [108]
who proposed that the Brownian motion of spins causes randomly fluctuating
magnetic fields thus influencing the spin-lattice relaxation time.
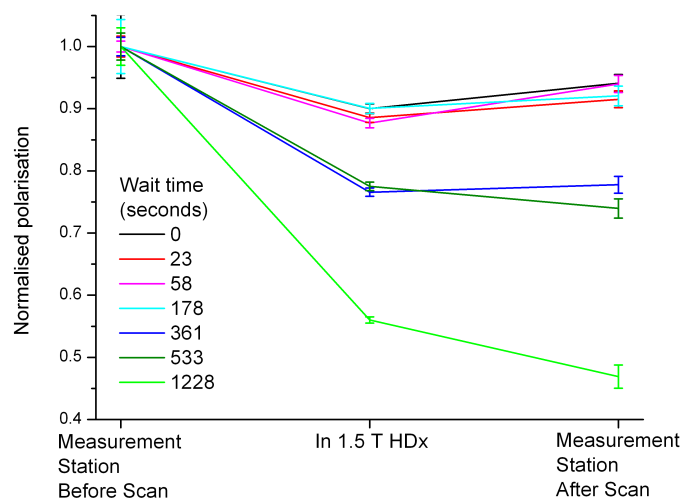
Figure 7.5: ^{129}Xe Polarisation measurements before, during and after transportation to the 1.5 T scanner. Measurements before and after 1.5 T scan were acquired on the polarisation measurement station at $\sim$2 mT. Wait times are defined as the period that the bag was held stationary between the polarisation measurement station and MRI scanner, so relaxation is affected most between the first two measurements.
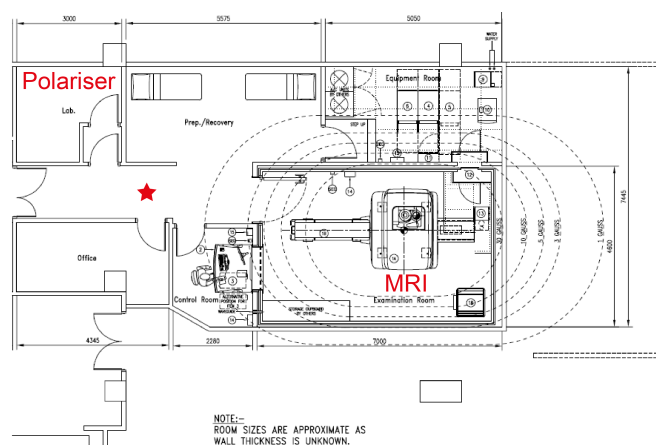
Figure 7.6: Site Plan showing location of the ^{129}Xe continuous flow polariser, MRI scanner and position of Tedlar bag containing hyperpolarised xenon, during wait times shown in Figure 7.5, which is indicated by the red star. Floor plan from GE Site Planning for 1.5 T scanner.

7.3 Imaging modalities

7.3.1 Proton lung imaging

To enable utilisation of hyperpolarised Xe^{129} for clinical use, a proton MRI image of the lung needs to be acquired as a localiser in order to visually examine the lung cavity such that the hyperpolarised lung images can be overlayed onto an anatomical image and any defects or blockages observed. Proton MRI of the lung is inherently difficult for several reasons. The first is the low quantity of tissue that is present in the lung, which leads to an inherently low proton mass making conventional proton MRI difficult. The second problem experienced is the rapid signal decay from the short T_2^* values due to the multiple air and fluid interfaces. Finally there will be motion artefacts due to respiratory, cardiac and vascular motion. The final two difficulties are lessened by having short echo times. Short echo times enables overall fast scan times which facilitates the subject to be able to hold their breath for the length of the scan thus reducing the respiratory motion. However, there are hardware and software constraints with ultra short echo times.

Cardiac motion can either be reduced by cardiac gating or short repetition times. Cardiac gating would appear initially to be the preferred scenario as short repetition times prevent full recovery of the proton signal to its initial state. However, unfortunately, cardiac gating slows the sequence down dramatically as the k-space lines can only be acquired at a specific time in the cardiac cycle and the sequence can no longer be acquired within a breath-hold.

Motion artefacts can cause blurring or ghosting in an image, for example, cardiac motion causes noise running through the heart in the phase encoding direction. In addition artefacts can arise from phase wrapping if the dimen-
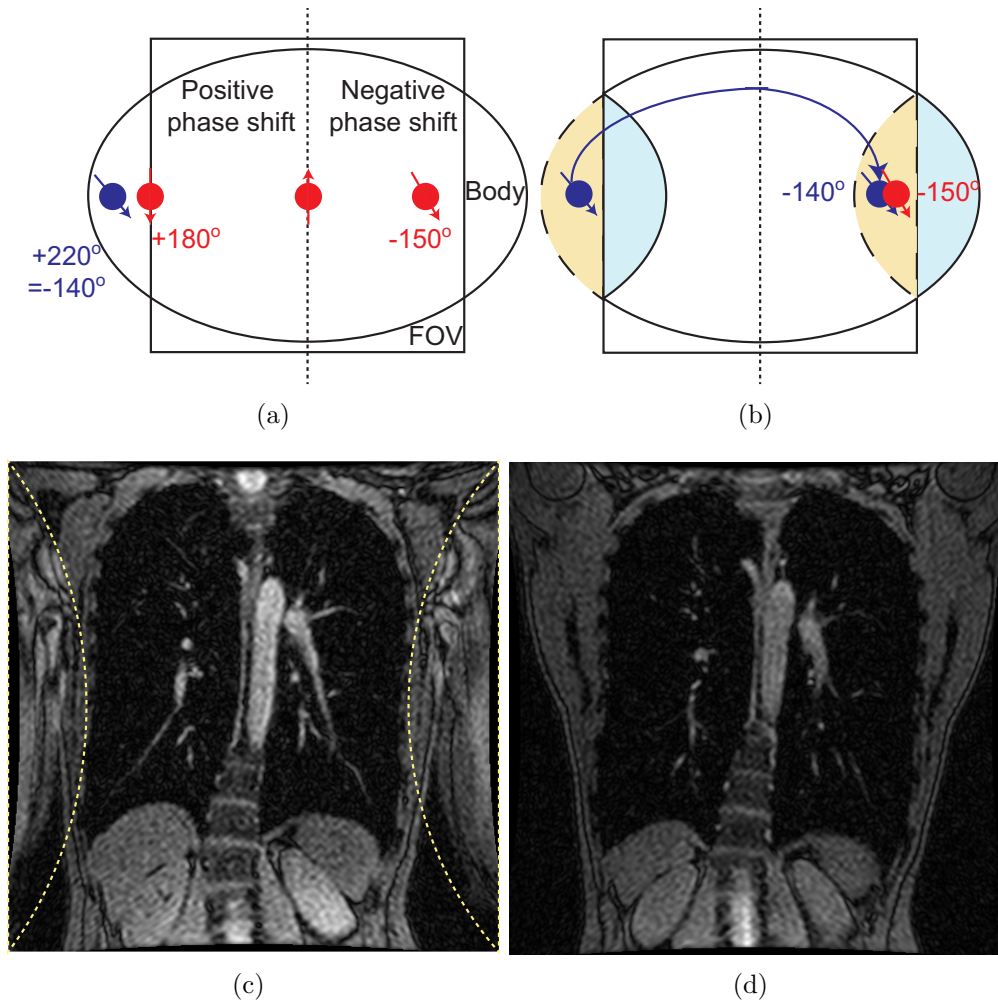
Figure 7.7: Schematic showing the origin of phase wrapping. This occurs when the field of view (FOV) is smaller than the volume of interest (a). When phase shifts outside the FOV (blue spins), exceed +180° or are less than -180°, they are mapped onto a phase shift within the region of interest. For example, a shift of +220° and is mapped onto -140° (b). This results in the same spatial encoding as spins within the FOV and overlapping occurs. If the object extends outside the right hand side of the FOV, it will be wrapped onto the left hand side of the image and vice versa, denoted by the coloured areas in (b). The effect of this aliasing is shown in two MRI scans with arms down (c) with phase wrapping (denoted by yellow dashed lines) as the arms are outside the FOV and arms up (d) where an image is produced without aliasing. Scans were performed on a healthy male volunteer using a Fast GRE pulse sequence with a flip angle of 10°, TE: 2.2 ms, TR: 4.8 ms, matrix size: 128 × 128, FOV: 38 cm × 38 cm, slice thickness: 5 mm, scan time: 0.672 s. Figures (a) and (b) based on concepts in [109].

sions of the object being scanned are greater than the field of view (FOV), as
shown in Figure 7.7. Phase encoding errors arise as the scanner assumes that
the phase range of spins in the region spans from -180° to +180°. However,
regions of the object lying outside of the FOV are assigned a phase >+180° or
<-180°, and these phases are folded onto the region of interest. For example, a
phase +220° in Figure 7.7(a) is given the same phase encoding as -140°, shown
in Figure 7.7(b). This results in multiple spins with the same phase encoding
and thus overlapping occurs on the image, as shown in Figure 7.7(c). Phase
wrapping can be avoided by including all of the region of interest within the
FOV, either by increasing the FOV or, for the upper body, by placing the arms
above the head, as shown in Figure 7.7(d). An inbuilt scanner algorithms such
as 'no phase wrap' could be used to prevent the aliasing by oversampling the
object outside the region of interest (i.e. increasing the FOV) but then dis-
carding this additional information before reconstruction, so that the apparent
FOV is not increased.

Speed of image acquisition is very important with lung imaging, as it enables
dynamic studies, reduces the likelihood of motion artefacts and enables breath-
hold imaging without respiratory motion. Two sequences were compared in
Figure 7.8: a fast GRadient Echo (GRE, used in Figure 7.7) and a Fast Imag-
ing Employing Steady State Acquisition (FIESTA). FIESTA is also known as
FISP (Fast Imaging with Steady state Precession) and balanced Fast Field
Echo (FFE). Both of these sequences are gradient echo sequences. Gradient
echoes are generated by reversing the gradient in the frequency encoding di-
rection (X gradient in Figures 7.8(a) and 7.8(b)). GRE sequences with short
repetition times (TR), do not allow time for the transverse magnetisation to
decay before the next TR, and this 'left over' magnetisation needs to be dealt
with. For Fast GRE the magnetisation is destroyed by switching the slice
select gradient with opposite polarity to dephase the spins before the next cy-
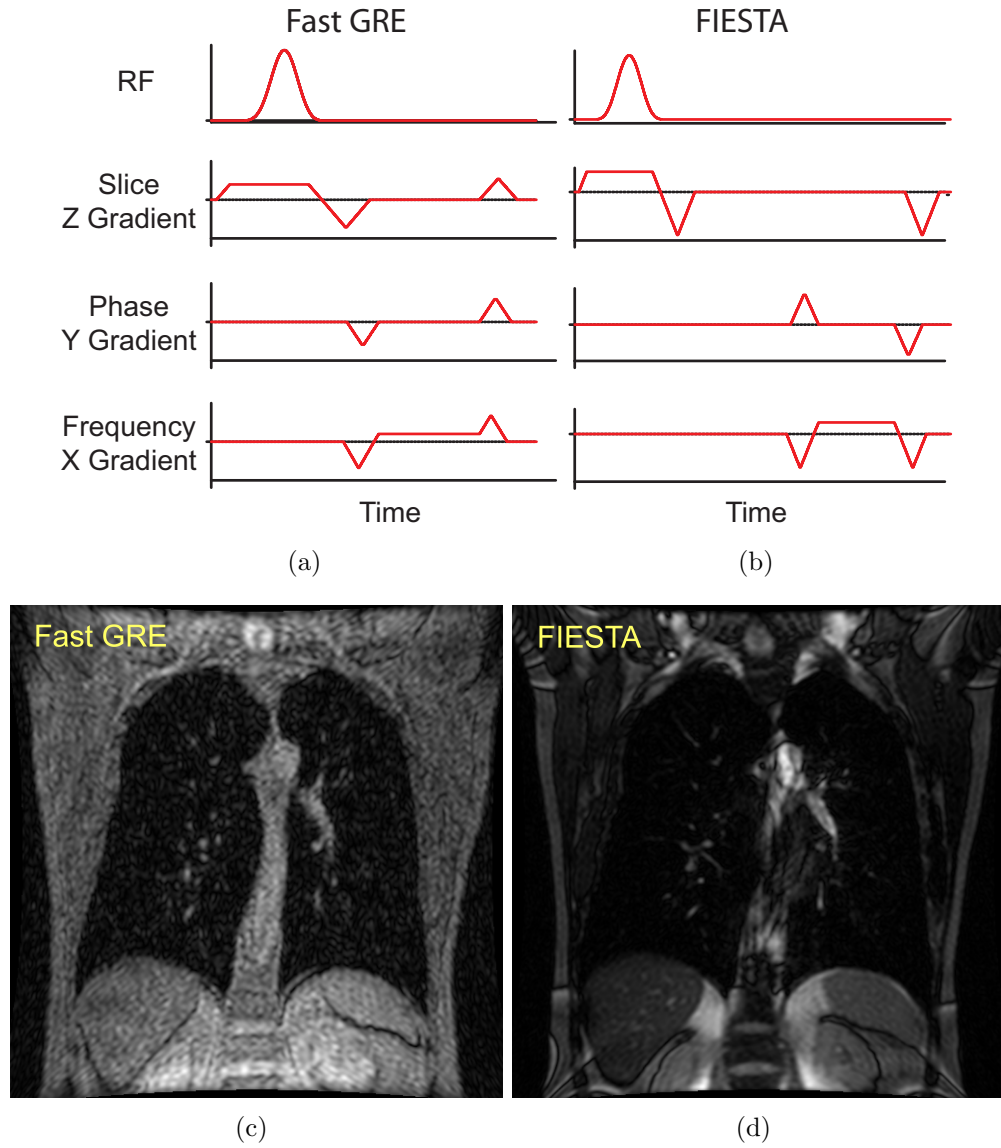
Figure 7.8: Comparison of pulse sequences and proton MRI scans for (a) and (c) spoiled (Fast GRE), and (b) and (d) refocused (FIESTA) gradient echo sequences, performed on a healthy male volunteer. Fast GRE scan parameters: flip angle: 10°, TE: 1.3 ms, TR: 3.8 ms, NEX: 1, matrix size: 128 x 128, FOV: 40 cm x 40 cm, slice thickness: 5 mm, scan time: 0.536 s. FIESTA scan parameters: flip angle: 50°, TE: 1.3 ms, TR: 3.1 ms, NEX: 1, matrix size: 128 x 128, FOV: 40 cm x 40 cm, slice thickness: 5 mm, scan time: 0.458 s.
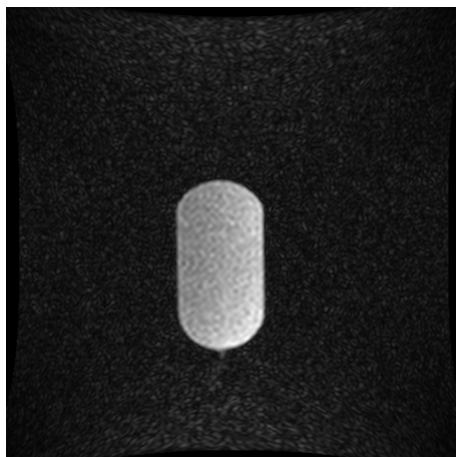
Figure 7.9: Hyperpolarised ^{129}Xe MRI scan inside a glass phantom, acquired using a fast GRE pulse sequence with an actual flip angle of ∼3° (100° set on scanner), TE: 4.9 ms, TR: 11 ms, NEX: 1, matrix size: 128 x128, FOV: 48 cm x 48 cm, scan time: 2 s, ^{129}Xe polarisation: 4.6 ± 0.1%. Acquisition parameters of ^{129}Xe: flow rate: 0.75 l/min, volume of gas: 0.6 l, storage time in frozen state: 26 min 40 s, percentage xenon in gas mix: 3%, these were optimal conditions for a 0.6 l bag as noted in 7.2.2.3.

cle; this is known as spoiling. FIESTA uses unspoiled sequences and instead refocuses the transverse magnetisation so that it is preserved from one TR cycle to the next, Figure 7.8(b), which enables shorter scan times. Due to the transverse magnetisation being refocused, a higher flip angle can be utilised in the FIESTA sequence and a sharper MRI scan is obtained for FIESTA, Figure 7.8(d), compared to Fast GRE, Figure 7.8(c). In these images, the scanner 'autovoice' was selected to synchronise the scan with asking the subject to breathe in and hold their breath and then after the scan to relax and return to normal breathing.

7.3.2 Hyperpolarised ^{129}Xe MRI imaging

Hyperpolarised MRI requires highly efficient sequences because there is no recovery of the magnetisation (without going through the hyperpolarisation process again). The magnetisation decays due to T_1 relaxation and the excitation pulses. A pulse sequence needs to be fast on the time scale of the T_1 of the sample. For pure ^{129}Xe gas at 1.5 T, the T_1 is a few hours, whereas *in*

vivo this drops to minutes. For a ventilation image, the typical scan time is
about 2 s per slice, as shown in Figure 7.9, which means negligible T_1 decay
is occurring over the time scale of the image acquisition.

7.4   Summary

This chapter has demonstrated the techniques that will be required for hy-
perpolarised ^{129}Xe functional lung MRI scans in Nottingham. Methods have
been discussed as to how to obtain a measure of ^{129}Xe polarisation on a 1.5 T
GE HDx scanner and comparisons were drawn to low field ($\sim$2 mT) ^{129}Xe po-
larisations. This allowed optimal conditions for hyperpolarising ^{129}Xe to be
achieved using a GE ^{129}Xe continuous flow polariser. These parameters take
into account a balance between the rate of flow of gas through the cell along
with the storage time of the frozen xenon. The flow rate alters the gas residence
time within the SEOP cell and thus the time available to allow spin-exchange
processes to occur between Rb and ^{129}Xe. Xenon is frozen to separate it from
its constituent buffer gases and to allow accumulation of large volumes. These
optimal specifications were subsequently used to acquire a ^{129}Xe MR image in
a phantom. Furthermore, proton lung MRI has been examined to obtain op-
timal parameter sets for localisation scans which can be used in future clinical
trials in Nottingham.

Chapter 8

Conclusions

This thesis is focused on probing the spin exchange optical pumping process with multiple techniques, under different experimental conditions. The various techniques outlined include low field NMR spectroscopy, near-IR optical absorption and *in situ* Raman spectroscopy. Xenon polarisations were measured using three surface NMR coils which are placed at the front, middle and back of the optical pumping cell to obtain spatial P_{Xe} values. An estimation of the rubidium polarisation was obtained by measuring the amount of pump laser light absorption with the magnetic field on and off. Energy transport and internal gas temperatures (T_{N_2}) were investigated using *in situ* Raman spectroscopy. Walter *et al.* [51] showed that energy transport is an important topic within SEOP, as thermocouples exterior to the OP cell are not a good indication of the internal gas temperatures. We have followed on from Walter's studies to look at high powered frequency narrowed lasers in the absence of helium as a buffer gas. Due to the advent of frequency narrowed lasers, SEOP experiments no longer require helium to pressure broaden the Rb D_1 absorption line. As part of the investigations, the orientation angle of the detection and excitation optics within the Raman instrumentation was examined. Firstly, the optics were arranged perpendicularly to allow the probe laser light to be spatially filtered by the arrangement. This method also utilised the

internal baffles of the spectrometer to physically block the light from entering the spectrometer. Due to the need for the optical pathways to be aligned to sub-mm accuracy, improvements can be made in experimental consistency by having the pathways arranged along the same optical plane. This idea is utilised in a new 180° geometry inline module, with the addition of optical notch filters to reduce the optical transmission of non-Raman scattered lines by many orders of magnitude. This module enables ultra-low frequency Raman scattering to be performed on a gas sample, with a ∼23 fold improvement in SNR compared to the conventional orthogonal arrangement using the same acquisition parameters.

SEOP conditions were investigated under different parameters, including Xe density, laser linewidth, temperature and alkali metal. Xe has a much lower thermal conductivity than N_2 (0.70 x 10^{-2} $Wm^{-1}K^{-1}$ compared to 3.09 x 10^{-2} $Wm^{-1}K^{-1}$), with correspondingly higher T_{N_2} values observed at the highest xenon partial pressures (p_{Xe}) for a fixed total cell volume. This corresponded to the region of highest signal intensity, $P_{Xe}.p_{Xe}$. Narrowing of the laser linewidth, increased the xenon polarisation of a sample as previously shown by Whiting *et al.* [71]. This was further investigated with the use of Raman spectroscopy to look at temperatures changes as probed across the cell, perpendicular to the SEOP pump laser. Internal gas temperatures were elevated by hundreds of degrees at the centre of the cell with the frequency narrowed laser, whereas only a few tens of degrees with the broadband laser due differences in resonant photon energy for the same overall laser power. At the cell walls, the gas temperature corresponded to the oven temperature measured by the thermocouple, leading to uneven heating across the vessel. This heating phenomena was also investigated along the length of the optical cell, parallel with the pump laser to obtain P_{Xe} and T_{N_2} values at the front, middle and back of the cell. Under steady state conditions, T_{N_2} and P_{Xe} were observed to

be largest at the back of the cell with a temperature and polarisation gradient exhibited across the cell. When rubidium runaway takes place, a process where P_{Xe} initially has fast buildup and then a dramatic drop to a lower P_{Xe} value, the temperature gradient switches as the back internal gas temperatures become the lowest. It is proposed that this is due to increased light absorption at the front of the cell and so less light penetrates to the back. This means that unpolarised rubidium at the rear of the cell is not able absorb the light and therefore no heat is transferred via non-radiative collisions to the nitrogen. Rubidium runaway can be alleviated by several methods discussed in Chapter 5 including lowering the overall temperature of the cell to reduce the rubidium number density, spatially monitoring and altering the oven temperature via feedback loops, [88], removing the rubidium from the laser line thus removing this heating effect and enabling more control over the rubidium number density, [55], and taking advantage of the increased spin exchange times during rubidium runaway but then lowering the cell temperature to a stable P_{Xe} to avoid the detrimental effects of this process, [93].

Along with rubidium, caesium was also investigated as the alkali metal of choice for SEOP experiments. Cs has been shown to have a higher spin exchange cross-section with xenon than Rb and is particularly effective at high Xe densities. In a previous study by Whiting *et al.* [28], Rb and Cs SEOP were compared using comparable broadband lasers and an approximately two-fold improvement in spin polarisation was observed. In this thesis, a similar comparison was made utilising frequency-narrowed lasers, it was seen that Cs optical pumping under these conditions produces higher polarisation than Rb but the same gains were not seen as with the broadband lasers. It is currently believed the reason for this is due to the limitations in the laser technology of the Cs laser, as it was not possible to have tuning across the whole spectral range of the Cs D_1 transition. Due to these restrictions in being able to

utilise the full potential of Cs SEOP, a hybrid alkali metal SEOP experiment to use Rb D_1 optical pumping and then spin exchange onto the Xe via Cs was studied. Dependencies of various ratios, temperature and gas mix were investigated, with high P_{Rb} and P_{Xe} being observed. Currently, the Rb/Cs hybrid does not have a increased P_{Xe} compared to pure Rb, but it does have comparable polarisation rates. With further work into this field, it is proposed that a future improvement to ^{129}Xe polarisers might be able to use this hybrid method without having to change the laser or optics, which are generally the most expensive parts of a polariser.

Finally, the thesis concludes with the purpose of studying the SEOP process within our lab, as it will be used as a tool for studying lung diseases with clinical lung MRI. Measurements of thermal and hyperpolarised ^{129}Xe NMR signals are performed at 1.5 T to enable polarisation measurements to be calculated and compared to a pre-calibrated 2 mT helmholtz coil measurement station. Polarisations were compared at different volumes, accumulation times and flow rates to allow calibration of the polariser for future studies. There is a balance needed between the flow rate, which controls the gas residence time and thus the time available for spin exchange between Rb and ^{129}Xe, along with the accumulation time of xenon in the frozen state. Following on from this, proton MRI localisation scans of the lungs were investigated as co-registration of ^{129}Xe MRI scans. Sequences for proton lung MRI were compared and artefacts discussed.

Appendix A

Calculation of rotational constant of nitrogen

The rotational partition function for a diatomic molecule is

$$q_R(T) = \sum_{J=0}^{\infty} \exp\left(\frac{-J(J+1)\theta_R}{T}\right) \tag{A.1}$$

where θ_R is the rotational temperature as defined by

$$\theta_R = \frac{B}{k_B} = \frac{h^2}{8\pi^2 I k_B} \tag{A.2}$$

where I is the momentum of inertia of a molecule, $I = \mu r^2$, with μ being the mass of the molecule and r is the bond length. Given that the N_2 bond length is 53 pm [38] and the mass is 28.02 m_u (atomic mass constant), the momentum of inertia, I, is 1.31 x 10^{-46} kgm^2. Therefore the rotational constant can be calculated to be 6.42 x 10^{10} s^{-1}. This is converted to wavenumbers using

$$\bar{\nu} = \frac{\nu}{c} \tag{A.3}$$

where $\bar{\nu}$ is wavenumbers, ν is frequency, and c is speed of light, to give 2.14 cm^{-1} as the rotational constant of nitrogen. This is converted into Joules

to allow calculation of the rotational temperature, using

$$E = h\nu \tag{A.4}$$

This gives B with a value of 4.25 x 10^{-23} J, thus the rotational temperature
is calculated to be 3.08 K using equation A.2. At this rotational temperature
the thermal energy $(k_B T)$ is comparable to the spacing between the rotational
energy levels (hcB) and therefore the rotational energy levels are populated
above this temperature.

Conference Proceedings

Oral presentations

1. **Hayley Newton**, Jason Skinner, Jonathan Birchall, Nicholas Whiting, Brogan M. Gust, Kaili Ranta, Michael J. Barlow, & Boyd M. Goodson; *Can We Utilise Rb/Cs Hybrid Optical Pumping to Hyperpolarise Noble Gases?*; 55th Experimental Nuclear Magnetic Resonance Conference 2014, 24 March 2014, Boston, USA

2. **Hayley Newton**, Nicholas Whiting, Michael J. Barlow, Peter Morris, Laura Walkup, & Boyd M. Goodson; *Effects of various spin-exchange optical pumping conditions on gas temperatures measured by Raman spectroscopy during production of hyperpolarised* ^{129}Xe; XeMat 2012 (Xenon in Materials), 29 June 2012, Dublin, Ireland

Travel grants awarded

1. ENC Ritchey Travel Award 2014 for the 55th Experimental Nuclear Magnetic Resonance Conference 2014

2. COST Trainee Grant TD1103, August 2013

3. Student Travel Stipend for the 54th Experimental Nuclear Magnetic Resonance Conference 2013

4. University of Nottingham Graduate School Travel Prize for travel to the 54th Experimental Nuclear Magnetic Resonance Conference 2013

5. UK NMR Discussion Group Travel Bursary for Euromar 2012

Conferences attended

1. 22nd ISMRM Meeting (Joint annual meeting ISMRM/ESMRMB), Milan, Italy, 12-16 May 2014

2. 55th Experimental Nuclear Magnetic Resonance Conference, Boston, MA, 23-28 March 2014

3. European Society for Magnetic Resonance in Medicine and Biology - Acquisition strategies for hyperpolarised spin systems, 25-27 August 2013, Lyngby, Denmark

4. 20th Annual British Association for Lung Research Summer Meeting, 'Curing Pulmonary Fibrosis: The Holy Grail', 10-12 July 2013, Nottingham, UK

5. 54th Experimental Nuclear Magnetic Resonance Conference, Pacific Grove, CA, 14-19 April 2013

6. GE EPIC Programming Course for Pulse Sequencing Development, 4-7 March 2013, Nottingham, UK

7. Euromar 2012, 1 - 5 July 2012, Dublin, Ireland

8. XeMat 2012 (Xenon in Materials), 27-29 June 2012, Dublin, Ireland

9. COST Action TD1103 'European Network for Spin Hyperpolarisation Physics and Methodology in NMR and MRI', 29 June - 1 July 2012, Dublin, Ireland

Posters

2014

1. Jason Skinner, **Hayley Newton**, Jonathan Birchall, Nicholas Whiting, Michael J. Barlow, & Boyd M. Goodson; *Using in-situ Raman and NMR Spectroscopies to Map the Dependences of Spin-Exchange Optical Pumping and Energy Transport on Xenon Density*; 55th Experimental Nuclear Magnetic Resonance Conference, March 2014, Boston, USA

2013

1. **Hayley Newton**, Jason Smith, Laura Walkup, Nicholas Whiting, Michael J. Barlow, Peter Morris & Boyd M. Goodson; *Effects of Gas Composition on Optical Pumping and Energy Transport for Hyperpolarized ^{129}Xe Using in situ Raman Spectroscopy and NMR*; 54th Experimental Nuclear Magnetic Resonance Conference, April 2013, California, USA

2. Panayiotis (Peter) Nikolaou, Aaron Coffey, Laura L. Walkup, Brogan Gust, **Hayley Newton**, Iga Muradyan, Matthew Rosen, Samuel Patz, Michael J. Barlow, Boyd M. Goodson & Eduard Chekmenev; *"XeUS"; A*

Second-Generation Open Source Clinical-Scale ^{129}Xe Polarizer for Xenon-Induced Polarization; 54th Experimental Nuclear Magnetic Resonance Conference, April 2013, California, USA

3. Kaili Ranta, Laura L. Walkup, Nicholas Whiting, Brogan Gust, **Hayley Newton**, Jason Smith, Michael J. Barlow & Boyd M. Goodson; *SEOP Diagnostics: Exploring Alkali Metal ESR Polarimetry Under Conditions with Poorly Resolved Resonances*; 54th Experimental Nuclear Magnetic Resonance Conference, April 2013, California, USA

4. Panayiotis (Peter) Nikolaou, Aaron Coffey, Laura L. Walkup, Brogan Gust, Nicholas Whiting, **Hayley Newton**, Scott Barcus, Iga Muradyan, Mikayel Dabaghyan, Gregory D. Moroz, Matthew Rosen, Samuel Patz, Michael J. Barlow, Eduard Chekmenev & Boyd M. Goodson; *High (30-90%) ^{129}Xe Hyperpolarization at High Xe Densities Using an Open-Source Polarizer for Clinical and Materials MRS/MRI*; 54th Experimental Nuclear Magnetic Resonance Conference, April 2013, California, USA

2012

5. **Hayley Newton**, Nicholas Whiting, Michael J. Barlow, Peter Morris, Laura Walkup, & Boyd M. Goodson; *In situ Raman spectroscopy to determine N_2 gas temperatures in spin-exchange optical pumping cells for use in hyperpolarised noble gas NMR/MRI*; XeMat 2012 (Xenon in Materials) and Euromar 2012, June/July 2012, Dublin, Ireland

6. Maria Liljeroth, John Owers-Bradley, Robert Walker, **Hayley Newton**, Michael Barlow, Kevin Teh, Ian Hall & Peter Morris; *Hyperpolarized Xenon-129 T_1 Relaxation Rate Dependence on the Partial Pressure of Oxygen, P_{O_2}, in Porcine lungs*; Euromar 2012, July 2012, Dublin, Ireland

7. Panayiotis Nikolaou, Aaron Coffey, Laura Walkup, Brogan Gust, Nicholas Whiting, **Hayley Newton**, Iga Muradyan, Mikayel Dabaghyan, Kaili Ranta, Gregory Moroz, Matthew Rosen, Samuel Patz, Michael J. Barlow, Eduard Chekmenev & Boyd M. Goodson; *"Scaling up" fundamental studies of SEOP at high Xe densities and laser fluxes to create an "open source" Xe polarizer for clinical-scale NMR and MRI*; XeMat 2012 (Xenon in Materials), June 2012, Dublin, Ireland

8. Maria Liljeroth, John Owers-Bradley, Robert Walker, **Hayley Newton**, Michael J. Barlow, Kevin Teh, Ian Hall & Peter Morris; *Hyperpolarized Xenon-129 in the Porcine Lung: A Preclinical Disease Model*; XeMat 2012 (Xenon in Materials), June 2012, Dublin, Ireland

9. Panayiotis Nikolaou, Aaron Coffey, Laura Walkup, Brogan Gust, Nicholas Whiting, **Hayley Newton**, Iga Muradyan, Mikayel Dabaghyan, Kaili

Ranta, Gregory Moroz, Matthew Rosen, Samuel Patz, Michael J. Barlow, Eduard Chekmenev, Shaoyi Xu, Ayse Yilmaz, Ping He, Max Gemeinhardt, Yong Gao & Boyd M. Goodson; *New Developments for Using Hyperpolarized ^{129}Xe and SPIONs as Contrast Agents: 1) "Scaling up" High-[Xe] SEOP for an "open-source" Xe Polarizer; 2) Towards Physiological pH sensing with Dendron Functionalized SPIONs*; Euromar 2012, July 2012, Dublin, Ireland

10. <u>Nicholas Whiting</u>, **Hayley Newton**, Michael J. Barlow, Peter J. Morris & Boyd M. Goodson; *In situ Raman mapping of nitrogen buffer gas rovibrational temperatures in spin-exchange optical pumping cells for use in hyperpolarized noble gas NMR/MRI*; 53rd Experimental Nuclear Magnetic Resonance Conference, April 2012, Miami, USA

11. Panayiotis Nikolaou, Aaron Coffey, <u>Laura Walkup</u>, Brogan Gust, Nicholas Whiting, **Hayley Newton**, Scott Barcus, Iga Muradyan, Gregory D. Moroz, Matthew Rosen, Samuel Patz, Michael J. Barlow, Eduard Chekmenev & Boyd M. Goodson; *An "Open-Source" ^{129}Xe Polarizer for Clinical Imaging, in vivo MRS/MRI, and NMR/MRI of Porous Materials*; 53rd Experimental Nuclear Magnetic Resonance Conference, April 2012, Miami, USA

2011

12. <u>Nicholas Whiting</u>, Michael J. Barlow, **Hayley Newton**, Laura L. Walkup, Panayiotis Nikolaou & Boyd M. Goodson; *Improved Production of Hyperpolarized Xenon using Cesium /Xenon Spin-Exchange Optical Pumping with High-Power, Frequency-Narrowed Laser Diode Arrays and High Xenon Partial Pressures*; Frontiers of Biomedical Science, June 2011, Nashville, USA

13. <u>Nicholas Whiting</u>, Michael J. Barlow, **Hayley Newton**, Laura L. Walkup, Panayiotis Nikolaou & Boyd M. Goodson; *Cesium/Xenon Spin-Exchange Optical Pumping Using High Power, Frequency Narrowed Laser Diode Arrays at High Xenon Densities*; 52nd Experimental Nuclear Magnetic Resonance Conference, April 2011, California, USA

14. <u>Maria Liljeroth</u>, Nicholas Whiting, **Hayley Newton**, Michael J. Barlow, Robert J. Walker, Kevin Teh, Boyd M. Goodson & Peter Morris; *Continuous Flow Rb /^{129}Xe Spin-Exchange Optical Pumping at High Xenon Densities: Preliminary Studies Toward in vivo Lung Imaging*; 52nd Experimental Nuclear Magnetic Resonance Conference, April 2011, California, USA

Note: Presenting author is underlined.

References

[1] National Institute for Health and Clinical Excellence *Chronic obstructive pulmonary disease: Costing report*, NICE clinical guideline 101, February 2011.

[2] National Institute for Health and Clinical Excellence *Lung cancer: Costing report*, NICE clinical guideline 121, April 2011.

[3] National Institute for Health and Clinical Excellence *Idiopathic pulmonary fibrosis: Costing report*, NICE clinical guideline 163, June 2013.

[4] E. J. van Beek and E. A. Hoffman, "Functional imaging: CT and MRI," *Clinics in Chest Medicine*, vol. 29, no. 1, pp. 195 – 216, 2008.

[5] W. Happer, "Optical pumping," *Reviews of Modern Physics*, vol. 44, no. 2, pp. 435–470, 1972.

[6] T. Walker and W. Happer, "Spin-exchange optical pumping of noble-gas nuclei," *Reviews of Modern Physics*, vol. 69, no. 2, pp. 629–642, 1997.

[7] M. Albert, G. Cates, B. Driehuys, W. Happer, B. Saam, C.S. Springer Jr, and A. Wishnia, "Biological magnetic resonance using laser-polarized ^{129}Xe," *Nature*, vol. 370, p. 199, 1994.

[8] P. Nikolaou, A. M. Coffey, L. L. Walkup, B. M. Gust, N. Whiting, H. Newton, S. Barcus, I. Muradyan, M. Dabaghyan, G. D. Moroz, M. S. Rosen, S. Patz, M. J. Barlow, E. Y. Chekmenev, and B. M. Goodson, "Near-unity nuclear polarization with an open-source 129Xe hyperpolarizer for NMR and MRI," *Proceedings of the National Academy of Sciences*, vol. 110, no. 35, pp. 14150 – 14155, 2013.

[9] P. Nikolaou, A. M. Coffey, L. L. Walkup, B. M. Gust, N. Whiting, H. Newton, I. Muradyan, M. Dabaghyan, K. Ranta, G. D. Moroz, M. S. Rosen, S. Patz, M. J. Barlow, E. Y. Chekmenev, and B. M. Goodson, "XeNA: An automated open-source ^{129}xe hyperpolarizer for clinical use," *Magnetic Resonance Imaging*, vol. 32, no. 5, pp. 541 – 550, 2014.

[10] N. Whiting, H. Newton, P. Morris, M. J. Barlow, and B. M. Goodson, "Observation of energy thermalization and ~ 1000 K gas temperatures during spin-exchange optical pumping at high xenon densities," *manuscript in preparation*, 2014.

[11] H. Newton, L. L. Walkup, N. Whiting, L. West, J. Carriere, F. Havermeyer, L. Ho, P. Morris, B. M. Goodson, and M. J. Barlow, "Comparative study of in situ N_2 rotational Raman spectroscopy methods for probing energy thermalisation processes during spin-exchange optical pumping," *Applied Physics B: Lasers and Optics*, vol. 115, no. 2, pp. 167 – 172, 2014.

[12] H. Newton, N. Whiting, M. J. Barlow, P. Morris, L. Walkup, and B. M. Goodson, "Effects of various spin-exchange optical pumping conditions on gas temperatures measured by Raman spectroscopy during production of hyperpolarised ^{129}Xe," in *XeMat 2012 (Xenon in Materials), Dublin, Ireland*, 29 June 2012.

[13] N. Whiting, M. J. Barlow, H. Newton, L. L. Walkup, P. Nikolaou, and B. M. Goodson, "Cesium/xenon spin-exchange optical pumping using high-power, frequency-narrowed laser diode arrays at high xenon densities," in *52nd Experimental Nuclear Magnetic Resonance Conference 2011, California, USA*.

[14] H. Newton, J. Skinner, J. Birchall, N. Whiting, B. M. Gust, K. Ranta, M. J. Barlow, and B. M. Goodson, "Can we utilise Rb/Cs hybrid optical pumping to hyperpolarise noble gases?," in *55th Experimental Nuclear Magnetic Resonance Conference 2014, Boston, USA*, 24 March 2014.

[15] B. M. Goodson, "Nuclear magnetic resonance of laser-polarized noble gases in molecules, materials, and organisms," *Journal of Magnetic Resonance*, vol. 155, p. 157, 2002.

[16] J. D. O'Neill, *Brute Force Polarisation of Xenon-129*. PhD thesis, University of Nottingham, 2008.

[17] A. Honig, X. Wei, A. Lewis, E. ter Haar, and K. Seraji-Bozorgzad, "High equilibrium spin polarizations in solid ^{129}Xe," *Physica B: Condensed Matter*, vol. 284-288, pp. 2049–2050, 2000.

[18] E. V. Krjukov, J. D. ONeill, and J. R. Owers-Bradley, "Brute force polarization of ^{129}Xe," *Journal of Low Temperature Physics*, vol. 140, no. 516, pp. 397 – 408, 2005.

[19] "The NIST Reference on Constants, Units, and Uncertainty, http://physics.nist.gov/cgi-bin/cuu/Value?gammae," February 2014.

[20] *Tables of Physical & Chemical Constants.* 3.8.1 Nuclear moments and magnetic resonance: Kaye & Laby Online. Version 1.0 (2005) www.kayelaby.npl.co.uk, 16th ed., 1995.

[21] R. Hurd, Y. Yen, and A. C. J. Ardenkjaer-Larsen, "Hyperpolarized 13C metabolic imaging using dissolution dynamic nuclear polarization," *Journal of Magnetic Resonance Imaging*, vol. 36, no. 6, pp. 1314–1328, 2012.

[22] S. Duckett and R. Mewis, "Application of parahydrogen induced polarization techniques in NMR spectroscopy and imaging," *Accounts of Chemical Research*, vol. 45, no. 8, pp. 1247–1257, 2012.

[23] S. Duckett and N. Wood, "Parahydrogen-based NMR methods as a mechanistic probe in inorganic chemistry," *Coordination Chemistry Reviews*, vol. 252, pp. 2278–2291, 2008.

[24] M. Batz, P.-J. Nacher, and G. Tastevin, "Fundamentals of metastability exchange optical pumping in helium," *Journal of Physics: Conference Series*, vol. 294, p. 012002, 2011.

[25] A. Kastler, "Optical methods of atomic orientation and of magnetic resonance," *Journal of the Optical Society of America*, vol. 47, no. 6, pp. 460–465, 1957.

[26] A. B. Baranga, S. Appelt, M. V. Romalis, C. J. Erickson, A. R. Young, G. D. Cates, and W. Happer, "Polarization of ^{3}He by spin exchange with optically pumped Rb and K vapors," *Physical Review Letters*, vol. 80, no. 13, pp. 2801–2804, 1998.

[27] Z. I. Cleveland, G. E. Pavlovskaya, N. D. Elkins, K. F. Stupic, J. E. Repine, and T. Meersmann, "Hyperpolarized 83Kr MRI of lungs," *Journal of Magnetic Resonance*, vol. 195, no. 2, pp. 232 –237, 2008.

[28] N. Whiting, N. A. Eschmann, B. M. Goodson, and M. J. Barlow, "^{129}Xe-Cs (D$_1$,D$_2$) versus ^{129}Xe-Rb (D$_1$) spin-exchange optical pumping at high xenon densities using high-power laser diode arrays," *Physical Review A*, vol. 83, p. 053428, 2011.

[29] K. F. Stupic, Z. I. Cleveland, G. E. Pavlovskaya, and T. Meersmann, "Hyperpolarized 131Xe NMR spectroscopy," *Journal of Magnetic Resonance*, vol. 208, pp. 58 – 69, 2011.

[30] D. A. Steck, "Rubidium 85 D line data," available online at http://steck.us/alkalidata (revision 0.1.1, 2 May 2008).

[31] D. A. Steck, "Cesium D line data," available online at http://steck.us/alkalidata (revision 2.0.1, 2 May 2008).

[32] B. Driehuys, G. D. Cates, E. Miron, K. Sauer, D. K. Walter, and W. Happer, "High-volume production of laser-polarized 129Xe," *Applied Physics Letters*, vol. 96, no. 12, pp. 1668 –1670, 1996.

[33] N. Whiting, P. Nikolaou, N. A. Eschmann, B. M. Goodson, and M. J. Barlow, "Interdependence of in-cell xenon density and temperature during Rb/Xe-129 spin-exchange optical pumping using VHG-narrowed laser diode arrays," *Journal of Magnetic Resonance*, vol. 208, no. 2, pp. 298–304, 2011.

[34] E. Brunner, "Enhancement of surface and biological magnetic resonance using laser-polarized noble gases," *Concepts in Magnetic Resonance*, vol. 11, no. 5, pp. 313 – 335, 1999.

[35] G. D. Cates, R. J. Fitzgerald, A. S. Barton, P. Bogorad, M. Gatzke, N. R. Newbury, and B. Saam, "Rb-129Xe spin-exchange rates due to binary and three-body collisions at high Xe pressures," *Physical Review A*, vol. 45, no. 7, pp. 4631 – 4639, 1992.

[36] T. Tiecke, "Properties of potassium," available online at http://staff.science.uva.nl/∼walraven/walraven/Publications_files/ PotassiumProperties.pdf, version 1.0, 2010.

[37] C. W. Bale and A. D. Pelton, "The Cs-Rb (cesium -rubidium) system," *Bulletin of Alloy Phase Diagrams*, vol. 4, no. 4, pp. 382 – 384, 1983.

[38] *Tables of Physical & Chemical Constants.* 3.7.5 Atomic radii: Kaye & Laby Online. Version 1.0 (2005) www.kayelaby.npl.co.uk, 16th ed., 1995.

[39] W. Shao, G. Wang, and E. Hughes, "Measurement of spin-exchange rate constants between Xe-129 and alkali metals," *Physical Review A*, vol. 72, no. 2, p. 022713, 2005.

[40] *Tables of Physical & Chemical Constants.* 3.1.2 Properties of the elements: Kaye & Laby Online. Version 1.0 (2005) www.kayelaby.npl.co.u, 16th ed., 1995.

[41] W. Happer, G. D. Cates, M. V. Romalis, and C. J. Erickson, "Alkali metal hybrid spin-exchange optical pumping," United States Patent, US 6318092 B1, 2001.

[42] E. Babcock, I. Nelson, S. Kadlecek, B. Driehuys, L. Anderson, F. Hersman, and T. G.Walker, "Hybrid spin-exchange optical pumping of ^{3}He," *Physical Review Letters*, vol. 91, no. 12, p. 123003, 2003.

[43] W. C. Chen, T. R. Gentile, T. G. Walker, and E. Babcock, "Spin-exchange optical pumping of ^{3}He with Rb-K mixtures and pure K," *Physical Review A*, vol. 75, p. 013416, 2007.

[44] Y.-Y. Jau, N. N. Kuzma, and W. Happer, "Measurement of ^{129}Xe-Cs binary spin-exchange rate coefficient," *Physical Review A*, vol. 69, p. 061401(R), 2004.

[45] Y.-Y. Jau, N. N. Kuzma, and W. Happer, "High-field measurement of the ^{129}Xe-Rb spin-exchange rate due to binary collisions," *Physical Review A*, vol. 66, p. 052710, 2002.

[46] H. M. Gibbs and R. J. Hull, "Spin-exchange cross sections for Rb^{87}-Rb^{87} and Rb^{87}-Cs^{133} collisions," *Physical Review*, vol. 153, no. 1, pp. 132 – 151, 1967.

[47] R. T. Kouzes, "The ^{3}He supply problem," *U.S. Department of Energy, PNNL-18388*, 2009.

[48] J. Woods, "Congressional hearing: caught by surprise: causes and consequences of the helium-3 supply crisis," *Testimony before the House Committee on Science and Technology, Subcommittee on Investigations and Oversight*, 2010.

[49] General Electric, 2500 Meridian Parkway, Suite 110, Durham, NC 27713, USA, *Xenon Polarizer Service Manual*, 2.0 ed., 2004. Part no. 02828.

[50] I. Saha, P. Nikolaou, N. Whiting, and G. B.M, "Characterization of violet emission from Rb optical pumping cells used in laser-polarized xenon NMR experiments," *Chemical Physics Letters*, vol. 428, pp. 268 – 276, 2006.

[51] D. K. Walter, W. Griffith, and W. Happer, "Energy transport in high-density spin-exchange optical pumping cells," *Physical Review Letters*, vol. 86 (15), pp. 3264 – 3267, 2001.

[52] S. Patz, F. W. Hersman, I. Muradian, M. I. Hrovat, I. C. Ruset, S. Ketel, F. Jacobson, G. P. Topulos, H. Hatabu, and J. P. Butler, "Hyperpolarized ^{129}Xe MRI: A viable functional lung imaging modality?," *European Journal of Radiology*, vol. 64, no. 3, pp. 335 – 344, 2008.

[53] Polarean, Durham, NC, USA, www.polarean.com, "Hyperpolarization system datasheet."

[54] G. Norquay, S. R. Parnell, X. Xu, J. Parra-Robles, and J. M. Wild, "Optimized production of hyperpolarized Xe-129 at 2 bars for in vivo lung magnetic resonance imaging," *Journal of Applied Physics*, vol. 113, no. 4, p. 044908, 2013.

[55] I. C. Ruset, S. Ketel, and F. Hersman, "Optical pumping system design for large production of hyperpolarized ^{129}Xe," *Physical Review Letters*, vol. 96, p. 053002, 2006.

[56] G. Schrank, Z. Ma, A. Schoeck, and B. Saam, "Characterization of a low-pressure high-capacity Xe-129 flow-through polarizer," *Physical Review A*, vol. 80, no. 6, p. 063424, 2009.

[57] N. N. Kuzma, B. Patton, K. Raman, and W. Happer, "Fast nuclear spin relaxation in hyperpolarized solid ^{129}Xe," *Physical Review Letters*, vol. 88, no. 14, p. 147602, 2002.

[58] P. Nikolaou, A. Coffey, L. Walkup, B. Gust, C. LaPierre, E. Koehnemann, M. Barlow, M. Rosen, B. Goodson, and E. Chekmenev, "A 3D-printed high power nuclear spin polarizer," *Journal of American Chemical Society*, vol. 136, no. 4, pp. 1636 – 1642, 2014.

[59] P. Nikolaou, A. M. Coffey, K. Ranta, L. L. Walkup, B. M. Gust, M. J. Barlow, M. S. Rosen, B. M. Goodson, and E. Y. Chekmenev, "Multidimensional mapping of spin-exchange optical pumping in clinical-scale batch-mode ^{129}Xe hyperpolarizers," *The Journal of Physical Chemistry*, DOI:10.1021/jp501493k, 2014.

[60] J. M. Wild, H. Marshall, X. Xu, G. Norquay, S. R. Parnell, M. Clemence, P. D. Griffiths, and J. Parra-Robles, "Simultaneous Imaging of Lung Structure and Function with Triple-Nuclear Hybrid MR Imaging," *Radiology*, vol. 267, no. 1, pp. 251–255, 2013.

[61] B. Driehuys, S. Martinez-Jimenez, Z. I. Cleveland, G. M. Metz, D. M. Beaver, J. C. Nouls, S. S. Kaushik, R. Firszt, C. Willis, K. T. Kelly, J. Wolber, M. Kraft, and H. P. McAdams, "Chronic obstructive pulmonary disease: Safety and tolerability of hyperpolarized 129 Xe MR imaging in healthy volunteers and patients," *Radiology*, vol. 262, no. 1, pp. 279 – 289, 2012.

[62] S. Klippel, J. Dopfert, J. Jayapaul, M. Kunth, F. Rossella, M. Schnurr, C. Witte, C. Freund, and L. Schroder, "Cell tracking with caged xenon: Using cryptophanes as MRI reporters upon cellular internalization," *Angewandte Chemie, International Edition*, vol. 53, pp. 493 – 496, 2014.

[63] M. S. Rosen, T. E. Chupp, K. P. Coulter, R. C. Welsh, and S. D. Swanson, "Polarized 129Xe optical pumping/spin exchange and delivery system for magnetic resonance spectroscopy and imaging studies," *Review of Scientific Instruments*, vol. 70, no. 2, pp. 1546 – 1552, 1999.

[64] X. Zeng, E. Miron, W. V. Wijngaarden, D. Schreiber, and W. Happer, "Wall relaxation of spin polarized ^{129}Xe nuclei," *Physics Letters A*, vol. 96, no. 4, pp. 191 –194, 1983.

[65] B. Driehuys, G. D. Cates, and W. Happer, "Surface relaxation mechanisms of laser-polarized ^{129}Xe," *Physical Review Letters*, vol. 74, pp. 4943–4946, 1995.

[66] P. Atkins and J. De Paula, *Atkins' Physical Chemistry*. Oxford: Oxford University Press, 7th ed., 2002.

[67] N. Whiting, *Using high-powered, frequency-narrowed lasers for Rb/129Xe and Cs/129Xe spin-exchange optical pumping to achieve improved production of highly spin-polarized xenon for use in magnetic resonance applications*. PhD thesis, Southern Illinois University, 2010.

[68] *Terranova Student Handbook*. Magritek, New Zealand.

[69] I. C. Ruset, *Hyperpolarized ^{129}Xe Production and Applications*. PhD thesis, University of New Hampshire, 1999.

[70] P. Nikolaou, N. Whiting, N. A. Eschmann, K. E. Chaffee, B. M. Goodson, and M. J. Barlow, "Generation of laser-polarized xenon using fiber-coupled laser-diode arrays narrowed with integrated volume holographic gratings," *Journal of Magnetic Resonance*, vol. 197, no. 2, pp. 249–254, 2009.

[71] N. Whiting, P. Nikolaou, N. A. Eschmann, M. J. Barlow, R. Lammert, J. Ungar, W. Hu, L. Vaissie, and B. M. Goodson, "Using frequency-narrowed, tunable laser diode arrays with integrated volume holographic gratings for spin-exchange optical pumping at high resonant fluxes and xenon densities," *Applied Physics B: Lasers and Optics*, vol. 106, pp. 775–788, 2012.

[72] E. Smith, *Modern Raman Spectscopy: A Practical Approach*. John Wiley & Sons, Inc, 2005.

[73] R. S. Hickman and L. H. Liang, "Rotational temperature measurement in nitrogen using Raman spectroscopy," *Review of Scientific Instruments*, vol. 43, pp. 796 – 799, 1972.

[74] A. Compaan, A. Wagoner, and A. Aydinli, "Rotational Raman scattering in the instructional laboratory," *American Journal of Physics*, vol. 62 (7), pp. 639 – 645, 1994.

[75] D. N. 000-10000-010-02-1209, *Ocean Optics Calibration Light Source CAL-2000 Installation and Operation Manual*, 2009, Dunedin, FL, USA.

[76] R. S. Mulliken, "Intensities of electronic transitions in molecular spectra I. introduction," *Journal of Chemical Physics*, vol. 7, pp. 14 – 20, 1939.

[77] G. Herzberg, *Molecular Spectra and Molecular Structure Vol II, Infrared and Raman Spectra of Polyatomic Molecules*. D. Van Nostrand Company, Inc, 13th ed., 1968.

[78] J. M. Hollas, *Modern Spectroscopy*. John Wiley, 3rd ed., 1998.

[79] D. Simonelli and M. J. Shultz, "Temperature dependence for the relative Raman cross section of the ammonia/water complex," *Journal of Molecular Spectroscopy*, vol. 205, pp. 221 – 226, 2001.

[80] M. V. Romalis, E. Miron, and G. D. Cates, "Pressure broadening of Rb D_1 and D_2 lines by ^{3}He, ^{4}He, N_2, and Xe. Line cores and near wings," *Physical Review A*, vol. 56, pp. 4569–4578, 1997.

[81] A. Fink, D. Baumer, and E. Brunner, "Production of hyperpolarized xenon in a static pump cell: Numerical simulations and experiments," *Physical Review A*, vol. 72, p. 053411, 2005.

[82] J. S. Six, T. Hughes-Riley, K. F. Stupic, G. E. Pavlovskaya, and T. Meersmann, "Pathway to cryogen free production of hyperpolarized krypton-83 and xenon-129," *PLoS ONE*, vol. 7, no. 11, p. e49927, 2012.

[83] C. Alcock, V. Itkin, and M. Horrigan, "Vapor pressure of the metal elements," *Canadian Metallurgical Quarterly*, vol. 23, p. 309, 1984.

[84] M. Wagshul and T. Chupp, "Laser optical pumping of high-density Rb in polarized ^{3}He targets," *Physical Review A*, vol. 49, no. 5, pp. 3854 – 3869, 1994.

[85] A. Fink and E. Brunner, "Optimization of continuous flow pump cells used for the production of hyperpolarized ^{129}Xe: A theoretical study," *Applied Physics B*, vol. 89, pp. 65 – 71, 2007.

[86] S. R. Parnell, M. H. Deppe, S. Ajraoui, J. Parra-Robles, S. Boag, and J. M. Wild, "Measurement of laser heating in spin exchange optical pumping by NMR diffusion sensitization gradients," *Journal of Applied Physics*, vol. 107, p. 094904, 2010.

[87] "T64000 and U1000 Horiba-Yvon Raman division brochure, accessed from http://www.instrument.com.cn/show/literature/c13445.pdf," Horiba Jobin Yvon, France.

[88] C. Witte, M. Kunth, F. Rossella, and L. Schröder, "Observing and preventing rubidium runaway in a direct-infusion xenon-spin hyperpolarizer optimized for high-resolution hyper-CEST (chemical exchange saturation transfer using hyperpolarized nuclei) NMR," *The Journal of Chemical Physics*, vol. 140, p. 084203, 2014.

[89] S. Appelt, T. Ünlü, K. Zilles, N. J. Shah, S. Baer-Lang, and H. Halling, "Experimental studies of rubidium absolute polarization at high temperatures," *Applied Physics Letters*, vol. 75, no. 3, pp. 427 – 429, 1999.

[90] A. L. Zook, B. B. Adhyaru, and C. R. Bowers, "High capacity production of >65% spin polarized xenon-129 for NMR spectroscopy and imaging," *Journal of Magnetic Resonance*, vol. 159, pp. 175 – 182, 2002.

[91] C. Moser and F. Havermeyer, "Ultra-narrow-band tunable laserline notch filter," *Applied Physics B*, vol. 95, pp. 597 – 601, 2009.

[92] G. W. Faris and R. A. Copeland, "Ratio of oxygen and nitrogen Raman cross sections in the ultraviolet," *Applied Optics*, vol. 36, no. 12, pp. 2684 – 2685, 1997.

[93] P. Nikolaou, A. M. Coffey, M. J. Barlow, M. S. Rosen, B. M. Goodson, and E. Y. Chekmenev, "Temperature-ramped ^{129}Xe spin exchange optical pumping," *manuscript in preparation*, 2014.

[94] N. Ressler, R. Sands, and T. Stark, "Measurement of spin-exchange cross section for ^{133}Cs, ^{87}Rb, ^{85}Rb, ^{39}K, and ^{23}Na," *Physical Review*, vol. 184, no. 1, pp. 102 – 118, 1969.

[95] E. Babcock, *Spin-Exchange Optical Pumping with Alkali-Metal Vapors*. PhD thesis, University of Wisconsin-Madison, 2005.

[96] B. Chann, E. Babcock, L. Anderson, and T. Walker, "Measurements of He-3 spin-exchange rates," *Physical Review A*, vol. 66, SEP 2002.

[97] A. R. Young, S. Appelt, A. B. Baranga, C. Erickson, and W. Happer, "Three-dimensional imaging of spin polarization of alkali-metal vapor in optical pumping cells," *Applied Physics Letters*, vol. 70, no. 23, pp. 3081–3083, 1997.

[98] N. Shah, T. Unlu, H. Wegener, H. Halling, K. Zilles, and S. Appelt, "Measurement of rubidium and xenon absolute polarization at high temperatures as a means of improved production of hyperpolarized Xe-129," *NMR in Biomedicine*, vol. 13, no. 4, pp. 214–219, 2000.

[99] E. van Beek, A. Dahmen, T. Stavngaard, K. Gast, C. Heussel, F. Krummenauere, J. Schmiedeskamp, J. Wild, L. Sgaard, A. Morbach, L. Schreiber, and H.-U. Kauczor, "Hyperpolarised ^{3}He MRI versus HRCT in COPD and normal volunteers: PHIL trial," *European Respiratory Journal*, vol. 34, pp. 1311 – 1321, 2009.

[100] Y. Ohno, H. Koyama, T. Yoshikawa, K. Matsumoto, M. Takahashi, M. V. Cauteren, and K. Sugimura, "T2* measurements of 3-T MRI with ultrashort TEs: Capabilities of pulmonary function assessment and clinical stage classification in smokers," *Cardiopulmonary Imaging*, vol. 197, p. W279, 2011.

[101] O. Togao, R. Tsuji, Y. Ohno, I. Dimitrov, and M. Takahashi, "Ultra-short echo time (UTE) MRI of the lung: Assessment of tissue density in the lung parenchyma," *Magnetic Resonance in Medicine*, vol. 64, no. 5, pp. 1491–1498, 2010.

[102] G. D. Cates, D. R. Benton, M. Gatzke, W. Happer, K. C. Hasson, and N. R. Newbury, "Laser production of large nuclear-spin polarization in frozen xenon," *Physical Review Letters*, vol. 65, no. 20, pp. 2591 – 2594, 1990.

[103] M. Gatzke, G. D. Cates, B. Driehuys, D. Fox, W. Happer, and B. Saam, "Extraordinarily slow nuclear spin relaxation in frozen laser-polarized ^{129}Xe," *Physical Review Letters*, vol. 70, p. 690, 1993.

[104] S. W. Morgan, *Relaxation of Solid Hyperpolarized ^{129}Xe*. PhD thesis, University of Utah, 2007.

[105] S. Appelt, F. Hasing, H. Kuhn, J. Perlo, and B. Blumich, "Mobile high resolution xenon nuclear magnetic resonance spectroscopy in the earth's magnetic field," *Physical Review Letters*, vol. 94, no. 19, 2005.

[106] B. Anger, *Polarization and relaxation in hyperpolarized ^{3}He and ^{129}Xe*. PhD thesis, University of Utah, 2008.

[107] C. Jameson, A. Jameson, and J. Hwang, "Nuclear spin relaxation by intermolecular magnetic dipole coupling in the gas phase. ^{129}Xe in oxygen," *Journal of Chemical Physics*, vol. 89, no. 7, pp. 4074 – 4081, 1988.

[108] L. D. Schearer and G. K. Walters, "Nuclear spin-lattice relaxation in the presence of magnetic-field gradients," *Physical Review*, vol. 139, pp. A1398 – A1402, 1965.

[109] D. Weishaupt, V. D. Köchli, and B. Marincek, *How does MRI work?* Springer, 2nd ed., 2006.